Università degli studi di Trieste

Extending approximate methods to generate simulated halo catalogs with modified gravity

Settore scientifico-disciplinare:
Astronomia e Astrofisica

Coordinatore:
Prof. Francesco Longo
Francesco Longo

Dottoranda:
Chiara Moretti

Supervisor:
Prof. Pierluigi Monaco
Pierluigi Monaco

Anno Accademico 2018/2019

Abstract

The current standard model of cosmology, the ΛCDM model, has proven to be extremely successful at fitting most cosmological observations on large scales, such as the cosmic microwave background and the large scale structure of the Universe. Nonetheless, to be consistent, it requires the introduction of exotic components: cold dark matter, which drives the gravitational evolution, and dark energy, responsible for the observed accelerated expansion of the Universe. Unveiling the nature of dark energy and dark matter is one of the most challenging and elusive open questions in cosmology and fundamental physics. The ΛCDM model relies on the assumption that the growth of structures in the Universe is driven by gravitational instability, described by Einstein's General Relativity (GR). Under this hypothesis, the simplest explanation for the observed accelerated expansion, and the only one that does not add new degrees of freedom, is that of a cosmological constant Λ. Its natural interpretation as the effect of vacuum energy poses however strong theoretical problems, such as fine tuning: the value of Λ needed to explain the recent accelerated expansion phase must be $\sim$120 orders of magnitude smaller than the value predicted by quantum field theory.

An alternative to the introduction of a cosmological constant is that GR is not the correct theory for gravity on cosmological scales. This possibility has prompted the development of a large number of Modified Gravity (MG) models. Such theories foresee specific signatures on cosmological observables, that are however not detected in currently available data. Admittedly, General Relativity has successfully passed all tests up to now, from laboratory, to Solar System, to the recent breakthroughs provided by the observation of gravitational waves and the imaging of the black hole in M87. As a consequence, any alternative theory, in order to be viable, must satisfy very tight constraints. One of the key targets of future generations of large scale struc-

ture surveys, such as Euclid, DESI, LSST or WFIRST, is indeed to investigate the nature of dark energy, and possibly disentangle between different gravity models. In general, MG models involve the introduction of an additional fifth force, whose behavior can be subdivided in three different regimes: on the largest scales the background evolution must mimic ΛCDM, but with a large deviation from GR, in order to explain the accelerated expansion without the need of a cosmological constant. On the smallest scales, the theory must reduce to GR: to achieve this, a screening mechanism must be introduced. Finally, there could still be deviations from GR on intermediate scales, making the mildly non-linear (NL) regime of structure formation particularly suitable to test MG models.

It is therefore of crucial importance that accurate theoretical predictions for different cosmological observables are available, and that such predictions are pushed to NL scales, in order to better exploit the data coming from future surveys. The standard, and most reliable tools employed to describe NL scales are N-body simulations. However, full N-body simulations are computationally expensive, and even more so if they are run with modified gravity. Their use becomes impractical, even in the standard GR case, when addressing the computation of covariance matrices of observables like the galaxy power spectrum or two-point correlation function; in this case thousands of realizations are required to properly populate the matrices and suppress sampling noise. A complementary approach is provided by the so-called approximate methods, able to quickly generate dark matter distributions and to describe the mildly-NL scales with minor compromises in accuracy.

One such method is implemented in the PINOCCHIO software, developed at INAF-Osservatorio Astronomico di Trieste (Monaco et al., 2002a,b, 2013), which performs simulations in the context of the ΛCDM model. Its algorithm is based on Lagrangian perturbation theory (LPT) and ellipsoidal collapse (EC). The main goal of this PhD work is to extend PINOCCHIO to make it capable of producing matter distributions in the context of beyond-ΛCDM models, with a particular focus on $f(R)$ models. Such extension requires a proper formulation of both LPT and EC in modified gravity, as well as an efficient numerical implementation of the two.

Together with MG models, the broad class of beyond-ΛCDM cosmologies includes also Warm Dark Matter (WDM) models, as a possible alternative to cold dark matter. Such theories take into account the possibility that dark matter particles retain relatively high velocities, which allow them to travel beyond some free-streaming scale, resulting in a suppression of small-scale fluctuations. As a first project of my PhD I considered the possibility of extending PINOCCHIO to WDM cosmologies following the technique of Bode et al. (2001), that mimics the small-scale suppression of power due to WDM free streaming by adopting a truncated power spectrum. Such approach showed a discrepancy between the halo mass function computed from PINOCCHIO and the one measured from WDM simulations, with a significant suppression on the high-mass end of the spectrum. I performed thorough tests by changing the smoothing scheme adopted by the code, which is equivalent to feeding the code a truncated power spectrum. Moreover, I performed an object-by-object analysis on halo catalogs produced with different minimum smoothing radii. Such analysis revealed an issue in the grouping part of the algorithm, and highlighted the need of a re-calibration. Since the calibration process is a rather lengthy one, and the code is currently undergoing major development, we leave this for a future work.

Afterwards I focused on extending PINOCCHIO to MG models, which required a proper reformulation of LPT. The latter is adopted in several fast, approximate codes that generate halo catalogs, since it allows to factorize the evolution of the displacement field in terms of a spatial part, and time-dependent growth functions for the different perturbative orders. It is therefore possible, starting from an initial displacement field, to readily compute particle displacements for any given redshift. In several MG models however the growth functions become scale dependent, making the separation not feasible. Moreover, the second order growth rate D_2 depends on three wavenumbers, that are constrained to form a triangle in Fourier space. Solving the full equation for second-order displacements would be too demanding in terms of computational time. One possibility is therefore to consider approximations for D_2 that only depend on k, as proposed in Winther et al. (2017). To find the proper approximation for D_2 I developed a new numerical method based on FFTs, consisting in computing the full source term of the second-order displacement differential equation, and comparing to several triangle configurations to choose the one that best matches the full source term. The resulting approximated D_2 is then used in a code to compute Lagrangian displacements, and tested against N-body simulations run with Hu-Sawicki $f(R)$ (Giocoli et al., 2018). Starting from 2LPT displacements, the halo catalog is constructed by matching the particle membership to the simulation catalog. From the reconstructed catalog I compute the halo power spectrum and compare to N-body simulations, showing that our approximation allows to recover the halo power spectrum of the simulations within 10% accuracy up to mildly NL scales ($\sim$0.2 h Mpc^{-1}), with the same performance as in the ΛCDM case. These results are summarized in a paper, accepted for publication on MNRAS (Moretti et al., 2019).

In order to construct halo catalogs, PINOCCHIO relies on the computation of collapse times, obtained by treating overdensities as homogeneous ellipsoids. Along with the introduction of scale-dependent growth to compute displacements, a proper reformulation of EC is therefore required. In its standard version, PINOCCHIO computes collapse times by taking advantage of the Lagrangian formulation of EC (Monaco, 1997a). Within this framework, the moment of collapse is defined as the moment of orbit crossing, and the linear growth rate is adopted as a time variable. However, in the context of MG models such approach is not suitable, since the growth rate is scale-dependent. An appropriate alternative is the description of the evolution of ellipsoidal overdensities provided by Bond & Myers (1996) (BM). Such approach involves the solution of integro-differential equations, and was later reformulated in Nadkarni-Ghosh & Singhal (2016) (NGS) to avoid integrals. The NGS formulation allows for a faster numerical solution with respect to BM, making it suitable to implement in PINOCCHIO. Starting from the results of Ruan et al. (2020), where the Authors present an extension of the BM approach to MG, I extend the NGS description to include both the gravity enhancement and the screening mechanism due to MG. With this formulation of EC the code will be able to generate the large sets of realizations needed to properly compute covariance matrices for cosmological observables in the MG framework. These results will appear in a forthcoming paper (Moretti 2020, in preparation).

This thesis is structured as follows:

- Chapter 1 provides a general introduction of cosmology and describes the standard ΛCDM model, together with current observational constraints on the cosmological parameters;

- Chapter 2 describes the growth of cosmic structures and the numerical tools employed to predict their evolution (such as Eulerian and Lagrangian perturbation theories, N-body simulations, approximate methods and ellipsoidal collapse);

- Chapter 3 provides an overview of MG models, with particular focus on the $f(R)$ family of models that are considered in this work;
- Chapter 4 provides a detailed description of the PINOCCHIO software, and an analysis on the extension of the code to WDM cosmologies;
- Chapter 5 provides a description of the new numerical method developed to compute second-order Lagrangian displacements with MG. I show how the method can be employed to find approximations for the second-order scale-dependent growth rate, and illustrate the comparison between my results and the outputs of a suite of N-body simulations;
- Chapter 6 presents a comparison between different descriptions of ellipsoidal collapse, and their extension to compute collapse times with modified gravity;
- In the final chapter (7) I discuss the results obtained, present a summary of the work undertaken during my PhD, and present future prospects.

Contents

Chapter 1

Introduction

> *Cosmology is peculiar among the sciences for it is both the oldest and the youngest. From the dawn of civilization man has speculated about the nature of the starry heavens and the origin of the world, but only in the present century has physical cosmology split away from general philosophy, to become an independent discipline.*
>
> G. J. Withrow

Cosmology is the study of the Universe as a whole, of its origin and history, its energy content and structure. While men always wondered *where does the universe come from?*, it is only in the last century, with the birth of modern cosmology, that the latter transitioned from being mostly related to philosophy, to being fully considered a branch of physics. This shift was made possible by theoretical developments paired with an increasing amount of data, owed to astounding technological advancements over the last century.

The beginning of cosmology as a science is usually identified with the advent of Einstein's theory for gravity, General Relativity (GR), in 1915. This theory, together with the *cosmological principle*, namely the assumption that the Universe is homogeneous and isotropic on large scales, build up the theoretical foundations for our understanding of the Universe. In subsequent years, several observations allowed to consolidate a shared cosmological picture:

- The realization that our Universe is expanding (Lemaître, 1927; Hubble, 1929), and that the expansion is currently proceeding at an accelerated rate (Perlmutter et al., 1999; Riess et al., 1998);

- Observations on the abundances of light elements, explained as result of a Hot Big Bang followed by a primordial nucleosynthesis phase (Gamow, 1946). Such theory is supported by the discovery of the the Cosmic Microwave Background radiation (CMB, Penzias & Wilson 1965; Peebles 1968);

- Investigations of the Large Scale Structure (LSS) of the Universe via galaxy redshift surveys showed that the distribution of matter in the Universe is clumpy and forms the so-called *cosmic web*. Redshift surveys started in the 1970s (CfA Redshift Survey with $\sim$ 2000 galaxies, Davis & Peebles 1983; Geller & Huchra 1989), and have evolved to vast and modern ones (Sloan Digital Sky Survey [1], millions of galaxies).

Starting from the pioneering work by Edwin Hubble, we know that our Universe is expanding. In his seminal paper (Hubble, 1926), Hubble confirmed that spiral nebulæ were extragalactic objects. Further investigations showed that such objects are moving away from us (Hubble, 1929), with a recession velocity that is proportional to their distance from the observer. This result was obtained by combining data from Cepheid variable stars, that can be used as standard candles, with redshift data. Hubble discovered a rough proportionality between redshift and distance, the well-known Hubble law:

$$v = H_0 r \;, \tag{1.1}$$

where H_0 is the Hubble constant. His results are shown in Fig. 1.1. The value of H_0 determined by Hubble himself was: $H_0 \sim 500$ km s^{-1} Mpc^{-1}, with a large error associated to it, as can be understood from the scatter of data points in Fig. 1.1. Even though eq. 1.1 holds only at small redshifts ($z \ll 1$), this result is considered to be the first observational evidence for the cosmic expansion.

The fact that the Universe is expanding and cooling led to think that it must have been denser and hotter in the past. This idea brought Robert Gamow to suggest, in the late 1940s, that the chemical elements might have

---

[1] `https://www.sdss.org/`

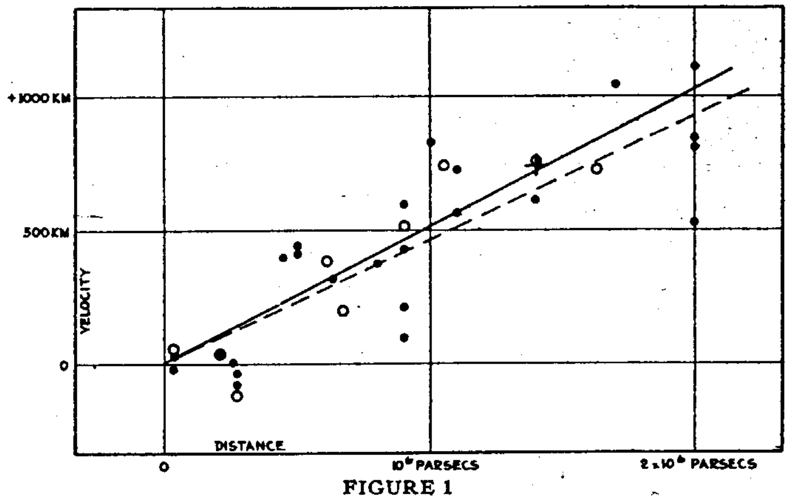

Fig. 1.1: Velocity vs. distance, Hubble's original data from his 1929 paper

been created in the early Universe in a *primordial nucleosynthesis* phase (Gamow, 1946). Moreover, Gamow realized that residual light should still be visible today as a background thermal radiation, with a temperature of a few degrees Kelvin (i.e. peaking at microwave wavelengths). That was the first prediction of the Cosmic Microwave Background Radiation (CMB), later discovered by Arno Penzias and Robert Wilson (Penzias & Wilson, 1965). According to the Big Bang theory, the earliest stages of life of the Universe are characterized by an extremely hot and dense fluid. These conditions are ideal to trigger nucleosynthesis reactions that produce heavier nuclei, starting from protons, neutrons and electrons. Other than the CMB, this model can explain the observed helium abundances, which are hard to justify with stellar nucleosynthesis alone. The verification of the abovementioned predictions were the first, strong observational evidences that allowed the Big Bang model to be confirmed as the standard theory in modern cosmology.

Further observations led to the conclusion that the gravitational potential probed by dynamical observations (e.g. from galaxy rotation curves and temperature of hot gas in galaxy clusters) were in strong disagreement with the potential derived from light alone. The first proposals for the presence of an *obscure* kind of matter, which do not emit electromagnetic radiation, came in the early 1930s by Fritz Zwicky (Zwicky, 1933) and Jan Oort (Oort, 1932), who were studying respectively the Coma galaxy cluster and stellar motions in the local galactic neighborhood. In later years aditional observations on the gravitational lensing of background objects by galaxy clusters and, more recently, the pattern of anisotropies in the CMB confirmed the need for such *dunkle Materie*, as Zwicky called it. All of the above are considered probes of the presence of Dark Matter (DM) in the Universe, and gravitational collapse driven by gravitational instabilities in the DM distribution is commonly accepted to be the mechanism behind the formation of cosmic structures.

Along with dark matter, another ingredient of the current cosmological model is Dark Energy (DE). In 1998 the teams of Saul Perlmutter, Adam Riess and Brian Schmidt, studying the distribution with redshift of Supernovæ Ia (as standard candles), independently discovered that the expansion of the Universe is occurring at an accelerating rate (Riess et al., 1998; Perlmutter et al., 1999). This is at odds with the fact that gravity should slow down its expansion, due to the presence of matter. A full explanation of the mechanism behind the accelerating expansion of the Universe is still missing: in general, it is ascribed to an unknown DE component. The simplest interpretation for DE is that of a homogeneous fluid permeating the Universe, possibly related to vacuum energy: a cosmological constant Λ. Deviations of the w parameter in equation of state of DE ($p = w\rho$) from the simplest $w = 1$, would represent a departure from the standard ΛCDM model. The interpretation of DE as a cosmological constant poses some theoretical issues (discussed in more detail in chapter 3), that have prompted the formulation of several alternative theories, including evolving DE and modifications of GR. The nature of DE is one of the biggest open questions in modern physics, one that future experiments (in particular galaxy redshift surveys) will hopefully help to solve.

Our current understanding of the Universe relies then on the above discussed pillars, both theoretical and observational, which are the building blocks of the standard model of cosmology, the ΛCDM model. This model successfully predicts all observations so far, describing a Universe that is homogeneous and isotropic on large scales, where the gravitational interaction driving the growth of structures is described by GR, and where the energy content is dominated by DE and DM. In the short time span of a century, scientists gained an enormous amount of informations and were able to propose, test and discard different models. Indeed, thanks to both ground- and space-based observations such as galaxy surveys and CMB experiments, a wealth of extremely precise cosmological measurements now available allows to constrain the cosmological parameters to a high degree of precision, that will improve to reach percent level accuracy with the next generation of galaxy redshift surveys. This impressive achievements allow us to say that we are truly living in a golden era for cosmology.

The standard model, however successful, leaves some big open questions, like those on the nature of DM and DE and the mechanism behind inflation. The aim of current and future experiments is to investigate alternatives theories to the standard cosmological model, and possibly to find satisfactory interpretations of the dark components.

1.1 The metric of space-time

The evolution of the Universe is largely dominated by the gravitational interaction. Hence, cosmology requires a proper theory of gravity as its basic foundation. One such theory is Einstein's General Relativity, which passed a significant number of tests, from solar system (Will, 2014), to the prediction of the orbital decay of the Hulse-Taylor binary pulsar (Weisberg et al., 2010) and the gravitational wave emission (Abbott et al., 2016, 2017a,b). According to GR space-time is not a rigid stage upon which events "stay" or "happen", but rather a dynamic entity whose geometrical properties depend on the energy density (in all forms). This idea is summarized in Einstein field equations (Einstein, 1916):

$$G_{\mu\nu} = R_{\mu\nu} - \frac{1}{2} g_{\mu\nu} R = 8\pi G T_{\mu\nu} - g_{\mu\nu}\Lambda \tag{1.2}$$

where $R_{\mu\nu}$ is the Ricci tensor, R is the scalar curvature (the trace of $R_{\mu\nu}$), $g_{\mu\nu}$ is the metric of space time, and $T_{\mu\nu}$ is the stress-energy tensor that describes the distribution of energy and momentum across the Universe. To quote John Wheeler: *"Space tells matter how to move, matter tells space how to curve"*. A general solution to the above non-linear equation has yet to be found. Eq. 1.2 can however be simplified by considering the symmetries of the problem at hand, i.e. our understanding of the Universe. The simplest symmetry is the one provided by the cosmological principle, which states that on a sufficiently large scale (larger than $\sim 100\ h^{-1}$ Mpc) the Universe is isotropic and homogeneous. The most general metric for such Universe is the Friedmann-Lemaître-Robertson-Walker metric (Friedmann, 1922; Lemaître, 1931; Robertson, 1935; Walker, 1937):

$$ds^2 = dt^2 - a^2(t)\left[\frac{dr^2}{1-Kr^2} + r^2(d\theta^2 + \sin^2\theta d\phi^2)\right] . \tag{1.3}$$

where r, θ and ϕ are comoving spherical coordinates, K is the curvature of space-time, and $a(t)$ is the scale factor representing how the physical distance between two points scales with time. The value of K determines whether the Universe is open ($K < 0$), flat ($K = 0$) or closed ($K => 0$). Most recent measurements are consistent with a flat universe (Planck Collaboration et al., 2018; Alam et al., 2017). By inserting this metric in eq. 1.2, one can derive the first Friedmann equation:

$$\left(\frac{\dot{a}}{a}\right)^2 = \frac{8\pi G}{3}\rho - \frac{Kc^2}{a^2} + \frac{\Lambda c^2}{3} , \tag{1.4}$$

where $\rho = \sum_i \rho_i$ is the sum of the densities of each component of the Universe, with the cosmological constant having $\rho_\Lambda = \Lambda c^2/8\pi G$. Equation 1.4 states that the variation of the scale factor as a function of the cosmic time is dictated by the total amount of energy in the Universe (matter, radiation, curvature and DE). The quantity $\dot{a}/a$ is usually referred to as the Hubble factor $H(t)$, whose value evaluated today is just the Hubble constant H_0. By combining the first Friedmann equation with the equation for energy conservation, one can derive the evolution equation for the Hubble parameter, also known as the second Friedmann equation:

$$\frac{\ddot{a}}{a} = -\frac{4\pi G}{3}\left(\rho + 3\frac{p}{c^2}\right) + \frac{\Lambda c^2}{3} . \tag{1.5}$$

Equation 1.5 provides the mathematical formalism for the cosmic acceleration, that is produced by the balance between the energy density and the self-pressure of the fluid. In addition, each component evolves differently with time:

$$\rho_i = \rho_{i,0} a^{-3(1+w)} , \tag{1.6}$$

where w is the equation of state parameter: $w = 1/3$ for radiation, $w = 0$ for non-relativistic matter and $w = -1$ for the cosmological constant. One possible extension of the standard model includes a time-dependent w for DE, a possibility that will be probed by future surveys.

It is possible to re-write equation 1.4 incorporating Λ in ρ: this allows to identify a critical value for the density corresponding to $K = 0$, i.e. to a flat Universe:

$$\rho_{\rm cr}(t) = \frac{3H^2(t)}{8\pi G} \ . \tag{1.7}$$

By using this critical density, it is possible to define the dimensionless density parameters for the cosmic fluids as the ratio $\Omega = \rho/\rho_{\rm cr}$:

$$\begin{aligned} \Omega_m(a) &= \frac{\rho_m(a)}{\rho_{{\rm cr}(a)}} = \frac{\Omega_{m,0}H_0^2}{a^3H^2(a)} \quad , \quad \Omega_r(a) = \frac{\rho_r(a)}{\rho_{\rm cr}(a)} = \frac{\Omega_{r,0}H_0^2}{a^4H^2(a)} \\ \Omega_\Lambda(a) &= \frac{\rho_\Lambda(a)}{\rho_{\rm cr}(a)} = \frac{\Omega_{\Lambda,0}H_0^2}{H^2(a)} \quad , \quad \Omega_K(a) = \frac{\rho_r(a)}{\rho_{\rm cr}(a)} = -\frac{KH_0^2}{a^2H^2(a)} \end{aligned} \tag{1.8}$$

The latter allow to write the first Friedmann equation as

$$\frac{H^2(a)}{H_0^2} = E^2(a) = \Omega_{m,0}a^{-3} + \Omega_{r,0}a^{-4} + \Omega_{K,0}a^{-2} + \Omega_{\Lambda,0} \ , \tag{1.9}$$

highlighting the relationship between the evolution of the Universe and its energy content.

1.1.1 The standard model of cosmology

GR planted the seeds that would eventually grow into the current standard model of cosmology, the ΛCDM model. The latter is a parameterization of the Hot Big Bang model describing a spatially flat Universe, where the energy content is dominated by Cold Dark Matter (CDM) and a cosmological constant Λ, responsible for the late-time accelerated expansion. On the other hand, CDM drives the formation and growth of cosmic structures, and the attribute *cold* refers to the fact that it was non-relativistic at decoupling from other species. In the framework of the ΛCDM model the minimum set of parameters to account for currently available observations is:

- Ω_m, the matter (CDM and baryons) energy density parameter;
- Ω_b, the baryon energy density parameter;
- Ω_Λ, the cosmological constant energy density parameter;
- Ω_K, the curvature energy density parameter ($\Omega_K = 0$ for a flat universe);
- Ω_r, the radiation (photons and neutrinos) energy density parameter;

- H_0, the Hubble constant;
- A_s, the amplitude of primordial fluctuations;
- n_s, the spectral index of the power spectrum of the primordial curvature perturbations.

Different cosmological probes depend on the values of the above parameters, hence the former can be used to constrain the latter(§1.4). Although the ΛCDM model successfully fits all cosmological observations so far, the very idea that most of the energy content of the Universe is in some form of unknown dark components raises some concerns. Moreover, recent data have shown the presence of some tensions between the parameters inferred from early and late probes, namely CMB versus LSS and SNIa (see §3.1.2). Such tensions are possibly related to to some systematics in the data, or to unknown physics. Indeed, several modifications or extensions of GR and the standard model of particle physics have been proposed to explain the dark sector (§3).

Future generations of experiments including galaxy redshift surveys, such as Euclid [2] (Laureijs et al., 2011), DESI [3] (Levi et al., 2013), LSST [4] (LSST Science Collaboration et al., 2009) or WFIRST [5] (Spergel et al., 2013), aim at addressing these issues, and constrain cosmological parameters to higher precision.

1.2 A brief thermal history of the Universe

The first suggestion that the Universe is expanding, and thus it could have originated from a hot and dense primordial state, dates back to Alexander Friedmann and George Lemaître in the 1920s. Despite an early separation of the scientific community between supporters of the Big Bang theory and the steady state scenario, a wide range of observational evidence has brought to a common acceptance of the Big Bang as the starting point for the current Universe.

---

[2] `https://www.euclid-ec.org/`

[3] `https://www.desi.lbl.gov/`

[4] `https://www.lsst.org/`

[5] `https://wfirst.gsfc.nasa.gov/`

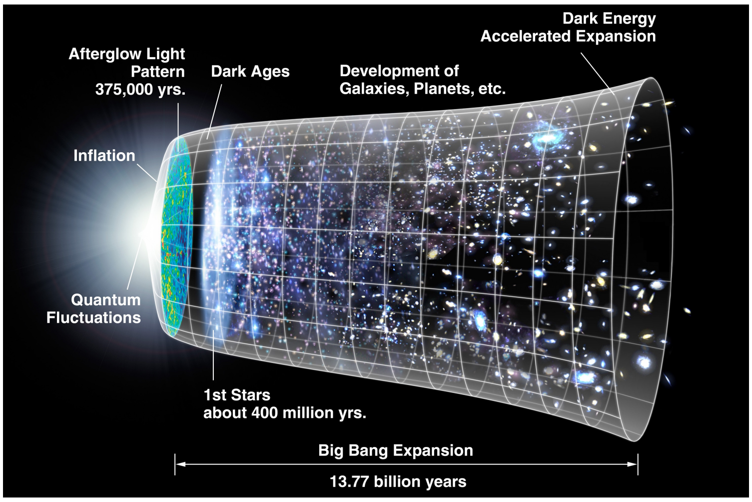

Fig. 1.2: A representation of the history of the Universe, starting from the seeds that are quantum fluctuations to today's accelerated expansion. *Credits: NASA/WMAP*

The presence of a hot, dense initial phase was later confirmed by the discovery of the CMB, a landmark evidence that the baryonic matter was completely ionized, and hence hot, in the early Universe. The thermal history of the Universe deals with the evolution of an expanding (and cooling) fluid, where the energy available for particle interactions slowly decreases over time. A knowledge of the rate of particle interactions is of crucial importance, for example in understanding the time at which each particle specie decouples from the primordial plasma. Decoupling occurs when the interaction rate for particles Γ drops below the Hubble rate H: at the very beginning, all particles are in thermal equilibrium enforced by frequent interactions. Then, as the Universe expands and cools down, their interaction rate decreases. The moment of decoupling depends on the type of particle and interaction, and is therefore different for each specie.

Currently we cannot access the extremely high energies present in the first phases of the Universe, hence our understanding of those interactions is possibly based on speculations or assumptions. Before 10^{-43} seconds from the Big Bang (or at energies above the Planck mass, $M_{\rm Pl}c^2 = 10^{19}$ GeV), the common understanding is that quantum effects should be incorporated. Soon after, inflation is supposed to take place at energies of about 10^{16} GeV, making the Universe exponentially expand by at least 26 orders of magnitude in size and boosting tiny quantum fluctuations to a large enough size to be the seeds for the current large scale structures. Inflation was introduced in the 1980s in works by Starobinskiĭ (1979), Guth (1981) and Linde (1982) to solve some problems related to background cosmology, namely the flatness, the horizon and the magnetic monopole problem. Several inflationary scenarios have been proposed over the years, and inflation is still one of the hot-topics in theoretical physics and cosmology (Mazumdar & Rocher, 2011; Martin et al., 2014).

After inflation, the Universe keeps expanding and cooling. The temperature of the fluid scales as

$$T \propto a^{-1} \ . \tag{1.10}$$

Neutrinos are kept in thermal equilibrium with the plasma by weak interactions, until their energy drops below $\sim$ 1 MeV (roughly one second after the Big Bang) and neutrinos decouple from the plasma. After decoupling, the temperature of neutrinos continue to decay as the inverse of the scale factor of the Universe. After about three minutes the energy has dropped to $\sim$ 0.1 MeV, allowing for the formation of the first nuclei (*Big Bang nucleosynthesis*, BBN). Modern BBN numerical codes can compute the abundance of light elements (H, ^4He, D, ^3He, ^7Li) to 1% precision (e.g. (Arbey, 2012)), with the number density fraction of baryons to photons $\eta = n_B/n_\gamma$ as the only parameter. The results can then be compared to observations and current constraints on η are

$$\eta = 4.6 - 5.9 \times 10^{-10} \ , \tag{1.11}$$

a very narrow range that indicates that there is about one baryon per 10^9 photons in the Universe today (Cyburt et al., 2016).

Up to this point, the evolution has been mainly driven by radiation, that dominates the energy content of the Universe. However, relativistic species have a density that scales as $\rho_r \propto a^{-4}$, while non-relativistic particles are pressure-less, hence $\rho_m \propto a^{-3}$. As a consequence there is a time when the two are equal: the *matter-radiation equality*. The redshift at which this happens can be estimated as:

$$1 + z_{eq} = \frac{a_0}{a_{eq}} = \frac{\Omega_{m,0}}{\Omega_{r,0}} \simeq 3 \times 10^4 \ \Omega_{m,0} h^2 \ . \tag{1.12}$$

Here a_0 is the scale factor today (usually normalized so that $a_0 = 1$). The exact value for z_{eq} depends on the density parameters for matter and radiation

(1.12), as well as on the mass of neutrinos.

As the Universe keeps expanding and cooling, electrons eventually bind to protons to form neutral hydrogen atoms. The photon mean free paths at this *recombination* epoch ($z_{\rm rec} \sim 1270$) suddenly increase up to the horizon scale (Peebles, 1968), making them free to stream and marking the transition of the Universe from opaque to transparent. It is at this epoch that the photons of what we measure today as Cosmic Microwave Background Radiation are emitted from the last scattering surface ($z_{\rm dec} \sim 1100$).

After recombination the Universe content is now divided into two non-interacting fluids: baryon and photons, with the photons no longer able to damp matter perturbations, and baryons free to collapse under their own self-gravity. Most importantly, baryons evolve under the gravitational pull set by DM perturbations that in the meantime have already started to grow. After a few hundreds of million years, the first stars start to form, marking the end of the Dark Ages and the beginning of the *re-ionization epoch*, thought to happen at $6 < z < 10$.

Starting from the equivalence at redshift $z \sim 10^4$, and up to re-ionization, the energy budget is dominated by matter. This is the epoch where structures in the Universe grow, finally forming the cosmic web that can be observed today via galaxy redshift surveys. Later on, at redshift $z < 1$, a new phase of accelerated expansion starts, prompted by an unknown mechanism dubbed Dark Energy.

1.3 Statistics of cosmic fields

According to observations, and in agreement with the cosmological principle, the Universe is nearly homogeneous and isotropic on very large scales. However, on scales smaller than galaxy superclusters, the structure of the Universe is highly inhomogeneous. On such scales the matter distribution is clumpy, as shown both by CMB experiments and galaxy redshift surveys, and form over-dense and under-dense regions that are organized in a *cosmic web* (see e.g. Fig. 1.3). The widely accepted model to explain the formation of structures in the Universe is that the latter are the result of the growth of primordial small-scale seeds, generated in the early Universe by quantum fluctuations of a scalar field and grown under gravitational instability, as described in §1.2. As a consequence, the present day matter distribution car-

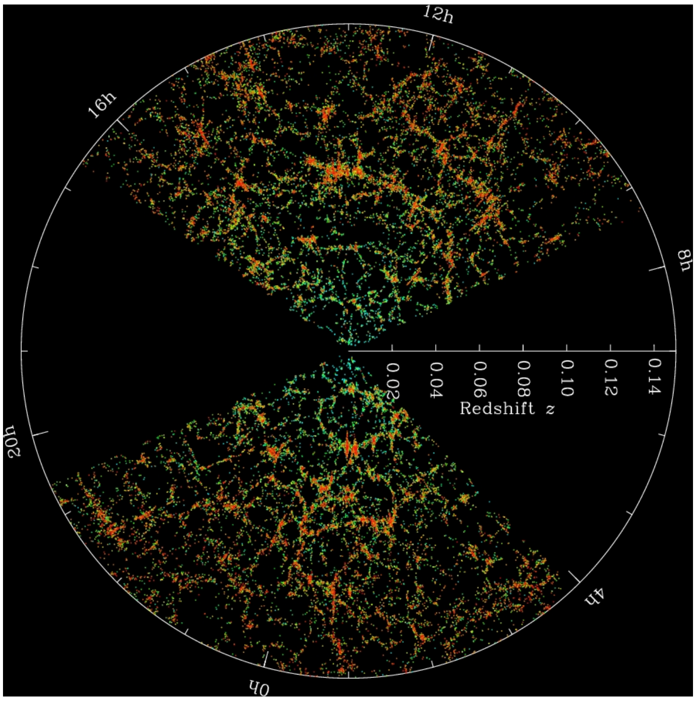

Fig. 1.3: The spatial distribution of galaxies observed by the SDSS survey. The observer is at the center, and the lightcones are projected along the DEC direction in order to get a 2d image as a function of redshift and right ascension. The cosmic web can be clearly identified, consisting of filaments, sheets, clusters and voids. *Credits: M. Blanton - SDSS*

ries information about the initial fluctuations that are the seed for the Large Scale Structure, hence it is possible to exploit it to test different cosmological scenarios. Such studies would however be statistical in their nature, since

- a deterministic description of the evolution would require having direct access to the primordial fluctuations. The latter are however not observationally reachable, thus we cannot get the initial conditions to solve the evolution equations;
- it is not possible to directly follow the time evolution of the fluctuations, owing to the long time-scale for cosmological evolution.

The common approach is therefore to consider our Universe as a single stochastic realization out of all possible realizations (i.e. universes). It is possible to consider cosmic scalar fields, as the cosmic density field, the velocity field, or the gravitational potential, for which one can predict statistical quantities, and compare the latter to statistics derived from observations.

We can thus think of our Universe as a realization of a random field $\psi(\vec{r}, t)$ with probability density function $P(\psi)$. Cosmic random fields are usually assumed to be statistically homogeneous and isotropic, i.e. their probability distribution functions are invariant under translation of the spatial coordinates and under rotations. Such random fields are used to describe fluctuations in the distributions of different quantities, such as galaxies or matter, with respect to a smooth background. As already discussed, theoretical investigation allows one to compute statistical quantities averaged over the ensemble of all possible realizations, for istance the first moment and variance of this field. Performing such average should in principle require the availability of several realizations (i.e. universes). The problem can be circumvented if one makes the *ergodic hypothesis*: if the sampled volume is large enough, a *fair sample*, the mean value determined over all universes can be replaced by a space average calculated over the available volume. For our purposes, the required random fields are the density contrast of the matter continuous field δ, and of the galaxy field δ_g:

$$\delta(\vec{r}, t) = \frac{\rho(\vec{r}, t) - \bar{\rho}(t)}{\bar{\rho}(t)} , \tag{1.13}$$

$$\delta_g(\vec{r}, t) = \frac{n(\vec{r}, t) - \bar{n}(t)}{\bar{n}(t)} , \tag{1.14}$$

where ρ is the matter density and n is the galaxy number density, and the barred quantities are the respective mean values.

1.3.1 Two-point statistics

One of the most important statistical quantities describing the spatial distribution of objects in the Universe is the two-point correlation function (2PCF):

$$\xi(r) = \langle \delta(\vec{x}) \delta(\vec{x} + \vec{r}) \rangle , \tag{1.15}$$

where δ is the density of a generic proxy for the total matter density field. The 2PCF represents the excess probability of finding a pair of objects at distance r respect to a random distribution, hence it is a measurement of the amplitude of clustering.

The fact that $\xi(r)$ only depends on the magnitude of $\vec{r}$ is a consequence of the assumptions of homogeneity and isotropy. Such feature no longer holds for redshift-space measurements (§1.4.2), affected by peculiar motion of galaxies. Moreover, performing a proper mapping between the underlying matter distribution a given tracer for matter is not trivial: galaxy redshift surveys measure the distribution of galaxies, while theoretical treatments can only predict matter statistics. The galaxy distribution is indeed assumed to be a proxy for the matter distribution; the two correlation functions $\xi_g(r)$ and $\xi_m(r)$ are therefore linked by the so-called *bias*. A careful modeling of the non-trivial bias relation between luminous and dark matter is then required when going from $\xi_m(r)$ to $\xi_g(r)$ and vice-versa.

A common and useful way of treating density fluctuations is to imagine them as waves that propagate in the Universe: in this way they can be decomposed into different wavelengths, each accounting for a different scale. The equivalent of the correlation function in Fourier space can be obtained by taking the Fourier transform of the density field $\delta_{\vec{k}}$ and computing the correlation between two waves with different wavevectors $\vec{k}_1$ and $\vec{k}_2$:

$$\langle \delta_{\vec{k}_1}\, \delta_{\vec{k}_2} \rangle = \left\langle \int \frac{\mathrm{d}^3\vec{x}_1}{(2\pi)^3}\, \delta(\vec{x}_1)\, e^{-i\vec{k}_1\cdot\vec{x}_1} \int \frac{\mathrm{d}^3\vec{x}_2}{(2\pi)^3}\, \delta(\vec{x}_2)\, e^{-i\vec{k}_2\cdot\vec{x}_2} \right\rangle \,. \tag{1.16}$$

By substituting $\vec{x} = \vec{x}_1$ and $\vec{r} = \vec{x}_2 - \vec{x}_2$ in eq. 1.16:

$$\begin{aligned} \langle \delta_{\vec{k}_1}\, \delta_{\vec{k}_2} \rangle &= \int \frac{\mathrm{d}^3\vec{x}}{(2\pi)^3} \int \frac{\mathrm{d}^3\vec{r}}{(2\pi)^3}\, e^{-i(\vec{k}_1+\vec{k}_2)\cdot\vec{x}}\, e^{-i\vec{k}\cdot\vec{x}}\, \langle \delta(\vec{x})\, \delta(\vec{x}+\vec{r}) \rangle = \\ &= \delta_D(\vec{k}_1+\vec{k}_2) \int \frac{\mathrm{d}^3\vec{x}}{(2\pi)^3}\, e^{-i\vec{k}\cdot\vec{r}}\, \xi(r) \,, \end{aligned} \tag{1.17}$$

where $\xi(r)$ is the correlation function and δ_D is the Dirac delta function. It can be seen from eq. 1.17 that two waves with different wavelength are not correlated in Fourier space. Eq. 1.17 can be written in a different form:

$$\langle \delta_{\vec{k}_1}\, \delta_{\vec{k}_2} \rangle = (2\pi)^3\, \delta_D(\vec{k}_1+\vec{k}_2)\, P(k_1) \,. \tag{1.18}$$

The new quantity introduced here is the *power spectrum* $P(k) = \langle |\delta_{\vec{k}}|^2 \rangle$, i.e. the Fourier transform of the correlation function.

1.3.2 Covariance matrices

The clustering statistics described in the previous section are sensitive to the underlying cosmology, and are therefore the main quantites considered when constraining cosmological parameters. The determination of cosmological parameters and the associated confidence levels is a task usually performed through a maximum likelihood analysis: theoretical predictions for the cosmological observable under scrutiny are computed and compared to data. Under the assumption of a Gaussian likelihood $\mathcal{L}$, the best fit model is the one that minimizes:

$$-2\ln\mathcal{L} = \sum_{i,j}(y_i^{\mathrm{d}} - y_i^{\mathrm{m}})C_{ij}^{-1}(y_j^{\mathrm{d}} - y_j^{\mathrm{m}}) \ , \tag{1.19}$$

where the sum runs over the data points, d and m stand for data and model respectively and C_{ij}^{-1} is the precision matrix, i.e. the inverse of the covariance matrix.

The latter can be sampled from a set of independent realizations N_r as:

$$C_{ij} = \frac{1}{N_r - 1}\sum_{n=1}^{N_r}(y_{n,i} - \bar{y}_i)(y_{n,j} - \bar{y}_j) \ , \tag{1.20}$$

where $\bar{y} = 1/N_r \sum_{i=1}^{N_r} y_i$ is the average of the observable over all realizations. Diagonal elements of the covariance matrix represent the square deviations of measurements from the mean value, while off-diagonal elements provide information on the correlation between different scales. Usually, the fitting procedure is carried out with a Markov Chain Monte Carlo (MCMC) approach, based on a likelihood-dependent sampling of the likelihood itself throughout the parameter space. The MCMC is required to sample the multi-dimensional parameter space in an efficient way. The final result of the analysis is a density map of the parameter space, corresponding to a multi-dimensional likelihood which is marginalized over to find the best fit for the parameters.

Future generations of LSS surveys will provide a large amount of high precision data (e.g. §1.5), with the potential to constrain cosmological parameters to % precision, on the condition that systematics are kept under control. Modeling the errors on cosmic statistics is indeed as fundamental as the determination of the cosmic statistics itself, making a proper estimation of the covariance matrix C_{ij} essential. Since a finite sampling of C_{ij} would result in the propagation of statistical sampling errors into the cosmological parameter inference, potentially limiting the capabilities of upcoming surveys, such a task requires the generation of large sets of simulations. The impact of finite sampling on the estimated covariance matrix was investigated within the Euclid collaboration by Lippich et al. (2019); Blot et al. (2019); Colavincenzo et al. (2019), showing that $\sim$2000-3000 realizations are needed. Moreover, the simulations should properly take into account halo/galaxy bias, redshift space distortions, and accurately model non-linear clustering. The selection function of the survey, defining its geometry and the galaxy sample, should also be included in the analysis.

Such a task is unfeasible with computationally demanding N-body simulations (§2.2.1. A possible solution is provided by approximate methods, described in §2.2.2, able to generate the required large sets of realizations in a fraction of the time with respect to full N-body simulations.

1.4 Cosmological observables and current constraints

In this section I give a brief summary of cosmological observables, as well as a (non-comprehensive) list of current constraints on ΛCDM parameters.

1.4.1 The Cosmic Microwave Background

CMB experiments aim at observing the last scattered photons, whose spectrum is that of a black body at 2.7 K (Fig. 1.4, right panel). This is indeed the most perfect black body spectrum observed in nature: the CMB is extremely isotropic and homogeneous, except for very small fluctuations in the temperature $\Delta T/T \sim 10^{-5}$, that can be clearly seen in the left panel of Fig. 1.5. CMB anisotropies can be divided into two categories: those originating at the epoch of last scattering, called primary anisotropies, and the ones due to interactions of the photons on their way to the observer, called secondary anisotropies. The main primary anisotropies are acoustic oscillations and collisionless damping. Acoustic oscillations arise because of a conflict between the gravitational interaction (that makes overdensities collapse) and the photon pressure (that tends to erase the anisotropies), and appear in the CMB temperature power spectrum as peaks and troughs. Collisionless - or Silk - damping is instead a suppression in the tail of the power spectrum, due to the increase in the mean free path of photons and the fact that the last scattering surface is not really a surface, but more of a *shell* with a finite

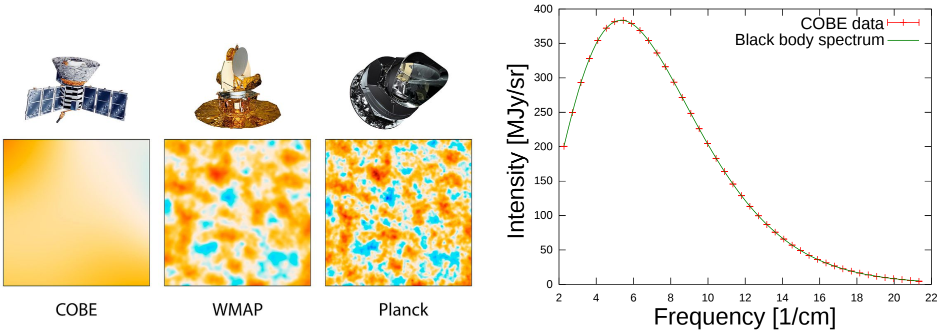

Fig. 1.4: *Left*: Evolution of CMB observations over two decades, showing the increasing resolution. Each panel shows 10 deg^2 patches of all-sky maps produced (left to right) with COBE, WMAP and Planck satellites *NASA/JPL-Caltech/ESA*. *Right*: Black body spectrum of the CMB as measured by the COBE satellite (Mather et al., 1994).

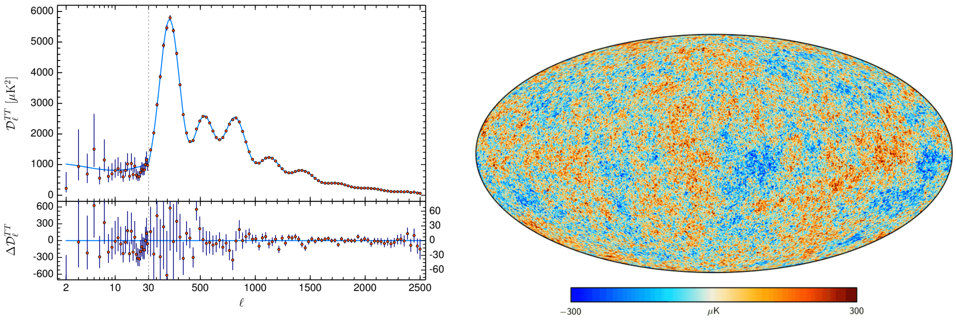

Fig. 1.5: *Left*: Temperature power spectrum of the CMB (Planck Collaboration et al., 2018). *Right*: CMB temperature map (Planck Collaboration et al., 2014).

depth (i.e., decoupling is not instantaneous). Secondary anisotropies, on the other hand, involve interactions of photons with the inter-galactic medium (Sunyaev-Zeldovich effect and Sachs-Wolfe effect).

Current constraints

Ever since its discovery, many experiments have been dedicated to studying the CMB. The most remarkable among these are three satellite missions: COBE, launched by NASA in 1980, WMAP, also a NASA satellite launched in 2002, and ESA's Planck, launched in 2009. The main results of these experiments are:

- the Universe is highly homogeneous and isotropic on large scales;

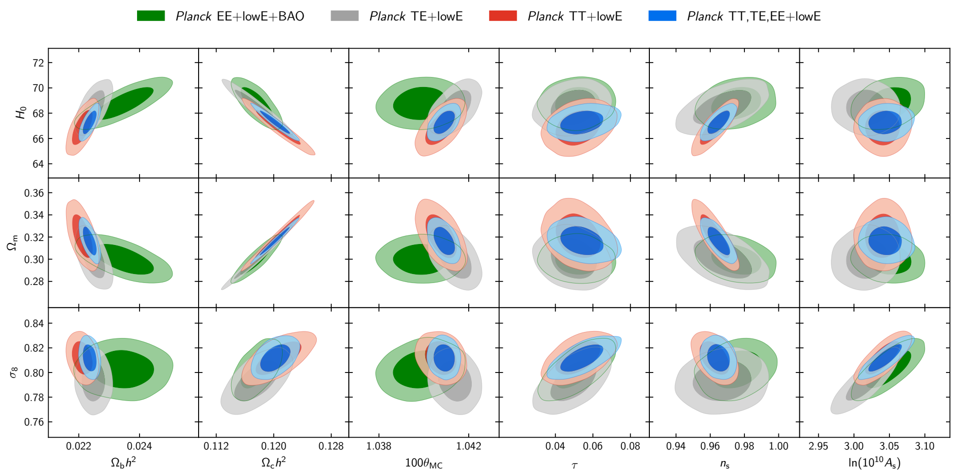

Fig. 1.6: One- and two-σ contours for the cosmological parameters of ΛCDM for different combinations of the data sets. From Planck Collaboration et al. (2018)

- there are small temperature fluctuations $\sim 10^{-5}$, likely being the seeds for today's LSS;
- the peak features in the CMB power spectrum can be exploited to put tight constraints on the cosmological parameters.

The most precise constraints to date on the cosmological parameters from CMB experiments are those provided by the Planck satellite in its 2018 Legacy release (Planck Collaboration et al., 2018), summarized in table 1.1 and Fig. 1.6. Such results show no significant deviations from the standard ΛCDM model.

$\Omega_b h^2$	0.02237 ± 0.00015
$\Omega_m h^2$	0.1200 ± 0.0012
$100\theta_*$	1.040909 ± 0.00031
τ	0.0544 ± 0.0073
$\ln(10^{10} A_s)$	3.044 ± 0.014
n_s	0.9649 ± 0.0042

Table 1.1: Constraints on parameters of base ΛCDM, from Planck Collaboration et al. (2018)

1.4.2 Galaxy redshift surveys

Galaxy redshift surveys aim at scanning large patches of the sky, in order to determine the spatial distribution of objects, such as galaxies or galaxy clusters. The goal of this kind of measurements is to make statistic measurements akin to those described in §1.3 and shown in Fig. 1.8. Such measurements of the clustering of objects in the Universe, as already discussed, allow to constrain the cosmological parameters.

The actual 3-dimensional position of galaxies is determined reconstructing their positions from redshifts. The latter can be either spectroscopic, if measured by means of a spectrograph, or photometric, if redshifts are derived from broad-band colors. The latter, suffer however from uncertainties that are roughly one order of magnitude larger than those on the spectroscopic redshifts: this is why the advent of multi-object spectrographs has been crucial in the recent advances in galaxy redshift surveys.

Constraining the comoving matter power spectrum from observed galaxies requires understanding and modeling a number of effects, both physical like Baryon Acoustic Oscillations (BAOs), or the bias linking the galaxy distribution to the underlying matter one, and observational, such as Redshift Space Distortions (RSDs) and the Alcock-Paczynski effect.

Redshift space distortions

The velocities of galaxies are caused both by the expansion of the Universe and their peculiar motion, so that the galaxy position can be written as:

$$\vec{s}(\vec{r}) = \vec{r} - v_r(r)\hat{r} \ , \tag{1.21}$$

where $\vec{s}$ is the redshift-space position of the galaxy, while $\vec{r}$ is the true position and v_r is the radial component of the peculiar velocity. RSDs are due to:

- coherent motion due to the infall of galaxies into matter overdensities (linear effect, Kaiser (1987)). This determines an apparent squashing of structures along the line of sight (left in Fig. 1.7) on the largest scales;
- random motion of galaxies inside clusters (non-linear effect, also known as Finger-of-God) . This results in an elongation of structures along the line of sight (right in Fig. 1.7).

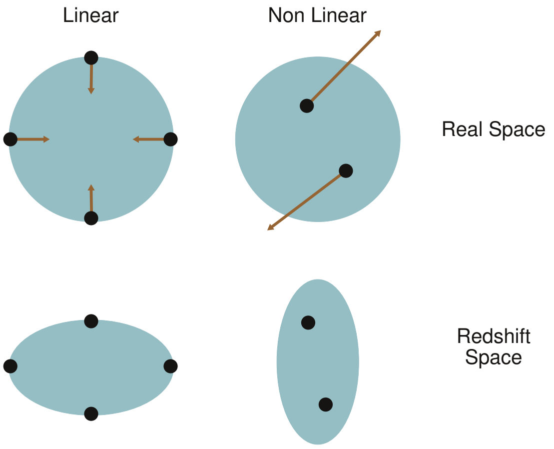

Fig. 1.7: Effect of peculiar motions of galaxies on their apparent position.

These effects result in anisotropic two-point functions (both the correlation function and the power spectrum). The common approach to describe the linear, Kaiser effect is to write the power spectrum as

$$P^s_{m,\mathrm{lin}}(\vec{k}) = (1 + f\mu^2)^2 P_{m,\mathrm{lin}}(k) \tag{1.22}$$

where the superscript s stands for quantities in redshift space, $f = \mathrm{d}\ln D/\mathrm{d}\ln a$ is the logarithmic derivative of the linear growth factor and μ is the cosine of the angle between the wavevector $\vec{k}$ and the line of sight. To calculate the galaxy power spectrum one must make some prescriptions for the bias: under the simplest assumption of linear bias $\delta_g = b\delta_m$, and defining a distortion parameter $\beta = f/b$, the galaxy power spectrum can be written as:

$$P^s_{g,L}(\vec{k}) = b^2(1 + \beta\mu^2)^2 P_{m,L}(k) \tag{1.23}$$

The treatment of the non-linear Finger-of-God effect is more complicated. One possibility is to treat it in a phenomenological way, including a damping factor that plays the role of a pairwise velocity distribution, as proposed in the dispersion model by Peacock & Dodds (1994) and later extended by Scoccimarro (2004). A more recent model, widely used in RSDs analysis today, is the so-called TNS model, described in Taruya et al. (2010).

The anisotropic redshift-space power spectrum is generally expanded as:

$$P^s(k,\mu) = \sum_l P_l^s(k)\mathcal{L}_l(\mu) \; , \tag{1.24}$$

where $\mathcal{L}_l$ are the Legendre polynomials and

$$P_l^s(k) = \frac{2l+1}{2}\int_{-1}^{+1} d\mu P^s(k,\mu)\mathcal{L}_l(\mu) \tag{1.25}$$

are the expansion multipoles. The same procedure can be applied to the correlation function, so that redshift-space quantities are usually expressed in terms of the monopole, quadrupole, and exadecapole.

A proper description of RSDs is of crucial importance to extract cosmological informations from the clustering signal. However cumbersome, an accurate modeling of RSDs can actually help in constraining cosmological parameters and breaking degeneracies (Percival & White, 2009). In particular, RSDs are sensitive to the growth of perturbations, as is clearly seen by the dependence on f in equation 1.22, and are usually employed to constrain the combination between f and σ_8 (standard deviation of the overdensities distribution, when averaged over a sphere of radius 8 Mpc h^{-1}), as shown in Fig. 1.10. Recent works showed that measurements in redshift space can also be exploited to break the degenerate effects of massive neutrinos and modified gravity on the two-point statistics (Hagstotz et al., 2019; Wright et al., 2019).

Baryon acoustic oscillations

BAOS are oscillations in the density of baryonic matter due to the counteracting forces of gravity in a collapsing overdensity, as opposed to the pressure of photons. They provide a standard ruler for cosmology whose size is set by the maximum distance that acoustic waves can travel in the plasma before decoupling, the sound horizon size. Baryon acoustic oscillations show up as a characteristic peak feature in the CMB, as well as in the galaxy two-point correlation function as a distinct “bump” at $\sim 110\ h^{-1}$ Mpc, or as “wiggles” in the galaxy power spectrum (see Fig. 1.8). The BAO signal was first detected in the CMB by WMAP, and later from the galaxy 2PCF of SDSS (Eisenstein et al., 2005). By comparing the BAO scale at recombination (observed from

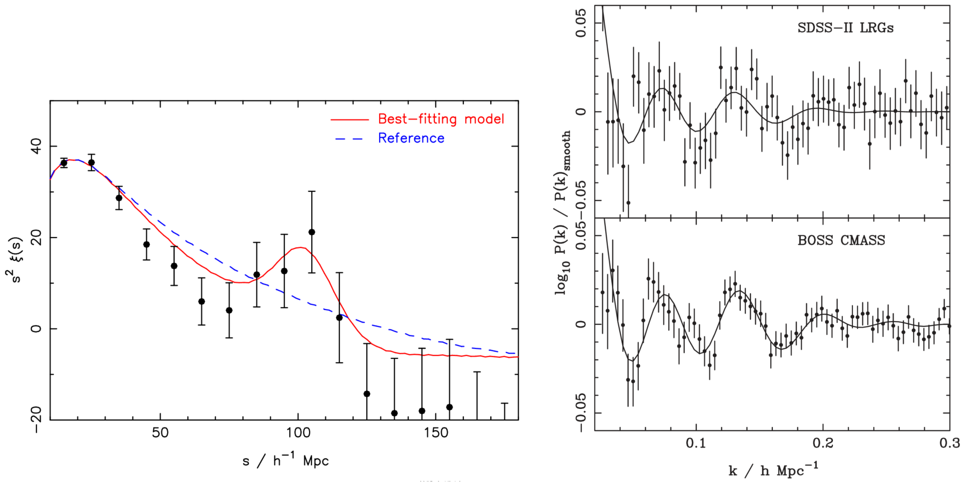

Fig. 1.8: *Left*: Two point correlation function from the WiggleZ survey (Blake et al., 2011). Black dots are data points, the solid red line is the best fitting model that includes BAOs, while the dashed blue line represents a model without baryons. *Right*: Power spectrum from SDSS-II LRG data and CMASS data (points in upper and lower panel respectively), solid lines represent the best-fitting models (Anderson et al., 2012).

the CMB) to its size today (measured from galaxy surveys) it is possible to study the expansion history of the Universe.

Alcock-Paczynski effect

We measure redshift, but want distances. Those are evaluated by making assumptions on the cosmology (specifically $H(z)$), so if the cosmology is wrong, there are distortions in the clustering signal: these are usually taken into account with the Alcock-Paczynski test (Alcock & Paczynski, 1979). The most robust source to perform the Alcock-Paczynski test is the BAO signal, since it is a distinct feature appearing on sufficiently large scales (free from effects of non-linear physics). Typically, the relevant parameters are:

$$\alpha_\perp = \frac{D_A(z) r_d^{\rm fid}}{D_A^{\rm fid} r_d} \quad , \qquad \alpha_\parallel = \frac{H^{\rm fid}(z) r_d^{\rm fid}}{H(z) r_d} \ , \tag{1.26}$$

where fid is the fiducial cosmological model assumed to convert redshifts to distances, r_d is the comoving BAO scale and $H(z)$ is the Hubble rate.

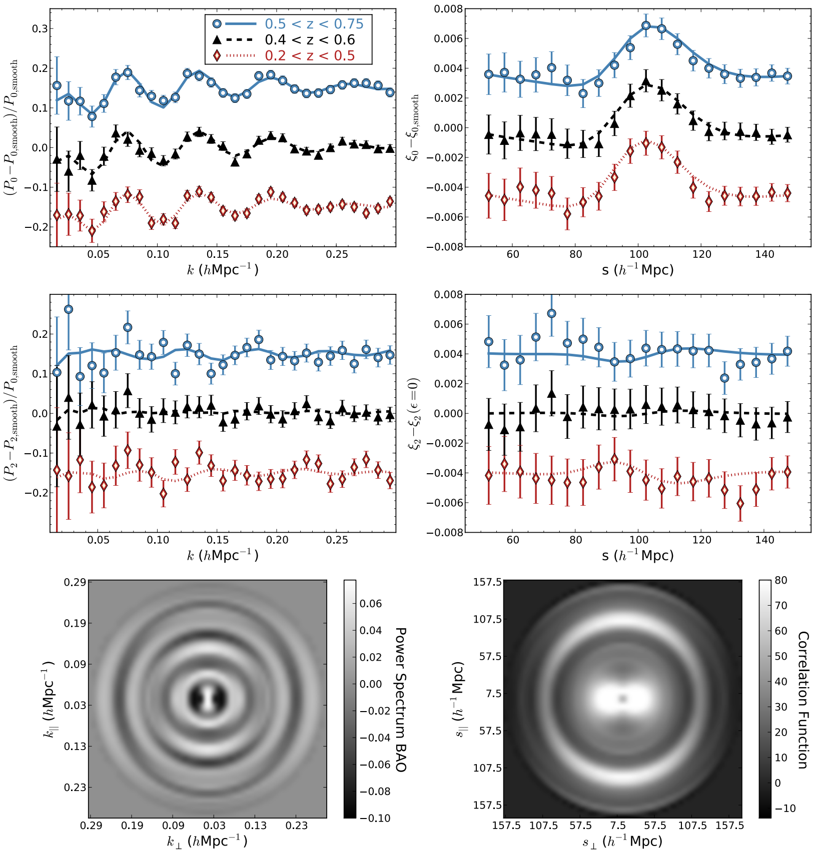

Fig. 1.9: Power spectrum (*left*) and two-point correlation function (*right*) multipoles from BOSS (Alam et al., 2017). The top row shows the monopole, while the middle row shows the quadrupole. In the bottom rows are shown the power spectrum and correlation function decomposed into transverse to and along the line of sight components.

Current constraints

Redshift surveys started at the end of the 1970s with the CfA redshift survey, followed by the 2dF Galaxy Redshift Survey (2dFGRS, Colless et al. (2003)), and the Sloan Digital Sky Survey (SDSS, York et al. (2000)), whose stage III included the Baryon Acoustic Oscillation Survey (BOSS, Alam et al. (2017)). The SDSS is now in its stage IV, with the extended Baryon Acoustic Oscillation Spectroscopic Survey (eBOSS) focused on studying BAOs at redshifts $0.6 < z < 2.5$. Fig. 1.9 shows recent measurements on the redshift-space two-point statistics (power spectrum, on the left, and 2PCF, on the right) for different redshift bins (Alam et al., 2017). The redshift-

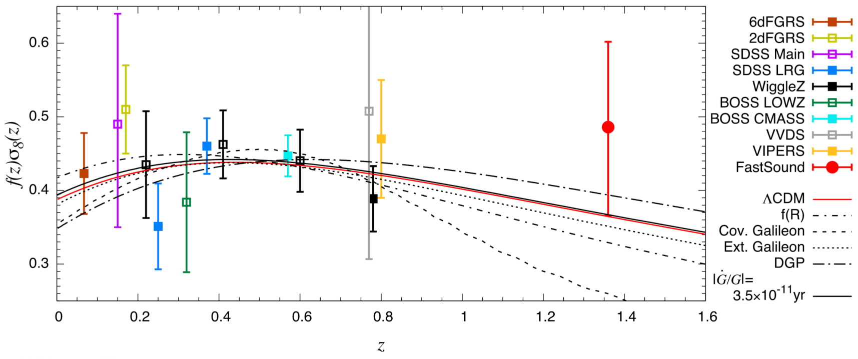

Fig. 1.10: Summary of the constraints on the measurement of the growth factor $f\sigma_8$ from different redshift surveys are shown as points with errorbars. The ΛCDM prediction is shown as a solid red line, while predictions for some modified gravity models are shown as black lines. From Okumura et al. (2016).

space induced anisotropy is clearly evident in the bottom row. Considering the standard ΛCDM scenario, BOSS data constrain $\Omega_m = 0.3110 \pm 0.005$, $H_0 = 67.06 \pm 0.5 \text{ km s}^{-1} \text{ Mpc}^{-1}$, and no significant evidence for non-flat ($\Omega_K \neq 0$) or evolving DE ($w_{DE} = w(a)$) cosmologies.

Fig. 1.10 summarizes measurements of the growth factor $f\ \sigma_8$ from different redshift surveys (Okumura et al., 2016). While all datasets are consistent with the standard ΛCDM scenario (solid red line), it is clear that the uncertainty on the measurements do not allow to disentangle between extensions of the standard model (dashed black lines). As discussed in the next section, the precise measurements that will be provided by the future Euclid survey will allow to discriminate between different models.

1.5 The Euclid Satellite

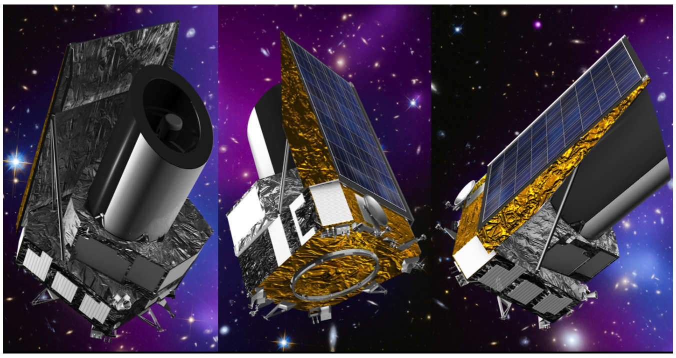

Fig. 1.11: Artist's view of the Euclid satellite. *Credits: ESA*

One of the future experiments that will help in tightening the constraints on cosmological parameters, as well as testing possible alternatives to the ΛCDM model, is the Euclid mission. The latter is a medium class space mission of ESA cosmic vision 2015-2025 program, selected for funding in 2011 and planned for launch in 2022. The satellite will travel to the L2 Sun-Earth Lagrangian point for a 6 years long mission.

The main science goal for Euclid (Laureijs et al., 2011; Amendola et al., 2018a) is to understand the mechanism behind the accelerated expansion of the Universe, by studying the expansion history and evolution of the Large Scale Structure. The imprints of DE and of the gravitational interaction will be traced by two main probes: Galaxy Clustering, through observations of BAOs and RSDs, and Weak Lensing. To this purpose, Euclid will measure redshifts and shapes of galaxies up to $z \sim 2$, covering 15000 deg^2 of the sky free of contamination by light from our Milky Way galaxy and zodiacal light. Moreover, there will be three *Euclid Deep Fields* covering around 40 deg^2 in total, extending the scientific scope of the mission to the high-redshift Universe. The two main probes will also be complemented by a number of additional probes, including abundance and properties of galaxy clusters, strong lensing and cross-correlation between CMB and Large Scale Structure.

The satellite will be equipped with a 1.2 m diameter, three-mirror telescope, that feeds two instruments to cover visible and near-infrared wavelengths. In the optical, a visible imager (VIS) will provide high-resolution (pixel resolution of 0.1 arcseconds) images with a wavelength range $500-800$ nm. In the near-infrared, a 3-filter photometer (NISP-P) will deliver im-

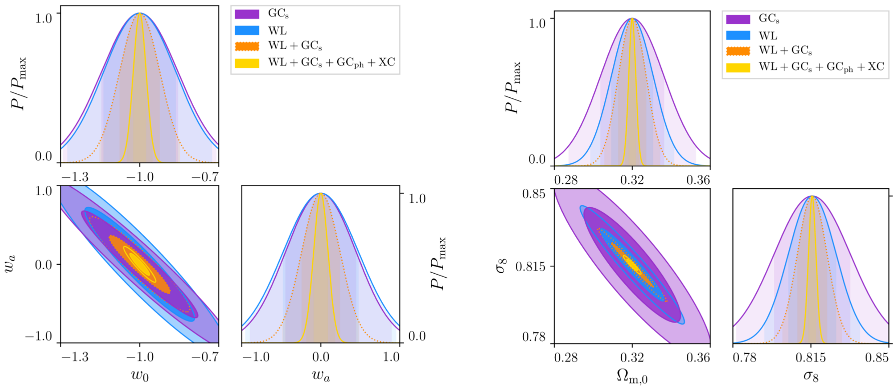

Fig. 1.12: Fisher forecasts for w_0, w_a (left) and Ω_m, σ_8 (right). From Euclid Collaboration et al. (2019)

ages in Y, J and H bands with a pixel resolution of 0.3 arcseconds, while slitless spectrography will be performed by NISP-S with two different filters: a *blue grism* $(920 - 1250$ nm), and a *red grism* $(1250 - 1850$ nm). These instruments will measure the 3D distribution of structures in the Universe from spectroscopic redshifts of galaxies and clusters of galaxies as well as the modification of shapes of galaxies induced by gravitational lensing effects.

The complete survey will feature billions of images and several tens of Petabytes of data. About 10 billion sources will be observed by Euclid out of which approximately 2 billions will be used for weak lensing, while about 30 millions of galaxy redshifts will be measured, and used for galaxy clustering.

Euclid will measure cosmological parameters with percent precision. In particular, the target precision for w in the DE equation of state is 1% for w_0 and 10% for w_a, tightly constraining evolving DE models. Fig. 1.12 shows forecasted constraints on the DE equation of state parameters (left triangular plot) and on Ω_m and σ_8 (right triangular plot). Different colors show different probes, as well as combinations of them. Fig. 1.13 shows the growth rate f as a function of redshift. The forecast for Euclid are shown as points with error-bars, while different lines refer to different modified gravity models (ΛCDM is plotted as a green line). The improvement with respect to currently available data (e.g. fig. 1.10) is evident, confirming the ability of Euclid data to disentangle between different gravity models.

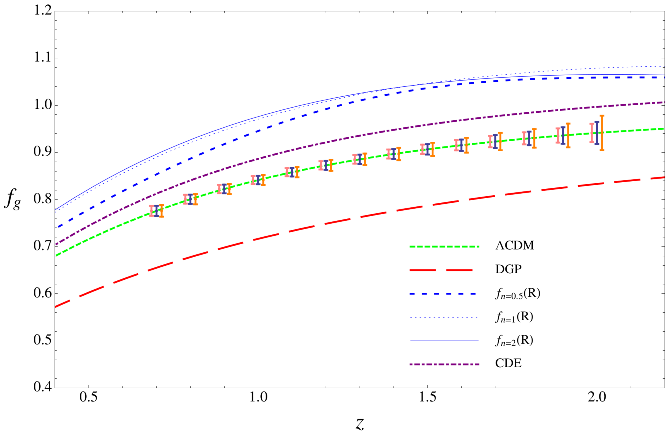

Fig. 1.13: Expected constraints on the growth rate for Euclid, points with error bars. Shown with lines are predictions for different models, including some modified gravity models (described in§3). From Amendola et al. (2018a)

Chapter 2

The evolution of perturbations

As discussed in the previous chapter, the Universe is nearly homogeneous and isotropic on very large scales. A closer look at how galaxies are distributed in the Universe reveals the presence of a cosmic web of filaments, walls and voids. As motivated in §1.3, one can merely give a statistical description of the cosmic web. Nonetheless it is crucial to make predictions for various observables in the context of different cosmological models, in order to extract informations from cosmological observations. In particular we need a theory for structure formation able to predict the statistics of cosmic fields. The commonly accepted picture for the formation of cosmic structures is the *hierarchical scenario*, where the current LSS emerge from a hierarchical, gravitationally driven assembly of smaller DM structures (halos), originated by primordial small-scale fluctuations. These structures merge to form larger and larger halos, generating the potential wells in which baryons eventually fall, and form stars and galaxies. Although the details of the formation of structures are affected at small scales by the physics of baryons, in the context of a universe where the dominating matter component is DM the global properties of the large scale distribution are determined by the collisionless dynamics of DM itself.

The latter can be approximated linearizing the equations describing the DM dynamics, an approach that can be safely adopted only under the assumption that densities and velocities are small. This approximation is, however, not suitable to follow the evolution of structures deeply into the non-linear regime. One possibility is to adopt a perturbative approach, which allows one to push predictions to mildly non-linear scales, such as the BAO scale. The advantage of such techniques is their quick computability. The fully non-linear scales however cannot be described with a perturbative method, because of highly non-linear dynamics and other small-scale phenomena (such as baryonic effects). These scales can only be accurately described with cosmological N-body simulations, which are however computationally expensive. For this reason, an alternative way (useful in particular for the computation of covariance matrices, §1.3.2) is provided by approximate methods that can quickly generate large sets of realizations of the density fields.

In this chapter I provide an overview of the numerical approaches currently used to predict cosmological quantities. Thorough and comprehensive reviews can be found in Bernardeau et al. (2002) (for perturbative approaches to cosmic growth), Bertschinger (1998) (for cosmological N-body simulations) and Monaco (2016) (for approximate methods).

2.1 Perturbative approach to cosmic growth

The evolution of the density field can be described approximating the Universe with an expanding perfect fluid. Such an approximation holds when the scales considered are much smaller than the particle horizon ($k \ll H$) and the velocities are much smaller than the speed of light ($v_p \ll c$): in this case we can adopt a Newtonian approximation, able to account for the linear regime of perturbations.

Most of the evolution and growth of cosmic structure occurs during the matter dominated era. Hence, in the following, I will neglect the contribution of Λ to the background evolution. This is equivalent to considering a universe that only includes matter, i.e. an Einstein-de Sitter universe. The physical coordinate $\vec{r}$ can be described in terms of a comoving coordinate $\vec{x}$ times the scale factor:

$$\vec{r}(t) = a(t)\vec{x}(t) \ . \tag{2.1}$$

The velocity of perturbations can then be written as:

$$\vec{v} = \frac{\mathrm{d}\vec{r}}{\mathrm{d}t} = \dot{a}\vec{x} + a\frac{\mathrm{d}\vec{x}}{\mathrm{d}t} = Ha\vec{x} + \vec{u} = H(t)\vec{r}(t) + \vec{u}(t) \ . \tag{2.2}$$

where $H\vec{r}$ denotes the Hubble flow and $\vec{u}$ is the peculiar velocity. It is useful to change the time coordinate to the conformal time τ, where $\mathrm{d}\tau = \mathrm{d}t/a$, and introduce a conformal Hubble factor $\mathcal{H}(\tau) = \mathrm{d}a/(a\,\mathrm{d}\tau) = aH$, so that

$$\vec{v}(\vec{x}, t) = \mathcal{H}\vec{x} + \vec{u} \tag{2.3}$$

The assumption of perfect fluid implies that the evolution of the density field is described by just three fluid equations: the continuity equation, Euler equation and Poisson equation,

$$\begin{aligned}
&\frac{\partial \rho}{\partial t} + \nabla_r \cdot (\rho \vec{v}) = 0 \\
&\frac{\partial \vec{v}}{\partial t} + (\vec{v} \cdot \nabla_r)\vec{v} = -\frac{1}{\rho}\nabla_r P - \nabla_r \Phi_{\mathrm{tot}} \\
&\nabla_r^2 \Phi_{\mathrm{tot}} = 4\pi G \rho
\end{aligned} \tag{2.4}$$

where ρ is the density, $\vec{u} = \dot{r}$ is the proper velocity, P is the pressure and Φ_{tot} is the gravitational potential. Here I am making the *one fluid* approximation, neglecting viscosity, so that the fluid is described completely by ρ and $\vec{v}$. Moreover, the fact that CDM is pressureless allows for the first term in the r.h.s. of Euler equation to be set to zero. It is possible to split quantities in equations 2.4 into background values and small fluctuations:

$$\begin{aligned}
&\rho(\vec{r}, t) = \bar{\rho}(t) + \delta\rho(\vec{r}, t) = \bar{\rho}(t)\left[1 + \delta(\vec{r}, t)\right] \\
&\vec{v} = \mathcal{H}\vec{x} + \vec{u} \\
&\Phi_{\mathrm{tot}} = \frac{2\pi G}{3}\bar{\rho} r^2 + \Phi(\vec{r}, t)
\end{aligned} \tag{2.5}$$

where δ is the matter overdensity. Moreover, using $\vec{x}$ and τ as spatial and time coordinates, the fluid equations 2.4 become:

$$\begin{aligned}
&\frac{\partial \delta}{\partial \tau} + \vec{\nabla} \cdot [(1 + \delta)\vec{u}] = 0 \\
&\frac{\partial \vec{u}}{\partial \tau} + \mathcal{H}\vec{u} + (\vec{u} \cdot \vec{\nabla})\vec{u} = -\nabla\Phi \\
&\nabla^2 \Phi = 4\pi G \bar{\rho} a^2 \delta\ .
\end{aligned} \tag{2.6}$$

2.1.1 Linear Eulerian Perturbation Theory

Equations 2.6 are fully non linear equations, so the first approach to describe the evolution of δ and $\vec{u}$ is to linearize them. This assumption is accurate only on very large scales, or at large redshifts, where the fluctuation fields are small. It is useful at this point to introduce the velocity divergence $\theta(\vec{x},\tau) = \vec{\nabla}\cdot\vec{u}$. Linearizing the fluid equations gives:

$$\begin{aligned} &\frac{\partial\delta}{\partial\tau} + \theta = 0 \\ &\frac{\partial\theta}{\partial\tau} + \mathcal{H}\theta = -\nabla^2\Phi \\ &\nabla^2\Phi = 4\pi G\bar{\rho}a^2\delta = \frac{3}{2}\mathcal{H}^2\delta \end{aligned} \tag{2.7}$$

where the last equation is exact only for an Einstein-de Sitter universe, but still accurate enough during matter domination. The Poisson equation can then be inserted into the Euler equation, leaving us with just two equations. The continuity and Euler equations can also be rewritten taking their Fourier transform:

$$\begin{aligned} &\frac{\partial\delta_{\vec{k}}}{\partial\tau} = -\theta_{\vec{k}} \\ &\frac{\partial\theta_{\vec{k}}}{\partial\tau} + \mathcal{H}\theta_{\vec{k}} + \frac{3}{2}\mathcal{H}^2\delta_{\vec{k}} = 0 \end{aligned} \tag{2.8}$$

which can be combined to give:

$$\frac{\partial^2\delta_{\vec{k}}}{\partial\tau^2} + \mathcal{H}\frac{\partial\delta_{\vec{k}}}{\partial\tau} - \frac{3}{2}\mathcal{H}^2\delta_{\vec{k}} = 0\ . \tag{2.9}$$

This last differential equation describes the time evolution of the overdensities δ. Factorizing $\delta_{\vec{k}}$ into a time-dependent and scale-dependent part, we may look for a solution of eq. 2.9 of the form $\delta_{\vec{k}}(\tau) = D(\tau)A_{\vec{k}}$, where $D(\tau)$ is called the *growth factor*. In this case, we end up with a second order differential equation for the time-dependent function D:

$$\frac{\partial^2 D}{\partial\tau^2} + \mathcal{H}\frac{\partial D}{\partial\tau} - \frac{3}{2}\mathcal{H}^2 D = 0\ . \tag{2.10}$$

This last equation has two solutions, a growing one and a decaying one:

$$\begin{aligned} &D_+(a) \propto a \\ &D_-(a) \propto a^{-3/2} \end{aligned} \tag{2.11}$$

so that $\delta(\vec{x},\tau) = D_+(\tau)A(\vec{x}) + D_-(\tau)B(\vec{x})$, $A(\vec{x})$ and $B(\vec{x})$ being arbitrary functions that describe the initial density field configuration. Althoug this solution is exact only for an Einstein-de Sitter universe, it is still a good approximation do describe the growth of perturbations during the matter dominated era. Extending this approach to a flat Universe with a cosmological constant yields:

$$D_+(a) = \frac{5}{2}\Omega_{m,0}H(a)\int_0^a \frac{\mathrm{d}a'}{(a')^3 H(a')} \ , \tag{2.12}$$

which must be solved numerically.

2.1.2 Non-linear Eulerian Perturbation Theory

The abovementioned approach can be extended considering the evolution of cosmic fields beyond linear order. This requires a self-consistent approximation, so that the velocity field is completely characterized by its divergence and vorticities are negligible. This is a safe assumption as long as one considers a collisionless fluid with vanishing initial vorticity (single-streaming limit, i.e. the velocity fluid is defined at each point), but breaks down at small enough scales, at the onset of multi-streaming. The perturbative approach involves expanding the density and velocity fields about their linear solutions (that are just time-dependent scalings of the initial fields), so that

$$\delta(\vec{x},\tau) = \sum_{n=1}^{\infty} \delta^{(n)}(\vec{x},\tau) \qquad , \qquad \theta(\vec{x},\tau) = \sum_{n=1}^{\infty} \theta^{(n)}(\vec{x},\tau) \ , \tag{2.13}$$

where $\delta^{(1)} = \delta_L$ is linear in the density field, $\delta^{(2)} \sim (\delta_L)^2$, etc. (the same holds for θ). It is useful at this point to consider only Fourier space quantities, since in linear theory each Fourier mode evolve independently form the others. Considering non-linear contributions to δ and θ, a coupling between different Fourier modes emerges. The equations of motion can be written as:

$$\begin{aligned} &\frac{\partial \delta_{\vec{k}}}{\partial \tau} + \theta_{\vec{k}} = -\int \mathrm{d}^2\vec{k}_1 \mathrm{d}^3\vec{k}_2 \delta_D(\vec{k} - \vec{k}_{12}) \alpha(\vec{k}_1, \vec{k}_2) \theta_{\vec{k}_1} \delta_{\vec{k}_2} \\ &\frac{\partial \theta_{\vec{k}}}{\partial \tau} + \mathcal{H}(\tau)\theta_{\vec{k}} + \frac{3}{2}\Omega_{m,0}\mathcal{H}^2(\tau) = -\int \mathrm{d}^2\vec{k}_1 \mathrm{d}^3\vec{k}_2 \delta_D(\vec{k} - \vec{k}_{12}) \beta(\vec{k}_1, \vec{k}_2) \theta_{\vec{k}_1} \theta_{\vec{k}_2} \ , \end{aligned} \tag{2.14}$$

where δ_D is the Dirac delta, $\vec{k}_{12} = \vec{k}_1 + \vec{k}_2$, a subscript $_{\vec{k}}$ denotes Fourier-space quantities and

$$\alpha(\vec{k}_1, \vec{k}_2) = \frac{\vec{k}_{12} \cdot \vec{k}_1}{k_1^2} \qquad , \qquad \beta(\vec{k}_1, \vec{k}_2) = \frac{k_{12}^2 (\vec{k}_1 \cdot \vec{k}_2)}{2 k_1^2 k_2^2} \tag{2.15}$$

encode the non-linear mode coupling. In an Einstein-de Sitter universe it is possible to write the solutions to eq.s 2.14 as

$$\begin{aligned} \delta^{(n)}_{\vec{k}} &= \int \mathrm{d}^3\vec{q}_1 ... \mathrm{d}^3\vec{q}_n \delta_D(\vec{k} - \vec{q}_{1...n}) F_n(\vec{q}_1, ..., \vec{q}_n) \delta_{L,\vec{q}_1} ... \delta_{L,\vec{q}_n} \\ \theta^{(n)}_{\vec{k}} &= \int \mathrm{d}^3\vec{q}_1 ... \mathrm{d}^3\vec{q}_n \delta_D(\vec{k} - \vec{q}_{1...n}) G_n(\vec{q}_1, ..., \vec{q}_n) \delta_{L,\vec{q}_1} ... \delta_{L,\vec{q}_n} \end{aligned} \tag{2.16}$$

where the kernels F and G can be constructed with recursive relations from the fundamental mode coupling functions of eq. 2.15 (Goroff et al., 1986; Jain & Bertschinger, 1994).

The leading order contribution to the evolution of the power spectrum is obtained from the linear overdensity field δ_L, derived from eq. 2.9:

$$\langle \delta_L(\vec{k}, \tau) \delta_L(\vec{k}', \tau) \rangle = \delta_D(\vec{k} + \vec{k}') P_L(k, \tau) \ , \tag{2.17}$$

where $P_L(k, \tau) = D_+^2(\tau) P_L(k)$, and the linear power spectrum $P_L(k)$ derives from the linear evolution of fluctuations through the radiation dominated era (usually followed using general relativistic Boltzmann solvers). From the higher-order expressions 2.16 for δ and θ, it is possible to compute non-linear corrections to the matter power spectrum: second-order corrections are obtained considering contributions up to third order in δ:

$$P_{\mathrm{NL}}(k, \tau) = P_L(k, \tau) + P_{22}(k, \tau) + P_{13}(k, \tau) \ , \tag{2.18}$$

with

$$\begin{aligned} P_{22}(k, \tau) &= 2 \int \mathrm{d}^2\vec{q} \, F_2^2(\vec{k} - \vec{q}, \vec{q}) \ P_L(|\vec{k} - \vec{q}|, \tau) \ P_L(\vec{q}, \tau) \\ P_{13}(k, \tau) &= 6 P_L(k, \tau) \int \mathrm{d}^3\vec{q} \, F_3(\vec{k}, \vec{q}, \vec{k} - \vec{q}) P_L(\vec{q}, \tau) \ , \end{aligned} \tag{2.19}$$

where F_2 and F_3 are the kernels for $\delta^{(2)}$ and $\delta^{(3)}$. The perturbative approach described above is called Standard Perturbation Theory (SPT), and the correction to the power spectrum of equation 2.18 is commonly referred to as the 1-loop power spectrum, in analogy with particle physics.

The main issue with SPT is that it has poor convergence properties when higher order corrections are included, introducing large deviations from the result of N-body simulations, as shown in Fig. 2.1 (Blas et al., 2014). For this reason, alternative approaches based on different re-summation schemes

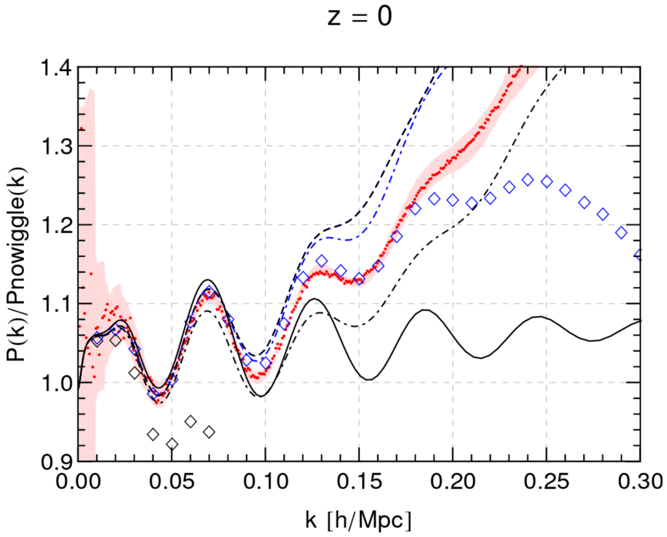

Fig. 2.1: Comparison of matter power spectrum measured from simulations to the SPT results. Solid black line is the linear prediction. Black dashed, dot-dashed lines and diamonds show respectively the one-, two- and three-loop predictions. Blue lines are the result of a re-summation scheme. From Blas et al. (2014)

have been proposed (Crocce & Scoccimarro, 2006; Bernardeau et al., 2008, 2012), as well as approaches based on Effective Field Theory (Baumann et al., 2012; Carrasco et al., 2012, 2014). In general, the SPT approach can predict cosmological quantities such as the power spectrum, showing good agreement with the results of N-body simulations. The validity range of different perturbative schemes was recently tested in Osato et al. (2019), showing that such methods are reliable to get accurate estimations of the cosmological parameters up to scales $k \sim 0.2 - 0.3\ h$ Mpc^{-1}.

2.1.3 Lagrangian Perturbation Theory

One of the assumptions made in §2.1.2 is that DM can be described as a fluid. It is thus possible to look at the evolution of the fluid considering specific locations in space, through which the fluid flows: this allows to study the dynamics of the density and velocity fields, and constitutes the Eulerian approach of SPT. An alternative method is to describe the fluid following the trajectories of particles (fluid elements): this is the Lagrangian description.

In a cosmological context, Lagrangian Perturbation Theory (LPT) was pioneered by Zel'dovich (Zel'dovich, 1970; Shandarin & Zeldovich, 1989). The main idea is to map the initial (Lagrangian) comoving particle position $\vec{q}$ to the final (Eulerian) comoving position $\vec{x}$ by means of a displacement field:

$$\vec{x}(\vec{q},\tau) = \vec{q} + \vec{\Psi}(\vec{q},\tau) \ , \tag{2.20}$$

where the displacement $\vec{\Psi}$ is the main quantity of interest, and the small parameter in the perturbative expansion of LPT. Applying conservation of mass to the fluid element it is possible to derive a relation between the Jacobian of the transformation from Eulerian to Lagrangian coordinates $J(\vec{q},\tau) = \partial\vec{x}/\partial\vec{q}$ and the overdensity δ:

$$\begin{gathered}\rho(\vec{x},\tau)\mathrm{d}^3\vec{x} = \rho(\vec{q})\mathrm{d}^3\vec{q} \quad \rightarrow \quad \bar{\rho}(\tau)[1+\delta(\vec{x},\tau)]\mathrm{d}^3\vec{x} = \bar{\rho}(\tau)\mathrm{d}^3\vec{q} \\ \Rightarrow J(\vec{q},\tau) = \frac{1}{1+\delta(\vec{x},\tau)} \quad \longleftrightarrow \quad \delta(\vec{x},\tau) = J^{-1}(\vec{q},\tau) - 1 \ .\end{gathered} \tag{2.21}$$

The above equation establish a direct relation between the overdensity field δ and the displacement field Ψ.

It is apparent how this result is valid up to orbit crossing: at the first crossing of trajectories, two fluid elements with different initial $\vec{q}$ end up in the same final position $\vec{x}$, the Jacobian J vanishes and the overdensity $\delta \rightarrow \infty$. Shell-crossing is then taken to be the limit of validity of the Lagrangian approach.

The equation of motion is given by Euler equation (2.7), that can be written in Lagrangian coordinates considering that:

- $\vec{u} = \partial\vec{x}/\partial\tau = \partial\vec{\Psi}/\partial\tau$;
- $\delta(\vec{x},\tau) = J^{-1}(\vec{q},\tau) - 1$;
- $(\nabla_{\vec{x}})_i = [\delta_K^{ij} + \vec{\Psi}_{i,j}]^{-1}(\nabla_{\vec{q}})_j$, with δ_K the Kroneker delta and $\vec{\Psi}_{i,j} = \partial\vec{\Psi}_i/\partial\vec{q}_j$.

The resulting equation is then:

$$J(\vec{q},\tau)[\delta_K^{ij} + \vec{\Psi}_{i,j}]^{-1}\nabla_{\vec{q}} \cdot \left[\frac{\partial^2\vec{\Psi}}{\partial\tau^2} + \mathcal{H}(\tau)\frac{\partial\vec{\Psi}}{\partial\tau}\right] = \frac{3}{2}\Omega_m(\tau)\mathcal{H}^2(\tau)[J(\vec{q},\tau) - 1] \ . \tag{2.22}$$

Zel'dovich approximation

The linearized version of eq. 2.22 is the so-called Zel'dovich approximation (ZA, Zel'dovich (1970)). Under the assumption that Ψ is curl-free, it is possible to write the displacement in terms of a potential $\phi = \nabla_{\vec{q}} \cdot \vec{\Psi}$. The resulting equation for the first-order displacement potential is then:

$$\frac{\partial^2 \phi^{(1)}}{\partial \tau^2} + \mathcal{H}(\tau) \frac{\partial \phi^{(1)}}{\partial \tau} = \frac{3}{2} \Omega_m(\tau) \mathcal{H}^2(\tau) \phi^{(1)} \ . \tag{2.23}$$

Since the operator acting on $\phi^{(1)}$ is only a function of time, the time evolution can be factored out and the potential can be written as a (time-dependent) growth factor times the initial potential: $\phi(\vec{q}, \tau) = D_1(\tau)\phi(\vec{q})$, where $D_1(\tau)$ is the linear growth factor already derived for SPT. At linear order, the density can be written as:

$$\delta(\vec{x}, \tau) + 1 = \frac{1}{[1 - \lambda_1 D_1(\tau)][1 - \lambda_2 D_1(\tau)][1 - \lambda_3 D_1(\tau)]} \ , \tag{2.24}$$

where λ_i are the eigenvalues of the Hessian of the potential $H = \partial^2 \phi / \partial q_i \partial q_j$. This equation allows for a simple interpretation of shell-crossing in ZA, depending on the value of the eigenvalues λ_i:

- $\lambda_i < 0$: we are looking at an underdense region that will reach $\delta = -1$;
- $\lambda_3 > 0$, $\lambda_1, \lambda_2 < 0$: when $\lambda_3 D_1(\tau) \to 1$ we have planar collapse along the axis identified by λ_3, leading to the formation of a bidimensional “cosmic pancake”;
- $\lambda_2, \lambda_3 > 0$, $\lambda_1 < 0$: tha collapse happens in two dimensions, leading to the formation of a filament;
- $\lambda_1, \lambda_2, \lambda_3 > 0$: the collapse proceeds in all directions. $\lambda_1 = \lambda_2 = \lambda_3$ corresponds to the collapse of a sphere.

Higher-order Lagrangian Perturbation Theory

Considering higher-order terms in eq. 2.22 leads to significant improvements in the description of the non-linear evolution of overdensities respect to the ZA. This is due to the fact that higher-order LPT takes into account the effects of gravitational tidal fields, i.e. the non-locality of the gravitational instability.

The perturbative expansion is expressed in terms of the displacement field as:

$$\vec{\Psi}(\vec{q},\tau) = \sum_i \vec{\Psi}^{(i)}(\vec{q},\tau) \ , \tag{2.25}$$

where the first order is related to the linear overdensity $\nabla_{\vec{q}} \cdot \vec{\Psi}^{(1)} = D_1(\tau)\delta(\vec{q})$ and $\vec{\Psi}^{(2)} \propto (\vec{\Psi}^{(1)})^2$ etc. Keeping second order terms in eq. 2.22, and writing the displacement field in terms of the potential ϕ one obtains:

$$\left(\frac{\partial^2}{\partial\tau^2} + \mathcal{H}\frac{\partial}{\partial\tau} - \frac{3}{2}\mathcal{H}^2\Omega_m\right)\phi^{(2)}_{,ii} = -\frac{3}{2}\mathcal{H}^2\Omega_m\left[\frac{1}{2}\left(\phi^{(1)}_{,ii}\phi^{(1)}_{jj} - \phi^{(1)}_{,ij}\phi^{(1)}_{,ji}\right)\right] \ , \tag{2.26}$$

where $_{,ij} = \partial^2/\partial q_i \partial q_j$. Again, it is possible to factorize the second order potential in a time- and space-dependent part, so that the time evolution is encoded in a second order growth factor $D_2(\tau)$, that can be obtained solving the differential equation

$$\left(\frac{\partial^2}{\partial\tau^2} + \mathcal{H}\frac{\partial}{\partial\tau} - \frac{3}{2}\mathcal{H}^2\Omega_m\right)D_2(\tau) = -\frac{3}{2}\mathcal{H}^2\Omega_m D_1^2(\tau) \ . \tag{2.27}$$

The initial second-order displacement potential $\phi^{(2)}(\vec{q},\tau_{in})$ is the term in square brackets on the right-hand-side of eq. 2.26. Extensions of LPT up to third order (3LPT) were developed in Buchert (1992); Buchert & Ehlers (1993); Buchert (1994), showing significant improvements in the description of mildly-NL scales. Fig. 2.2 shows the comparison between density maps obtained from a full N-body simulation (top left), and increasing LPT orders (first-, second- and third-order, clockwise from the top right panel): the clear effect is a thickening of the NL structures for higher LPT orders. A more quantitative way to measure the performance of the Lagrangian approach is obtained comparing the statistics of the cosmic field. In Munari et al. (2017a), the authors show the effect of higher perturbative orders on the predictions for the matter power spectrum. The bottom panel of Fig. 2.3 shows the ratio of the power spectrum with respect to the one measured from N-body simulations, highlighting the significant improvement of 3LPT over the ZA and 2LPT.

Given an initial displacement field and once the equations for the growth factors are solved, the advantage of LPT is the straightforward computation of potentials and displacements for any time. For this reason, LPT has proven to be a very powerful tool and is indeed the foundation on which many

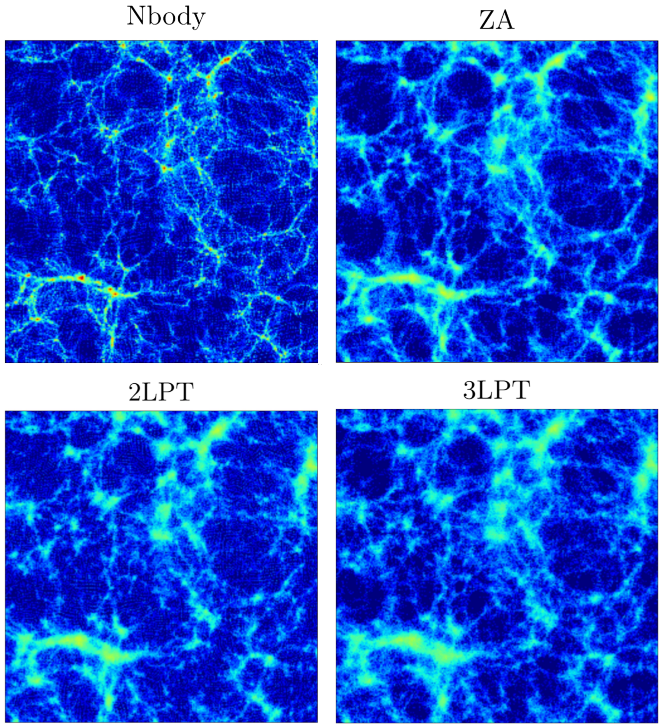

Fig. 2.2: Density maps at $z = 0$ obtained for a full N-body simluation (top left) and different orders of LPT (Munari et al., 2017a). The panels show slices of depth 10 h^{-1} Mpc and side 200 h^{-1} Mpc.

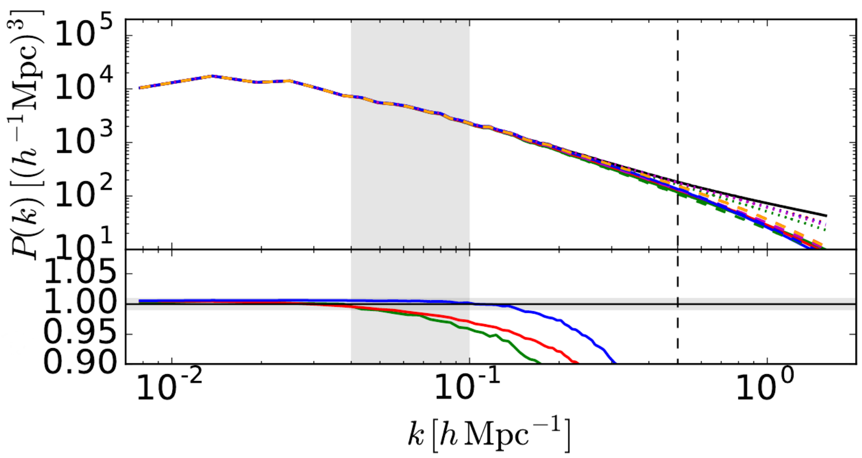

Fig. 2.3: Matter power spectrum at $z = 1$ obtained from N-body simulations (black solid line) and LPT displacements. The green line is the ZA, red line is 2LPT and blue line is 3LPT. From Munari et al. (2017a).

approximate methods (§2.2.2) rely.

2.2 Simulating the Universe

As mentioned before, the proper tool to get a full description of the non-linear scales of the LSS and their evolution are N-body simulations. During the last decades, technological advances allowed to access a larger and larger number of cores, as well as large storage facilities, resulting in an improvement of cosmological N-body simulations both in size and resolution.

However, full N-body remain computationally expensive. On the other hand, a proper computation of covariance matrices (essential to constrain cosmological parameters, see §1.3.2) calls for the generation of large sets of realizations. It has been shown that, in order to reach the precision needed by future experiments, $\sim 10^3$ realizations are needed. Such a problem cannot be tackled with N-body simulations, however it can be solved with the use of approximate methods. The latter are the optimal tradeoff between speed and accuracy, being able to readily generate the large sets of simulated catalogs needed while following the mildly NL scales with sufficient precision.

2.2.1 N-body simulations

Cosmological N-body simulations involve generating a realization of the Universe in a finite comoving volume with a cubic box of side L^3_{box}. The continuous DM distribution is sampled at some discrete locations in phase-space (grid points), that act as particles in the simulation. The mass resolution of the simulation depends then on the number of particles N_{part}:

$$m_p = \bar{\rho}\frac{L^3_{\text{box}}}{N_{\text{part}}} \, , \tag{2.28}$$

where $\bar{\rho}$ is the homogeneous density fixed by the fiducial cosmology. In the case of cosmological simulations, N-body particles do not correspond to real particles but rather to mass elements m_p, with position $\vec{x}_i$ and velocity $\vec{v}_i$; this naturally leads to the introduction of a *softening length*, to deal with the (unphysical) scattering of particles that get close together.

Initial conditions (particles velocities and positions) for the simulations are generated displacing particles from a regular grid with LPT displacements; this is done at a sufficiently high redshift, so that the perturbative approach can be safely adopted ($50 \leq z \leq 100$). The N-body code then proceeds to numerically solve the equations of motion for particles that interact gravitationally. The underlying dynamics is, in general cases, approximated by Newton law, but it can also include relativistic effects or modified gravity. The equations of motion for the particles are then

$$\frac{\mathrm{d}\vec{x}_i}{\mathrm{d}t} = \vec{v}_i \quad , \quad m_p \frac{\mathrm{d}\vec{v}_i}{\mathrm{d}t} = \vec{F}_i \ , \tag{2.29}$$

where $\vec{F}_i$ is the force acting on the particle i due to interaction with all other particles j:

$$\vec{F}_i = -\sum_{j \neq i} G m_i m_j \frac{(\vec{r}_i - \vec{r}_j)}{|\vec{r}_i - \vec{r}_j|^3} \ . \tag{2.30}$$

The evaluation of the force of eq. 2.30 is the most time consuming task in an N-body simulation, due to the large number of particles usually involved ($N_{\rm part} \sim 10^9 - 10^{10}$, and the number of interactions to be computed scales as $\mathcal{O}(N^2)$). For this reason, methods that evaluate the force acting on each particle as the sum of the contributions of all other $N-1$ particles (*particle-particle methods*) are computationally expensive, and different approximation schemes have been developed to reduce computational time in collisionless systems. Two commonly adopted approaches are:

- *Particle-mesh methods* (PM, Hockney & Eastwood (1988)): the density field is discretised over a grid (mesh). The gravitational potential is then evaluated solving the Poisson equation (sourced by the discrete density field) in Fourier space, by means of Fast Fourier Transforms. The downside of this method is that the mesh size limits the resolution, introducing errors on the evaluated forces on small scales. To mitigate this issue, the mesh can be adaptive (*Adaptive Mesh Refinement*, AMR) rather than static, so that more dense regions are sampled with a finer mesh. The computational cost of particle-mesh methods scales as $\mathcal{O}(N_g \log N_g)$, N_g being the number of vertices of the mesh;

- *Tree methods* (Barnes & Hut, 1986): the number of interactions to be evaluated is reduced dividing the volume into cubic cells by means of an octree; for nearby cells, the interactions between particles are evaluated individually, while distant cells are treated as single particles. In this case, the computational cost scales as $\mathcal{O}(N \log N)$.

Currently available code for N-body simulations include RAMSES (PM + AMR, Teyssier (2002)), PKDGRAV (tree algorithm, Stadel (2001)) and GAD-

GET (hybrid tree-PM, (Springel, 2005)). A recent code comparison was performed in Schneider et al. (2016) by the Euclid Cosmological Simulation Working Group, later extended in Garrison et al. (2019) including the ABACUS code (Garrison et al. (2018)). Despite the different algorithm choice, both the power spectra and bispectra obtained from different codes showed percent agreement, ensuring that at least numerical effects are under control.

2.2.2 Approximate methods

Future surveys, such as the Euclid satellite described in §1.5, will observe billions of galaxies, making the error budget dominated by systematics rather than statistical errors. Simulating wide modern surveys is still a challenge, despite the tremendous improvement of N-body codes. The reason behind this are the large volumes ($L \sim 4h^{-1}\mathrm{Gpc}$, needed to properly sample the BAO scale and generate past-light-cones without many replications along the l.o.s.) and high resolution (resolve halos of at least $\sim 10^{11} M_\odot$, which translates in $m_p \leq 10^9 M_\odot$, or $N_\mathrm{part} \sim 10^{12}$) are required. Currently the largest available N-body simulation is the Euclid Flagship Simulation, with a box of $L = 3780h^{-1}\mathrm{Mpc}$ and $N_\mathrm{part} = 2 \times 10^{12}$ particles. Such a simulation is already expensive in term of computational time and storage, but on top of that, a precise determination of the cosmological parameters from survey data requires a proper modeling of the covariance matrix, in order to evaluate the likelihood. To that end, thousands of simulated catalogs are required for each cosmological model to constrain. The proper tool to address this problem are approximate methods: semi-analytical models that rely on some approximation to make them run significantly faster than full N-body (a factor of ~ 1000), with minor compromises on the accuracy of the modeling of mildly-NL scales (there is a significant loss of accuracy at scales $\gtrsim 0.5h\mathrm{Mpc}^{-1}$).

During the 1990s approximate methods drew interest (and effort in the development) as an alternative to N-body simulations (Sahni & Coles, 1995). In recent years, they are being used as a complement to full N-body, rather than an alternative, with the purpose of evaluating covariance matrices. Approximate methods can roughly be divided into two categories:

- *Predictive methods* that follow the particle trajectories, evolving some initial linear density field down to the halo formation;

- *Calibrated methods* that use some bias scheme to stochastically populate a non-linear density field with halos. They are usually faster than predictive models, but need to be calibrated on a reference N-body simulation.

Codes that implement predictive approximate methods are PINOCCHIO (Monaco et al., 2002a, 2013), PTHALOS (Scoccimarro & Sheth, 2002), together with methods that implement a particle-mesh scheme such as COLA (Tassev et al., 2013) and FASTPM Feng et al. (2016). Hybrid-PM schemes show an improved accuracy in describing NL scales with respect to purely Lagrangian methods, but at the price of larger computational time. Codes like PATCHY (Kitaura et al., 2014), EZMOCKS (Chuang et al., 2015a) and HALOGEN (Avila et al., 2015) fall instead in the second category of calibrated methods.

A comparison of the clustering statistics obtained using approximate methods was performed in Chuang et al. (2015b), quantifying deviations from N-body simulations in the two- and three-point statistics both in real and redshift space, as well as the mass function. More recently, a series of paper focused on the performances of different approximate methods to compute the covariance matrix for the two-point correlation function (Lippich et al., 2019), power spectrum (Blot et al., 2019) and bispectrum (Colavincenzo et al., 2019), as compared to the covariance obtained from a set of N-body simulations. Those works showed that all approximate methods can accurately recover the mean parameter values inferred using the N-body covariance. Moreover, the parameter uncertainties agree with the corresponding N-body results within 10%. These results confirm that, given their speed with respect to full N-body simulations, approximate methods are the optimal tool to compute covariances.

This PhD work is focused on extending the PINOCCHIO code to modified gravity theories, therefore the code is described in more detail in chapter 4.

2.3 Gravitational collapse

According to the standard cosmological model, structure formation in the Universe is driven by gravitational collapse of regions that are overdense with respect to the background. Such overdensities initially expands with the Hubble flow, until they reach a maximum size (*turnaround*, TA) and then start collapsing, finally forming virialized objects. Baryonic matter, in the form of gas, feels the gravitational pull of such DM halos: it is accreted onto the halo, shocked, and eventually cools down and start forming stars and galaxies. The simplest way to describe the gravitational collapse of perturbation is provided by the spherical collapse model (Gunn, 1977), that can be extended considering more realistic triaxial shapes for halos, as in the ellipsoidal collapse model (White & Silk, 1979; Bond & Myers, 1996).

2.3.1 Spherical collapse

The most straightforward way to describe the collapse of perturbations is treating them as spherical overdensities δ embedded in an expanding Universe. The evolution of a shell of radius r is described by Newton equation:

$$\frac{\mathrm{d}^2 r}{\mathrm{d}t^2} = -\frac{GM}{r^2} \, , \tag{2.31}$$

where $M = M(< r)$ is the mass enclosed within the shell. The assumption of the model is that there is no shell-crossing, so that both the total mass and the mass of each shell remain constant. Eq. 2.31 can be integrated once to get

$$\frac{1}{2}\left(\frac{\mathrm{d}r}{\mathrm{d}t}\right)^2 - \frac{GM}{r} = E \, . \tag{2.32}$$

For $E = 0$, the solution is $r \propto M^{1/3} t^{2/3}$: the overdensity expands as an Einstein-de Sitter universe, with scale factor $a(t) \propto t^{2/3}$. However, if $E < 0$, the derivative $\mathrm{d}r/\mathrm{d}r$ can change sign: in this case, the expansion slows down until it reaches the TA point, after which collapse starts. This happens when the region considered is sufficiently denser with respect to the environment, and the gravitational pull is enough to win over the kinetic energy. The time evolution of the shell can also be written in terms of a parametric solution of the form:

$$\begin{aligned} r &= A r_{in}(1 - \cos\theta) \\ t &= B t_{in}(\theta - \sin\theta) \, . \end{aligned} \tag{2.33}$$

where r_{in} is the initial radius of the overdensity. The turnaround moment corresponds to $\theta = \pi$, while collapse occurs for $\theta = 2\pi$.

The initial conditions for eq. 2.31 are set by the initial overdensity δ_{in}:

$$M = \frac{4\pi}{3} r^3(t)\rho(t) = M_{in} = \frac{4\pi}{3} r_{in}^3 \bar{\rho}_b (1 + \delta_{in}) \ , \tag{2.34}$$

where $\bar{\rho}_b$ is the background density. The second initial condition is set so that the initial velocity of the shell matches the expansion of the Universe, $(\mathrm{d}r/\mathrm{d}t)_{in} = H_{in} r_{in}$. The initial energy of the shell is then:

$$\begin{cases} K_{in} = \frac{1}{2}\left(\frac{\mathrm{d}r}{\mathrm{d}t}\right)^2 |_{in} = \frac{H_{in}^2 r_{in}^2}{2} \\ U_{in} = -GM_{in}/r_{in} = -H_{in}^2 r_{in}^2 \Omega_m (1+\delta_{in})/2 = -K_{in}\Omega_m(1+\delta_{in}) \end{cases} \tag{2.35}$$

with K and U being the kinetic and gravitational potential energy respectively, and Ω_m the matter density parameter. Equation 2.35 allows to set a first condition for collapse:

$$\begin{aligned} E_{in} = K_{in} + U_{in} = K_{in}(1 - \Omega_m(1+\delta_{in})) < 0 \\ \Rightarrow (1+\delta_{in}) > \Omega_m^{-1} \ . \end{aligned} \tag{2.36}$$

The moment of TA corresponds to the moment of maximum expansion, when the kinetic energy is zero and the total energy of the shell is given by the gravitational potential energy $E = -\frac{GM}{r_{TA}}$; after this moment, the overdensity begins to shrink, until it collapses and reaches virial equilibrium. It is possible to derive a relation between the radius of maximum expansion r_{TA} and the virial radius r_{vir}: just considering energy conservation and the virial theorem $(U_{vir} = -2K_{vir})$ one can derive $r_{vir} \sim \frac{r_{TA}}{2}$, meaning that at virialization the system is half the size with respect to TA. This last relation can be used to set A and B in eq. 2.33, and then derive the evolution equation for the overdensity δ. For an Einstein-de Sitter universe and in the linear regime, the latter can be written as:

$$\delta \simeq \frac{3}{20}\theta^2 \simeq \frac{3}{5}\delta_{in}\left(\frac{t}{t_{in}}\right)^{2/3} \ , \tag{2.37}$$

so that the linearly extrapolated values are $\delta_L \simeq 1.062$ at TA and $\delta_L \simeq 1.686$ at virialization. It can be shown that the density at collapse does not change much if one includes a cosmological constant Λ: in that case, $\delta_L \simeq 1.696\Omega_m(a_{coll})^{0.0055}$, with a very weak dependence on the cosmology.

2.3.2 The halo mass function

The dynamical description of the evolution of perturbations deep in the non-linear regime is quite complicated. However, several methods have been developed to predict the distribution and masses of collapsed objects starting from an initial density field $\delta(\vec{x}, t_{in})$.

The main idea behind these approaches is that objects of mass M form from overdense regions in an initial density field $\delta(\vec{x}; R)$ smoothed on some scale R; it is somewhat natural to think that such regions correspond to peaks in the density field. Identifying the number density of peaks with the number density of objects of mass $M \propto R^3$ leads however to the so-called *cloud-in-cloud* problem: a mass element associated to a peak $\delta(\vec{x}; R_1)$ could also be associated to $\delta(\vec{x}; R_2)$ with $R_2 > R_1$. There are two possibilities:

- $\delta_2 < \delta_1$: the mass element reaches the critical density for collapse first at t_1 on scale R_1 (forming an object of M_1), then at $t_2 > t_1$ on scale R_2 (forming an object of mass M_2). Hence, the mass element is part both of M_1 and M_2, reflecting a situation where an object of mass M_1 merges to form a larger halo of mass M_2 at t_2;
- $\delta_2 > \delta_1$: the mass element should end up directly in the object of mass M_2, without being part of the object of mass M_1. The peak δ_1 should then be excluded from the number density of objects of mass M_1, and considered in the number density of halos with mass M_2.

Predicting the halo mass function, i.e. the number densities of halos with mass between M and $M + \mathrm{d}M$, requires a proper way to split the density field into separate "patches". It is possible to tackle the problem in a statistical way, in order to characterize the halo population. The basic assumptions behind this approach are:

- the initial density field is a Gaussian random field;
- densities are computed extrapolating the linear densities into the non-linear regime;
- the density is smoothed on some scale $R \propto M^{1/3}$;
- mass elements at some location $\vec{x}$ end up in halos of mass M at a time t if their density is above some threshold $\delta_c(t)$;

A simple method is the so-called Press-Schechter formalism (PS, Press & Schechter (1974)): the spherical collapse model can be used to set the threshold for collapse at $\delta_c = 1.686$. The assumption of the model is that the fraction of halos with mass $> M$ is given by the probability that the density contrast (smoothed on scale R) is larger than δ_c:

$$\mathcal{P}(>\delta_c) = \int_{\delta_c}^{\infty} \frac{1}{\sqrt{2\pi}\sigma(R)} \exp\left(-\frac{\delta^2}{2\sigma^2(R)}\right) d\delta \,. \qquad (2.38)$$

with $\sigma^2(R) = \langle\delta^2\rangle$ the variance of the smoothed density field. The shortcoming of this approach is that, as $M \to 0$, $\sigma(M) \to \infty$ and $\mathcal{P}(>\delta_c) \to 1/2$: only half of the mass is in collapsed objects; this is a consequence of the linear approximation. The problem was circumvented with the introduction of a "fudge factor" 2. The PS halo mass function can be derived differentiating eq. 2.38:

$$n(M,t)\mathrm{d}M = \sqrt{\frac{2}{\pi}} \frac{\bar{\rho}}{M^2} \frac{\delta_c}{\sigma} \exp\left(-\frac{\delta_c}{2\sigma^2}\right) \left|\frac{\mathrm{d}\ln\sigma}{\mathrm{d}\ln M}\right| \mathrm{d}M \qquad (2.39)$$

An alternative mass function was derived in Bond et al. (1991); Bower (1991); Peacock & Heavens (1990); Lacey & Cole (1993) (Extended Press-Schechter formalism, EPS), based on the *excursion set formalism*. The EPS approach was further extended with the inclusion of a "moving" barrier in place of the fixed critical density for collapse at δ_c (Sheth & Tormen, 1999, 2002). The latter is based also on ellipsoidal collapse, which is the topic of §2.3.3. All this approaches are more phenomenological than physical, thus they are not guaranteed to provide an accurate description of the formation of DM halos.

2.3.3 Ellipsoidal collapse

A more sophisticated description of the evolution of structures in the Universe can be obtained by relaxing the assumption of spherical symmetry for the shape of overdensities, for instance employing a triaxial treatment. This can be done describing the overdensities as homogeneous ellipsoids embedded in a background Universe, as in the *ellipsoidal collapse model* (EC, first considered in White & Silk 1979, and further developed in Bond & Myers 1996). EC was also adopted in Sheth & Tormen (1999, 2002) and Monaco

(1997a,b), to compute predictions for the halo mass function in the framework of the excursion set approach. The triaxial description of overdensities introduces the problem of finding a proper definition for the time of collapse. In general, there are two possibilities:

- collapse of the ellipsoid on the third axis: this definition is appropriate to describe the collapse of peaks, intended as extended regions, and was adopted in Bond & Myers (1996),Sheth & Tormen (2002). In this case, the tidal tensor and the inertia tensor are misaligned, leading to the acquisition of angular momentum (White, 1984);
- collapse of the ellipsoid on the first (shortest) axis, corresponding to the moment of orbit crossing: this definition is suitable to describe the collapse of mass elements, and was adopted in Monaco (1997a,b). In this case the tidal tensor and the inertia tensor are aligned, and there is no acquisition of angular momentum. The overdensity starts evolving as a sphere, but acquires a triaxial shape due the presence of tidal forces.

In this section I describe three different prescriptions for the evolution of ellipsoidal overdensities that can be employed to compute the collapse times of ellipsoids: the one described in Bond & Myers (1996), later reformulated in Nadkarni-Ghosh & Singhal (2016), and a description based on LPT (Monaco, 1997a).

Bond & Myers approach

The density contrast δ of an ellipsoid with density ρ_e embedded in a background with density ρ_b is given by:

$$\delta = \frac{\rho_e}{\rho_b} - 1 \ . \tag{2.40}$$

The three principal axes of the ellipsoid can be written as $r_i(t) = a_i(t)\,q$, where q is the comoving radius of the corresponding Lagrangian sphere (concentric with the ellipsoid and with the same mass, but with density equal to the background), while $a_i(t)$ represents the time evolution of the ellipsoid axes. Enforcing mass conservation leads to:

$$a^3 q^3 \rho_m = a_1 a_2 a_3 q^3 \rho_e \ , \tag{2.41}$$

so that

$$\delta = \frac{a^3}{a_1 a_2 a_3} - 1 \; . \tag{2.42}$$

The evolution equation for the ellipsoid principal axes can be written as (Bond & Myers, 1996):

$$\frac{\mathrm{d}^2 a_i}{\mathrm{d}t^2} = \frac{8\pi G}{3}\rho_\Lambda a_i - 4\pi G\bar{\rho}_m a_i \left[\frac{1}{3} + \left(\frac{\delta}{3} + \frac{\delta b_i}{2} + \lambda_{ext,i}\right)\right] \; . \tag{2.43}$$

The term in round brackets in eq. 2.43 represents the contribution from the gravitational potential of the ellipsoid. In particular, the parameters b_i and $\lambda_{ext,i}$ denote the internal and external contributions to the tidal shear. The total tidal field is described by the tidal field tensor $T_{ij} = \partial^2\Phi_P/\partial x_i \partial x_j = T_{ij,\mathrm{int}} + T_{ij,\mathrm{ext}}$, with Φ_P the peculiar gravitational potential. The ellipsoid's eigensystem is the same as the eigensystem of T, so the internal shear can be evaluated as:

$$b_i(t) = a_1(t)a_2(t)a_3(t) \int_0^\infty \frac{\mathrm{d}\tau}{[a_i^2(t)+\tau]\prod_{j=1}^3 (a_j^2(t)+\tau)^{1/2}} - \frac{2}{3} \; . \tag{2.44}$$

On the other hand, the external shear can be evaluated as:

$$\begin{cases} \lambda_{ext,i}(t) = \frac{D_1(t)}{D_1(t_0)}\left(\lambda_i(t_0) - \frac{\delta(t_0)}{3}\right) & \text{linear} \\ \lambda_{ext,i}(t) = 5b_i(t)/4 & \text{non linear} \end{cases} \tag{2.45}$$

where D_1 is the linear growth factor, t_0 is some initial time and the λ_i terms are the eigenvalues of the tidal tensor. The effects of the linear or non-linear approximation in evaluating the external shear have been studied in Angrick & Bartelmann (2010), where the authors introduced a hybrid model to interpolate between the two. The equation of motion 2.43 can be written using the expansion rate of the background a as time variable:

$$\frac{\mathrm{d}^2 a_i}{\mathrm{d}a^2} + \left(\frac{1}{a} + \frac{E'(a)}{E(a)}\right)\frac{\mathrm{d}a_i}{\mathrm{d}a} + \left(\frac{3\Omega_{m,0}\, C_i(a)}{2a^5 E^2(a)} - \frac{\Omega_\Lambda}{a^2 E^2(a)}\right) a_i = 0 \; , \tag{2.46}$$

where $E(a) = H(a)/H_0$ is the dimensionless Hubble rate, and $C_i(a)$ is the term in square brackets in eq. 2.43. The initial conditions for this differential

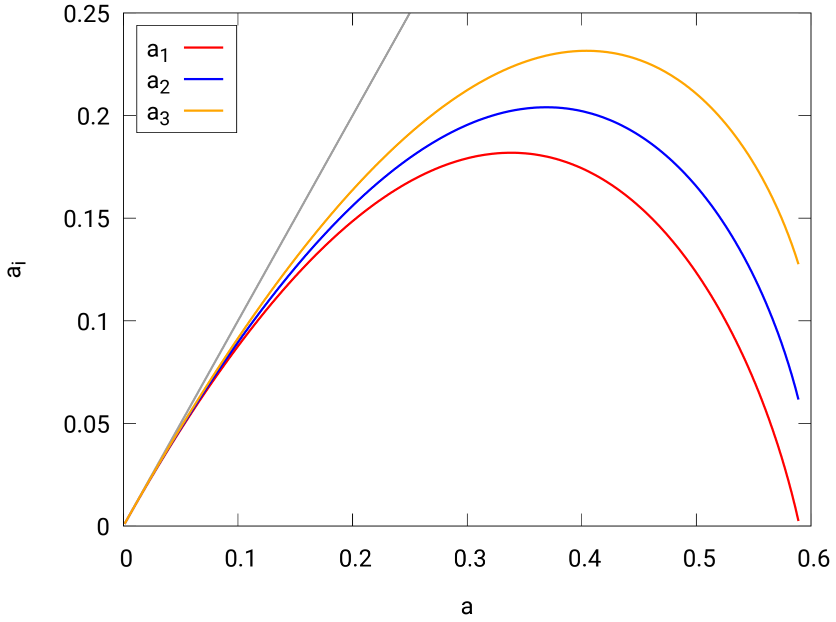

Fig. 2.4: Evolution of the axes of an ellipsoid with $\lambda_1 = 1.2$, $\lambda_2 = 1$, $\lambda_3 = 0.8$ corresponding to a linearly evolved $\delta(a_0) = 3$, computed numerically integrating eq. 2.43: the three axes evolve together at the beginning, with the expanding Universe, but the evolution proceeds at different rates in the three directions, with a_1 (axis with the largest λ) reaching turnaroud well before the other ones. The integration is stopped as the first axis collapses $(a_1 = 0)$.

equation are set by the Zel'dovich approximation:

$$\begin{cases} a_i(a_0) = a_0[1 - \lambda_i(a_0)] \\ a_i^{'}(a_0) = 1 - \lambda_i(a_0) - \frac{\mathrm{d}\ln D_1}{\mathrm{d}\ln a}|_{a=a_0} \approx 1 - 2\lambda_i(a_0) \end{cases} \tag{2.47}$$

Eq. 2.43 defines a set of three coupled second-order integro-differential equations describing the evolution of the ellipsoidal overdensity. The moment of collapse is defined as the moment of first axis collapse: assuming $\lambda_1 \geq \lambda_2 \geq \lambda_3$, collapse corresponds to $a_1 = 0$. The evolution equations for the ellipsoid can be solved numerically for a given set of eigenvalues λ_i of the deformation tensor (e.g. Fig. 2.4). However, the evaluation of the elliptic integral of eq. 2.45 is computationally demanding, making it unsuitable for a fast evaluation of collapse times for a large number of objects.

Nadkarni-Ghosh & Singhal approach

An alternative approach to ellipsoidal collapse is described in Nadkarni-Ghosh & Singhal (2016). This is just a reformulation of the BM approach in terms of the eigenvalues of the deformation tensor, the velocity derivative tensor and the gravity Hessian. The ellipsoid's evolution is described by a set of nine dimensionless parameters:

$$\begin{aligned} \lambda_{a,i} &= 1 - \frac{a_i}{a} \\ \lambda_{v,i} &= \frac{1}{H}\frac{\dot{a}_i}{a_i} - 1 \\ \lambda_{d,i} &= \frac{\delta\alpha_i}{2} + \lambda_{ext,i} = C_i - \frac{1}{3} \end{aligned} \tag{2.48}$$

where C_i is again the term in square brackets in eq. 2.43. The eigenvalues $\lambda_{d,i}$ are ordered as $\lambda_{d,1} \geq \lambda_{d,2} \geq \lambda_{d,3}$, so that $\lambda_{v,1} \leq \lambda_{v,2} \leq \lambda_{v,3}$ and $\lambda_{a,1} \geq \lambda_{a,2} \geq \lambda_{a,3}$. The new parameters of eq. 2.48 correspond to:

- The three λ_a correspond to the eigenvalues of the deformation tensor and characterize the shape of the ellipsoid; when an axis is collapsing, $\lambda_a \to 1$;
- The three λ_v capture the deviation of the velocity of each axis expansion with respect to the Hubble flow;
- The three λ_d correspond to the eigenvalues of the gravity Hessian (tensor of second derivatives of the gravitational field), i.e. $\delta = \sum \lambda_{d,i}$.

The evolution equations for the nine eigenvalues are:

$$\begin{aligned} \frac{\mathrm{d}\lambda_{a,i}}{\mathrm{d}\ln a} &= -\lambda_{v,i}(1-\lambda_{a,i}) \\ \frac{\mathrm{d}\lambda_{v,i}}{\mathrm{d}\ln a} &= -\frac{1}{2}\left[3\Omega_m(a)\lambda_{d,i} - \left(\Omega_m(a) - 2\Omega_\Lambda(a) - 2\right)\lambda_{v,i} + 2\lambda_{v,i}^2\right] \\ \frac{\mathrm{d}\lambda_{d,i}}{\mathrm{d}\ln a} &= -(1+\delta)\left(\delta + \frac{5}{2}\right)^{-1}\left(\lambda_{d,i} + \frac{5}{6}\right)\sum_{j=1}^{3}\lambda_{v,j} + \\ &\quad + \left(\lambda_{d,i} + \frac{5}{6}\right)\sum_{i=1}^{3}(1+\lambda_{v,i}) - \left(\delta + \frac{5}{2}\right)(1+\lambda_{v,i}) + \\ &\quad + \sum_{j\neq i}\frac{(\lambda_{d,j} - \lambda_{d,i}[(1-\lambda_{a,i})^2(1+\lambda_{v,i}) - (1-\lambda_{a,j})^2(1+\lambda_{v,j})]}{(1-\lambda_{a,i})^2 - (1-\lambda_{a,j})^2} \end{aligned} \tag{2.49}$$

These are obtained taking the derivative of eq. 2.48 with respect to the scale factor a. The collapse times computed solving 2.49 are the same as those derived from the BM approach, with the added bonus of avoiding the introduction of elliptic integrals, making the numerical solution of equations 2.49 faster. A comparison between collapse times for different ellipsoidal configurations can be found in §6.1.

Lagrangian PT approach

A third possibility to describe the evolution of ellipsoidal density perturbations is described in (Monaco, 1997a). The main idea is to expand the peculiar potential φ in a Taylor series:

$$\varphi(\vec{q}) = \varphi(\vec{q}_0) + \frac{\partial \varphi}{\partial q_i}(\vec{q}_0) q_i + \frac{1}{2}\frac{\partial^2 \varphi}{\partial q_i \partial q_j} q_i q_j + ... \tag{2.50}$$

The first term is a constant, while the second term produces a bulk motion of the mass element. The third term in eq. 2.50 is the first occurring term in the expansion to determine the density evolution of the mass element. It is a quadratic potential (determined by the Hessian of the gravitational potential), and is the same as the case of an homogeneous ellipsoid and can be used to model the evolution of the overdensity. As shown in Monaco (1997a), the application of LPT up to third order provides a good approximation to the evolution of the ellipsoid. Considering a quadratic potential:

$$\varphi(\mathbf{q}) = \frac{1}{2}(\lambda_1 q_1^2 + \lambda_2 q_2^2 + \lambda_3 q_3^2) \tag{2.51}$$

Collapse is identified as the moment the density diverges, corresponding to vanishing of the Jacobian. This amounts to choosing the moment of orbit crossing as the time when $J(\mathbf{q}, t) = 0$:

$$1 + \varphi_{,11} D_1 + \varphi^{(2)}_{,11} D_2 + \varphi^{(3a)}_{,11} D_{3a} + \varphi^{(3b)}_{,11} D_{3b} = 0 \ , \tag{2.52}$$

where D_i are the growth factors for the different LPT orders. In the ellipsoid's eigensystem the contribution to the deformation tensor are diagonal:

$$\begin{aligned}
\varphi_{,11} &= \lambda_1 \\
\varphi^{(2)}_{,11} &= \lambda_1(\lambda_2+\lambda_3) \\
\varphi^{(3a)}_{,11} &= \lambda_1\lambda_2\lambda_3 \\
\varphi^{(3b)}_{,11} &= \lambda_1\lambda_2\lambda_3 + \frac{\lambda_1\delta_l(\delta_l-\lambda_1)}{2}
\end{aligned} \tag{2.53}$$

The D_2, D_{3a} and D_{3b} growth factors can be written as functions of the linear growth factors D_1 (with a weak dependence on the matter density parameter, as shown in Bouchet et al. (1995)). Eq. 2.52 then becomes:

$$\begin{aligned}
&\left[\frac{\mu}{9}\Omega_m(a)^{-4/275} - \frac{5}{42}\Omega_m(a)^{-268/17875}\left(\mu + \frac{\lambda_1\delta(\delta-\lambda_1)}{2}\right)\right] D_1^3(a) \\
&\quad -\frac{3}{14}\Omega_m(a)^{-1/143}\lambda_1(\delta-\lambda_1)D_1^2(a) - \lambda_1 D_1(a) + 1 = 0 \ ,
\end{aligned} \tag{2.54}$$

where $\mu = \lambda_1\lambda_2\lambda_3$. Eq. 2.54 can be solved analitically if one neglects the dependence on $\Omega_m(a)$, adopting the linear growth rate as time coordinate.

A comparison of collapse times computed with LPT and BM was performed in Monaco (1995), showing good agreement except for the quasi-spherical case, were the LPT approach significantly overestimates collapse times. This issue is due to the slow convergence of the LPT truncation for spherical configurations, however it can be solved with the introduction of a correction allowing to recover spherical collapse:

$$D^C_{n,\mathrm{coll}} = D_{n,\mathrm{coll}} - \Delta \exp(-ax-by) \ , \tag{2.55}$$

where $x = \lambda_1 - \lambda_2$, $y = \lambda_2 - \lambda_3$ and

$$\begin{cases}
n=2 \quad , \quad \Delta = 0.580 \quad , \quad a = 5.4 \quad , \quad b = 2.3 \ , \\
n=3 \quad , \quad \Delta = 0.364 \quad , \quad a = 6.5 \quad , \quad b = 2.8 \ .
\end{cases} \tag{2.56}$$

This approach is the one implemented in the PINOCCHIO code (§4.1), where ellipsoidal collapse times are used to construct the merger histories of halos.

Such description of ellipsoidal collapse, although allowing for a very fast solution, can not be trivially extended to the MG case. The reason behind that is the introduction of scale-dependent growth in MG theories (§5); as a consequence, the growth rate cannot be used as time coordinate. In Ruan et al. (2020), the authors extend the Bond & Myers approach to the case of $f(R)$ models, providing the proper evolution equations for ellipsoidal collapse in MG. However, as described in §6.1, solving eq. 2.43 is too computationally demanding for the implementation in a fast approximate method. A suitable compromise is the joint adoption of the Ruan et al. (2020) extension and the Nadkarni-Ghosh & Singhal approach (§2.3.3), to achieve a fast computation of ellipsoidal collapse times in the framework of modified gravity theories. Such approach, discussed in §6, is our choice for the implementation of ellipsoidal collapse with MG in PINOCCHIO.

Chapter 3

Modified Gravity

As discussed in chapter 1, the standard cosmological model relies on GR to describe the gravitational interactions. GR is indeed in remarkable agreement with a wealth of observations, ranging from Solar System tests, gravitational redshift experiments, lensing of light from background stars from the Sun and the anomalous perihelion of Mercury, as well as the Shapiro time–delay measured by the Cassini spacecraft and Lunar laser ranging experiments. Outside the Solar System, GR is also in good agreement with tests involving changes in the orbital period of binary pulsars due to gravitational waves emission (Hulse & Taylor, 1975). The most recent breakthrough in this field is the detection of gravitational waves emitted by merging black holes (Abbott et al., 2016) and neutron stars mergers (Abbott et al., 2017a), together with the detection of their electromagnetic counterpart (Abbott et al., 2017b), and the imaging of the black hole in M87 (Event Horizon Telescope Collaboration et al., 2019).

Despite its remarkable success, a proper test of GR on large cosmological scales is still missing: hence, the application of GR in cosmological studies is actually an extrapolation of the regime of validity of the theory. Moreover, the standard cosmological model requires additional dark components to be consistent with current data. In particular, DE is required to explain the observed accelerated expansion of the Universe (Riess et al., 1998; Perlmutter et al., 1999). Finding a physical explanation to the mechanism behind the accelerated expansion is one of the biggest open questions in modern physics, and the main driver for current and future LSS surveys.

The simplest description for DE is the cosmological constant Λ in the field equations 1.2. However, the introduction of Λ poses some theoretical problems (§3.1). An alternative to the introduction of a cosmological constant is to consider extensions to GR. This possibility has prompted the development of a wealth of MG theories able to explain the accelerated expansion without resorting to a cosmological constant (Amendola & Tsujikawa, 2010; Joyce et al., 2015; Koyama, 2018; Ishak, 2019).

This chapter provides a general overview of the motivations to consider models beyond-ΛCDM, the main classes of MG and their parameterizations, the signatures of MG on cosmological observables as well as current cosmological constraints on such parameters. Particular attention is given to the $f(R)$ class of theories, especially the Hu-Sawicki model (Hu & Sawicki (2007), HS).

3.1 Motivation

The unknown nature of the two principal constituents of our Universe, dark energy and dark matter, could in principle be enough to consider alternatives to GR. On the other hand, stronger motivations come from the so-called "cosmological constant problems", as well as tensions between the value for some cosmological parameters.

3.1.1 Cosmological constant problems

The cosmological constant can be described as an effective cosmic fluid, with an equation of state parameter $w = -1$. This coincides with the equation of state of the vacuum energy associated with quantum fluctuations, connecting the problem of cosmic acceleration to the cosmological constant/vacuum energy problems (Weinberg, 1989; Peebles & Ratra, 2003; Padmanabhan, 2003; Martin, 2012; Burgess, 2013): the discrepancy between quantum predictions for the vacuum energy and the observed value for Λ spans some 120 orders of magnitudes. This first issue is also known as fine-tuning, or "old cosmological constant problem".

A second problem emerged with more precise measurements of cosmic density parameters showing that $\Omega_\Lambda \sim \Omega_{m,0}$: we appear to be living at a very special moment of the history of the Universe, shown by the grey band

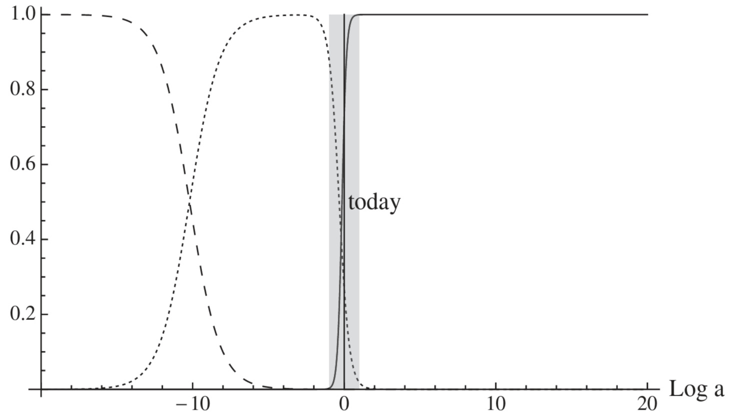

Fig. 3.1: Evolution of the density parameters. Dashed line is Ω_r, dotted line Ω_m, solid line is Ω_Λ. Highlighted in grey is the epoch when $\Omega_m \sim \Omega_\Lambda$. From Sivanandam (2013).

in Fig. 3.1. This appears to be further fine-tuning of the model's parameters, and is known as the coincidence problem or "new cosmological constant problem" (Sivanandam, 2013; Velten et al., 2014).

3.1.2 Tensions

Another motivation to pursue alternatives to GR comes from tensions between the cosmological parameters derived from early versus late cosmological probes. In particular, combining different approaches to measure the Hubble constant H_0 leads to a $\sim 4-5\ \sigma$ tension with early Universe measurements. This can be seen in fig. 3.2: all early Universe data consistently predict lower values of H_0 (CMB data from Planck Collaboration et al. 2018 and a combination of CMB, BBN, BAO and WL data Abbott et al. 2018) with respect to low redshift data. The latter include distance ladder measurements from Cepheids and SNIa (Riess et al., 2019), strong lensing time delays of quasars (Wong et al., 2019), observations of water masers in circum-nuclear orbits around supermassive black holes (MCP, Reid et al. 2009), SNIa calibrated with the tip of the red giant branch (CCHP collaboration, Freedman et al. 2019). The nature of such tension is still debated (Verde et al., 2019): future experiments, with lower statistical errors, will reveal if it is due to systematics, or if it is a signature of new physics and possibly of deviations from GR.

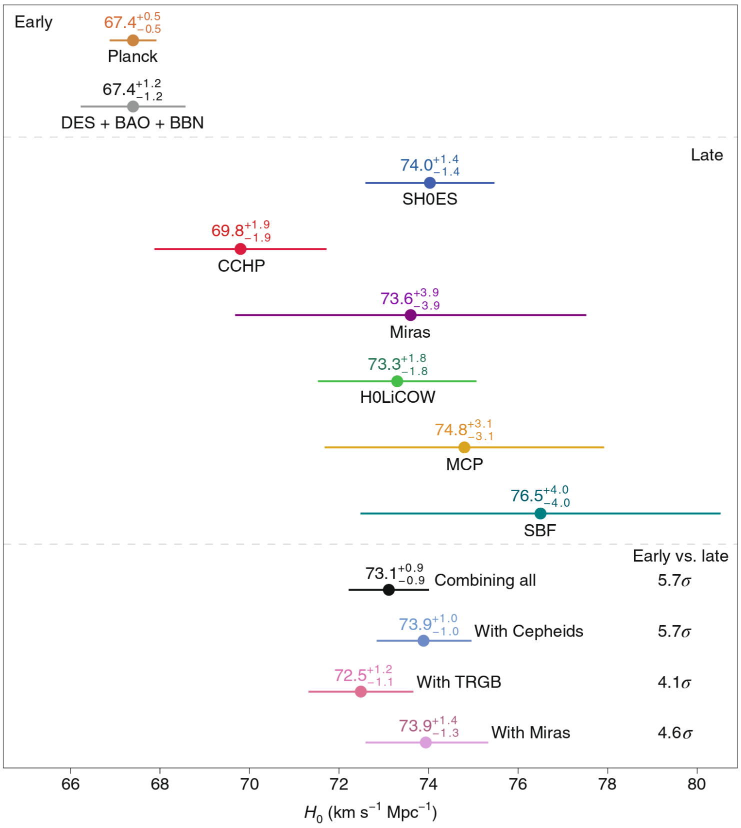

Fig. 3.2: Compilation of Hubble constant measurements from recent data. From Verde et al. (2019).

3.2 Modified gravity theories

There are several ways to characterize extensions to GR, altough none of them provides a neat and satisfactory categorization. Starting from Einstein field equations:

$$R_{\mu\nu} - \frac{1}{2} g_{\mu\nu} R + g_{\mu\nu} \Lambda = 8\pi G T_{\mu\nu} \ , \tag{3.1}$$

a first distinction can be performed between models including modifications to the right hand side of eq. 3.1 as opposed to those modifying the left hand side. The former operate on the stress-energy content of the Universe, and are known as Dark Energy (DE) models, while the latter act on the gravity theory itself, modifying the Einstein-Hilbert action, and are known as Modified Gravity (MG) models. However, drawing a sharp line between the two categories is not straightforward. In Joyce et al. (2015) the authors

use the strong equivalence principle as a characterizing feature: models that satisfy it are DE models, while those violating it are MG models. Another possibility comes from considering Lovelock theorem (Lovelock, 1969, 1971), stating that *the only local, second-order, gravitational field equations that can be derived from a four-dimensional action constructed solely from the metric tensor, and satisfying the conditions of being symmetric and divergence-free, are those of the Einstein field equations with a cosmological constant*.
Theories can therefore be classified according to which requirement they violate (Berti et al., 2015; Koyama, 2018; Amendola et al., 2018a; Ishak, 2019).

A third, more phenomenological categorization is proposed in Amendola et al. (2018a):

- *Standard DE models*: gravity is standard GR and DE does not cluster on sub-horizon scales. One example is a minimally coupled scalar-field with standard kinetic energy, with sound speed $c_s = c$ (e.g. quintessence, Wetterich 1988; Ratra & Peebles 1988);

- *Clustering DE models*: DE has fluctuations and can cluster on sub-horizon scales, resulting in an additional contribution to Poisson equation due to DE perturbations. In terms of the DE parameters (see §3.4), this amounts to having $Q \neq 1$, but still $\eta = 1$ (e.g. k-essence, Armendariz-Picon et al. 2000);

- *MG models*: in these models Einstein field equations are modified, leading to changes in the Poisson equations and $\eta \neq 1$. In particular, these models postulate the existence of a "fifth force", and include scalar-tensor theories, $f(R)$ theories (De Felice & Tsujikawa, 2010) and Dvali-Gabadadze-Porrati theories (DGP, Dvali et al. 2000).

In general, DE models assume that the cosmological constant is a dynamical field (Copeland et al., 2006). Current data constrain the parameter of the DE equation of state to be very close to 1; therefore, an extension of the case of the cosmological constant (with constant $w = -1$) is to consider a time dependent equation of state for DE ($w = w(a)$), approaching its present value through some mechanism. Such models share the presence of an additional degree of freedom affecting the background evolution, resulting in modified Friedmann equations, but with unchanged fluid equations. As a consequence, these models do not affect structure formation directly, but only the expansion rate of the Universe.

A first class of models that falls in the MG category is coupled DE. This includes models where DE, identified with a dynamical scalar field, interacts with other components of the Universe. The coupling introduces a fifth force, effectively modifying the gravitational interaction and therefore structure formation, resulting in distinctive signatures in the cosmological observables. The case of coupling with all species include scalar-tensor theories and $f(R)$ models.

3.3 Screening mechanisms

All MG models postulate additional degrees of freedom in the gravitational sector that, when coupled to matter, effectively introduce a fifth force. In order to comply with tight Solar System constraints, any viable MG models should include a screening mechanism to locally "hide" the additional degrees of freedom, so that on small scales GR is restored. Screening can be relevant in regions where the Newtonian potential Φ_N or its derivatives become large, suggesting the following classification scheme:

- *Large field values*: this type of screenings activate in regions where Φ_N exceeds some threshold, hence the largest deviations from GR should appear in regions where Φ_N is small. Large values of the potential may cause the coupling with matter to weaken, the mass of the scalar field to increase, or the self-coupling to the field to become large. Examples are chameleon (Khoury & Weltman, 2004a,b), dilaton (Damour & Polyakov, 1994; Brax et al., 2011) or symmetron (Olive & Pospelov, 2008; Hinterbichler & Khoury, 2010) screening:
    - *Chameleon*: the scalar field takes a background value $\bar{\psi}$ determined by the background density. The potential introduces a mass term for the scalar field perturbation $m(\psi)$ which depends on the background field, and that does not propagate beyond the Compton length m^{-1}. Large masses correspond to screened regions: this can happen in dense environments, e.g. in the Solar System. On the other hand, on cosmological scales the density (and thus $m(\psi)$) is small, allowing for deviations from GR;

  - *Dilaton and symmetron screening*: In this case, the coupling of the scalar field to matter is determined by a function $\omega(\psi)$, again depending on the background scalar field $\bar{\psi}$ and therefore on the background density. It is possible to have models where $\omega(\bar{\psi})$ is large in dense environments, so that the scalar field decouples from matter, while $\omega \sim \mathcal{O}(1)$ on cosmological scales;

- *First derivatives*: this form of screenings appears when $\nabla\Phi_N$ exceeds some threshold. And example is given by k-mouflage screening (Babichev et al., 2009; Brax & Valageas, 2014a,b);

- *Second derivatives*: these activate in regions of high curvature, where $\nabla^2\Phi_N$ is large, therefore the largest deviations from GR are expected to be in regions of low curvature. Such models rely on non-linearities of the second derivative of the scalar field. One example is Vainshtein screening (Vainshtein, 1972), associated with galileon and massive gravity.

Extensive reviews on screening mechanisms can be found in Khoury (2010); Joyce et al. (2015); Burrage & Sakstein (2018).

3.4 Parametrizations

Given the large number of proposed MG theories, a thorough exploration of the parameter space is rather cumbersome, and a possible approach is to use a parameterization able to account for several models. This involves considering general time- and scale- dependent functions; such a parameterization should in principle be able to capture all relevant physics with the least number of parameters. Useful parameterizations can be motivated by predictions for specific theories of MG/DE (Song et al., 2010) or by measurability (Amendola et al., 2018b): the latter implies measuring departures from a fiducial model (i.e. ΛCDM). Approaches to parameterization can be based on:

- *Model parameters* capturing the degrees of freedom of DE/MG and modifying the evolution equations of the energy-momentum content with respect to a fiducial model. Such parameters can be associated with physical effects, and have a specific behavior for different theories;

- *Trigger relations* derived directly from observations: these are constructed to break down if the data do not describe the features predicted by the fiducial model. A widely used trigger relation derives from the growth rate $f(a) = \mathrm{d}\log D/\mathrm{d}\log a \sim \Omega_m(a)^\gamma$. In ΛCDM, $\gamma \simeq 0.545$ (Linder, 2005): deviations from this value could suggest extensions of the standard scenario. In general, it is possible to consider a time and scale dependent function $\gamma(k, a)$ (e.g. Nunes & Mota 2006; Linder & Cahn 2007).

A common way to parameterize DE models is via a time dependent equation of state. The most common parameterization is (Chevallier & Polarski, 2001; Linder, 2003):

$$w(a) = w_0 + w_a(1 - a) \ . \tag{3.2}$$

Different parameterizations were proposed e.g. in Huterer & Turner (2001); Maor et al. (2001); Weller & Albrecht (2001) (linear and logarithmic parameterizations in z), Bassett et al. (2004) (rapidly varying equation of state). Current constraints on w_0, w_a are summarized in §3.6.1, while forecasts for Euclid can be found in §1.5.

Any generic modification of the dynamics of scalar perturbations beyond the simple scenario of evolving DE can be obtained with the introduction of two new degrees of freedom, encoded in the equations for the metric potentials as:

$$-k^2\Phi = 4\pi G Q(a,k) a^2 \rho_m \delta_m \quad , \quad \Phi = \eta(k,a)\Psi \tag{3.3}$$

In MG models the function $Q(a, k)$ represents a mass screening effect due to local modifications of gravity, and effectively modifies Newton constant. In clustering DE models Q represents the additional clustering due to the DE perturbations. On the other hand, the function $\eta(a, k)$ parameterizes the effective anisotropic stress (ratio of the metric potentials, $\eta = 1$ in ΛCDM) introduced by MG or DE. The functional form of Q and η depend on the particular model considered. In general, Q and η can be combined to obtain different sets of parameterizations (Amendola et al., 2018b; Pogosian et al., 2010; Song et al., 2010). A common alternative to (Q, η) is:

$$\mu = \frac{Q}{\eta} \quad , \quad \Sigma = \frac{Q}{2}\left(1 + \frac{1}{\eta}\right) \ , \tag{3.4}$$

leading to modified linear (Fourier space) Poisson equations for the potentials:

$$\begin{aligned} -k^2\Psi &= 4\pi G a^2 \mu(k,a)\rho_m\delta_m \\ -k^2(\Psi+\Phi) &= 8\pi G a^2 \Sigma(k,a)\rho_m\delta_m \end{aligned} \tag{3.5}$$

A summary of different parameterizations can be found in Daniel et al. (2010). The pair (μ, Σ) was shown to be particularly suited when combining CMB data with galaxy survey data (Daniel & Linder, 2010; Zhao et al., 2010; Axelsson et al., 2014).

3.5 $f(R)$ gravity

The $f(R)$ family of models is one of the most popular and well studied modifications of GR (see Sotiriou & Faraoni 2010, De Felice & Tsujikawa 2010 for reviews). Indeed, one of the simplest extensions of GR is to modify the Einstein-Hilbert action by substituting the Ricci scalar with a generic function $f(R)$:

$$\mathcal{S} = \frac{1}{16\pi G}\int \mathrm{d}^4x\sqrt{-g}f(R) + \int \mathrm{d}^4x\sqrt{-g}\mathcal{L}_m(\psi_m, g_{\mu\nu}) \ , \tag{3.6}$$

where $\mathcal{L}_m$ is the Lagrangian of the matter field ψ_m. By varying the action with respect to the metric, one obtains the modified field equations:

$$f_R R_{\mu\nu} - \frac{1}{2}g_{\mu\nu}f(R) + (g_{\mu\nu}\Box - \nabla_\mu\nabla_\nu)f_R = 8\pi G T_{\mu\nu} \ , \tag{3.7}$$

where $f_R = \mathrm{d}f/\mathrm{d}R$ and $\Box$ is the d'Alembert operator. If $f(R) = R$, eq. 3.7 reduces to standard GR, and the field equations are second-order in derivatives of the metric. In all other cases, eq. 3.7 contains up to fourth-order derivatives of the metric $g_{\mu\nu}$.

It can be shown that theories with an action of the form of eq. 3.6 are equivalent to GR plus a non-minimally coupled scalar field (Bicknell, 1974). This can be obtained by means of a conformal transformation of the form $\bar{g}_{\mu\nu} = g_{\mu\nu}f_R$ (Maeda, 1989). Defining $\phi = \sqrt{3/16\pi G}\ln f_R$, the field equations become:

$$\bar{R}_{\mu\nu} - \frac{1}{2}\bar{g}_{\mu\nu}\bar{R}_{\mu\nu} = 8\pi G\left(\phi_{,\mu}\phi_\nu - \frac{1}{2}\bar{g}_{\mu\nu}\bar{g}^{\rho\sigma}\phi_{,\rho}\phi_{,\sigma} - \bar{g}_{\mu\nu}V\right) + 8\pi G\bar{T}_{\mu\nu} \ , \tag{3.8}$$

with $V = V(\phi) = (Rf_R - f(R))/16\pi G f_R^2$. Another possibility is to apply a Legendre transformation so that the field equations take the form of a scalar-tensor theory. The action can be written as

$$\mathcal{S} = \frac{1}{16\pi G} \int \mathrm{d}^4x\sqrt{-g}[f(\xi) + (R - \xi)f'(\xi)] \ , \tag{3.9}$$

where ξ is a new field and $f' = \mathrm{d}f/\mathrm{d}\xi \equiv \phi$. It is possible to define a potential:

$$\Lambda(\phi) \equiv \frac{1}{2}\left[\xi(\phi)\phi - f(\xi(\phi))\right] \ , \tag{3.10}$$

so that the action is

$$\mathcal{S} = \frac{1}{16\pi G} \int \mathrm{d}^4x\sqrt{-g}\left[\phi R - 2\Lambda(\phi)\right] \ . \tag{3.11}$$

which is a scalar-tensor theory with coupling constant $\omega = 0$. The metric is the same as in eq. 3.6, so the coupling of the field ϕ to the matter fields is unchanged.

There are several functional forms for $f(R)$, but all the viable ones must comply with theoretical and phenomenological constraints:

- The first and second derivatives must be positive, i.e. $f_R = df/dR > 0$, $f_{RR} = d^2f/dR^2 > 0$. This is required to avoid instabilities in the high curvature regime;
- The derivative f_R evaluated today must be $|f_{R0}| \ll 1$ to satisfy Solar System constraints.

This is a particular case of models showing chameleon screening, i.e. the scalar field acquires a mass in high density environment, effectively hiding additional degrees of freedom and restoring GR.

$f(R)$ models can be applied to the description of stellar formation and evolution (Capozziello et al., 2011), gravitational waves emission (De Laurentis & De Martino, 2013), rotation curves of spiral galaxies and the velocity dispersion of elliptical galaxies (Cardone & Capozziello, 2011; Napolitano et al., 2012), cluster of galaxies (Peirone et al., 2017; Pizzuti et al., 2017). In the context of cosmology, $f(R)$ models can be used to explain both early (inflation) and late time accelerated expansion. Possible models include Starobinsky (1980), Hu & Sawicki (2007) (see §3.5.1), Appleby & Battye (2007), Cognola et al. (2008).

3.5.1 Hu–Sawicki $f(R)$

One of the $f(R)$ models that evade Solar System constraints was proposed in Hu & Sawicki (2007) (HS). The functional form of $f(R)$ is chosen to comply with the following constraints:

- At high redshift the cosmological model mimics ΛCDM;
- At low redshift the expansion is accelerated, in a way similar way to ΛCDM but without the need of a cosmological constant;
- There are sufficient additional degrees of freedom to have a screening mechanism in place.

Satisfying these constraints means that $f(R)$ should satisfy:

$$\lim_{R\to\infty} f(R) = \text{const.} \quad , \quad \lim_{R\to 0} f(R) = 0 \tag{3.12}$$

These requirements are met by a broken power–law model:

$$f(R) = -m^2 \frac{c_1 (R/m^2)^n}{c_2 (R/m^2)^n + 1} \ . \tag{3.13}$$

with c_1, c_2 and n dimensionless parameters of the model and m^2 is a mass scale, defined as $m^2 = H_0^2 \Omega_{m,0}$. By imposing a background expansion that mimics the ΛCDM expansion history, c_1 and c_2 are constrained to be $c_1/c_2 \approx 6\Omega_m/\Omega_\Lambda$, therefore the model has only two free parameters, commonly expressed in terms of the index n and the value f_{R0}.

Hu-Sawicki $f(R)$ is one of the most studied among $f(R)$ models, and it is included as one of the basic models in several numerical codes to compute cosmological observables in the context of MG (see §3.7).

3.6 Cosmological probes of the gravity theory

Cosmological probes can broadly be divided in two categories: those probing the expansion history of the Universe and its geometry, for example via distance measurements and the expansion rate, and those constraining the growth and formation history of structures. Combining the two allows to tighten the constraints on cosmological parameters, and possibly break degeneracies. However, to test MG models, growth measurements are the most useful, providing a test of the gravity theory in the Newtonian limit on sub-horizon scales. Current constraints on MG from cosmological measurements are summarized in §3.6.1.

The general approach to constrain MG models from data is to consider the parameterizations described in §3.4. Usually, constraints are placed on the linear evolution of density fluctuations. However, considering only the linear regime is limiting, since most of the information is contained in the non-linear regime of structure formation. On the other hand, investigating NL scales requires in general a model-by-model approach. Signatures in the linear regime include:

- *CMB*: typically, MG affects the large scale amplitude of the temperature and the lensing potential power spectrum. Therefore, CMB measurements can be used to constrain the η parameter;

- *Growth rate* $f = \mathrm{d}\ln D/\mathrm{d}\ln a$: it probes the linear growth of density perturbations, hence it can constrain deviations from GR in terms of the μ parameter;

- *Galaxy clustering*: already at scales $k \sim 0.1\ h^{-1}$ Mpc the matter power spectrum could be enhanced by the presence of the MG fifth force. Such modification can in principle be scale dependent.

Probes for the non-linear regime include:

- *Halo counts*: the halo mass function is affected because of changes in the critical density for collapse, resulting in general in a higher abundance of massive halos with respect to the standard GR case. Computing predictions involves properly taking the screening mechanism into account;

- *Dynamical vs. lensing mass estimates* are different for models with $\mu \neq 0$, $\Sigma = 0$ (such as for scalar-tensor theories or DGP models), hence the lensing mass can be different from the dynamical mass, estimated assuming GR;

- *Voids*, being low density regions, can exhibit un-screened MG effects, in particular in their lensing profile.

3.6.1 Constraints on beyond-ΛCDM models

In this section I give a brief review of current constraints on MG theories from cosmological data. In general, test of the gravity theory are performed in terms of deviations of the parameterizations described in §3.4 from their GR value.

Fig. 3.3 shows the results obtained combining galaxy clustering and weak gravitational lensing data from the DES Y1 survey (Abbott et al., 2019), together with external datasets that include CMB (from Planck), BAO (from SDSS, 6dF and BOSS), RSD (from BOSS) and SNIa (from the Pantheon compilation). The constraints on the time-varying DE equation of state parameters are $w_0 = -1.01^{+0.04}_{-0.04}$, $w_a = -0.28^{+0.37}_{-0.48}$, shown in the left panel. The right panel shows constraints on the MG parameters $\Sigma_0 = 0.06^{+0.08}_{-0.07}$, $\mu_0 = -0.11^{+0.42}_{-0.46}$. In both cases, the results are consistent with the standard ΛCDM model with GR, shown as grey dashed lines.

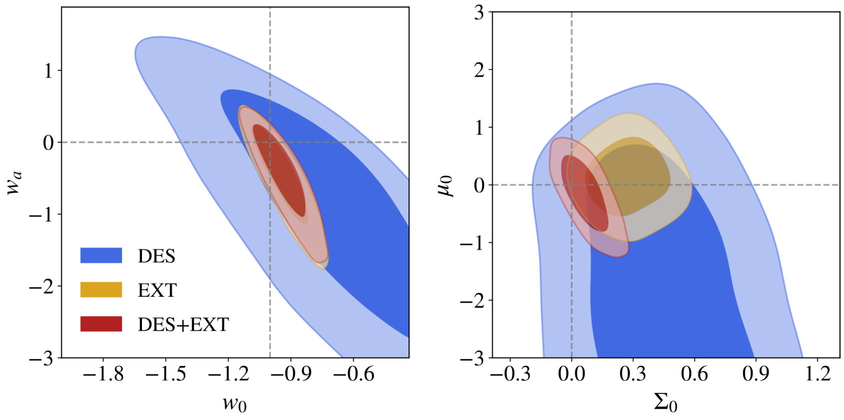

Fig. 3.3: *Left*: Constraints on the DE equation of state parameters (w_0, w_a) (left) and modified gravity parameters (Σ_0, μ_0) (right). Blue contours show the 68% and 95% confidence regions from DES alone, yellow is external data (from Planck, BOSS and the Pantheon SNIa compilation) alone, and red is the combination of the two. The intersection of the horizontal and vertical dashed lines shows the parameter values in the ΛCDM model (left panel) and in general relativity (right). From Abbott et al. (2019).

Fig. 3.4 shows the constraints on w_0, w_a (left panel) and the MG parameters μ_0, η_0 (right panel) from CMB data (Planck Collaboration et al., 2018). The tightest constraints on the DE equation of state are provided by a combination of Planck data with BAO and SNIa, resulting in $w_0 = 0.961 \pm 0.077$, $w_a = -0.28^{+0.31}_{-0.27}$. The right panel shows the marginalized posterior distributions of the MG parameters μ and η. The tightest constraints are provided by combination with BAO, RSD and WL data: $\mu_0 - 1 = -0.07^{+0.19}_{-0.32}$, $\eta_0 - 1 = 0.32^{+0.63}_{-0.89}$. It is worth noting that in this analysis the scale-dependence of the MG parameters is not taken into account. Again, there is no significant evidence for deviations from the standard cosmological model.

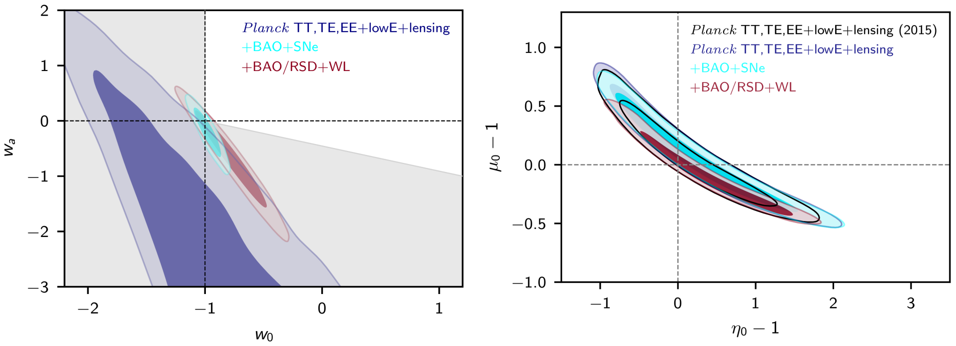

Fig. 3.4: *Left*: Marginalized posterior distributions for (w_0, w_a) for various data combinations. *Right*: Marginalized posterior distributions for the MG parameters (μ, η), obtained neglecting any scale dependence. In both panels the ΛCDM values are shown as dashed lines, while the black contours in the right panel show the Planck2015 results. From Planck Collaboration et al. (2018)

Fig. 3.5 shows the constraints on the DE parameters w_0, w_a and the MG parameters Q, Σ, derived from WL data provided by the KiDS survey Joudaki et al. 2018. The constraints on the DE equation of state (left panel) are weak, but still consistent with the standard model shown as grey dashed lines. The right panel shows marginalized posterior distributions for the MG parameters Q, Σ. Again, in both cases the results are consistent with the standard ΛCDM model. In the KiDS analysis, the MG parameters are divided in two redshift bins and two scale bins, with transition at $k = 0.05\ h$ Mpc^{-1} and $z = 1$; the plot shows constraints for the low-z,high-k bin.

It is worth mentioning the constraints on MG models that can be obtained from gravitational wave propagation. The simultaneous detection of gravitational waves from a neutron star merger by LIGO/VIRGO and observation of a short gamma ray burst by Fermi/Integral allowed to put stringent bounds on the difference between the speed of GW propagation and the speed of light. The observed time delay between the two observations was

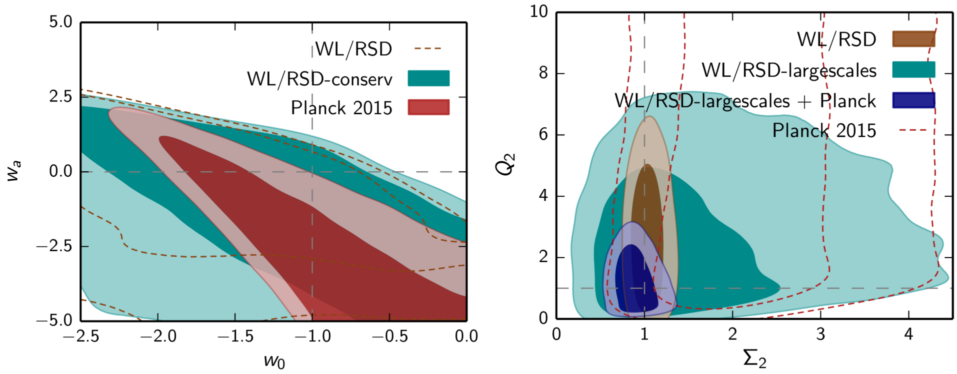

Fig. 3.5: Constraints on the dark energy parameters (left) and MG parameters (right) from KiDS data (Joudaki et al., 2018).

$1.74 \pm 0.05s$, resulting in:

$$-3 \times 10^{-5} < \frac{c_{GW}}{c} - 1 < 7 \times 10^{-16} \,. \tag{3.14}$$

This constraint has heavy implications for all MG models that predict a change in the GW propagation speed, severely limiting the viable theory space (see e.g. Creminelli & Vernizzi 2017; Amendola et al. 2018b).

3.6.2 Degeneracy with massive neutrinos

Recently, attention was been drawn to possible degenerate effects that might arise when one considers MG in presence of massive neutrinos. The effect of massive neutrinos on cosmological observables are briefly outlined in section 4.2. Massive neutrinos affect cosmological quantities by damping the growth of structures on small scales (Lesgourgues et al., 2013). Since modified gravity models predicts an enhancement in the growth of structures, the two effects are degenerate, and might result in the inability to distinguish MG+massive neutrino cosmologies from the standard scenario (Baldi et al. 2014, see e.g. fig. 3.6). Recent works have shown that investigating redshift-space quantities can help in breaking the degeneracies (Hagstotz et al., 2019; Wright et al., 2019).

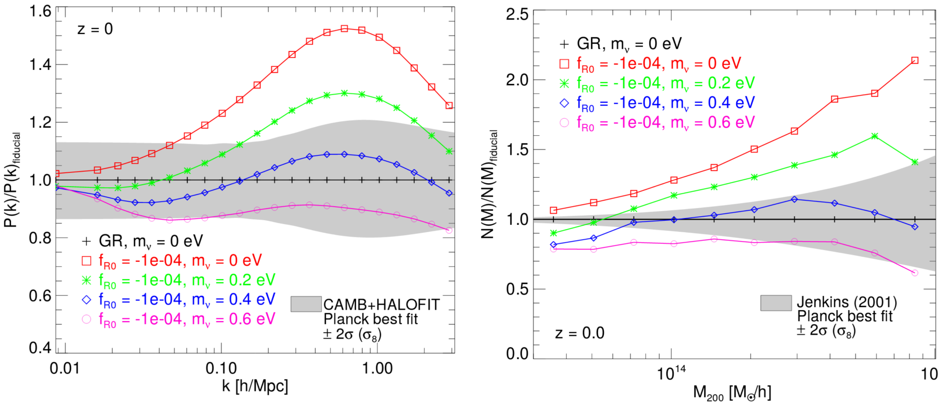

Fig. 3.6: Matter power spectrum (left) and halo mass function (right) for cosmologies that include both MG and massive neutrinos. The MG model considered is $n = 1$ Hu-Sawicki, with different values of the f_{R0} parameter, as described in the legend. The neutrino mass range considered is $0 - 0.6$ eV. From Baldi et al. (2014).

3.7 Simulations with MG

As described in §2.2.1, N-body simulations are the standard tools to compute LSS observables in the fully non-linear regime. Hence, reliable N-body simulations that implement MG models are required in order to robustly test the gravity theory, especially in light of forthcoming high precision cosmological data.

In most cases, MG theories include an additional degree of freedom φ which mediates a fifth force. As a consequence, the Einstein and fluid equations are augmented by an equation of motion for φ. For the specific case of $f(R)$ gravity, the equations to solve are:

$$\begin{aligned} \frac{1}{a^2}\nabla^2\Phi &= \frac{16\pi G}{3}\bar{\rho}\delta + \frac{1}{6}\delta R \\ \frac{3}{a^2}\nabla^2 f_R &= -8\pi G\bar{\rho}\delta - \delta R\,, \end{aligned} \tag{3.15}$$

where $\delta R = R - \bar{R}$ are perturbations of the Ricci scalar and $f_R = \mathrm{d}f/\mathrm{d}R = \varphi$ plays the role of the scalar degree of freedom. The screening mechanism is realized through non-linearities in the equation for $\nabla^2 f_R$, which result in a complex interplay between the matter distribution and the magnitude of the fifth force. Hence, in addition to the system of equations solved in standard N-body simulations, MG simulations must also solve the non-linear equation of motion of the scalar field. Performing such task adds to the already high computational cost of standard N-body simulations, thus requiring the development of new numerical techniques. Early efforts were made in this direction by solving the equation for φ on a fixed grid, as in Oyaizu (2008), Schmidt (2009), Khoury & Wyman (2009). Further improvements involved the implementation of adaptive mesh refinements, thus allowing for a better resolution on small scales (Li & Zhao, 2009) and adaptive-mesh parallel codes. Examples of parallel codes that implement MG with an AMR scheme include ECOSMOMG (Li et al., 2013), ISIS (Llinares & Mota, 2013) and MG-GADGET (Puchwein et al., 2013). The latter is an extension of the TreePM+SPH simulation code P-GADGET3, itself based on GADGET2 (Springel, 2005), which efficiently include modified gravity theories relying on multigrid acceleration. MG-GADGET allows also to include massive neutrinos in MG simulations (Baldi et al., 2014).

Multigrid acceleration is a numerical technique developed to speed up the numerical convergence of the partial differential equation for φ. In a general particle-mesh scheme, at every time step in the simulation an N-body solver computes the density field from particle positions, uses the density to evaluate the gravitational potential via Poisson equation and plugs the potential in the geodesic equation to move particles. To make the process more efficient, Poisson equation is usually solved by means of FFTs. In the context of MG however this is in general not possible, because of the non-linearities in the equations introduced by the presence of φ. Such difficulty can be overcome with the adoption of an FFT-relaxation method if the equations are solved on fixed grids, while for the case of irregularly shaped grids the technique adopted consists in discretizing the equation for φ on a grid and using an iterative scheme to obtain improved solutions.

In §5, propose an approximate way of computing 2LPT displacements in $f(R)$ modified gravity (Moretti et al., 2019). In order to assess the performances of said approximation, I take advantage of simulations run with MG-GADGET with Hu-Sawicki $f(R)$ (Giocoli et al., 2018) and compare the halo power spectrum obtained from our approximate method to the one measured from the MG N-body simulations, showing that our method allows to recover the halo power spectrum within 10% up to mildly-NL scales of $0.2 - 0.4\ h\ \mathrm{Mpc}^{-1}$.

Chapter 4

The PINOCCHIO code

As discussed in §1.5, future galaxy redshift surveys will provide a large amount of high precision data. Placing tight constraints on cosmological parameters requires being able to keep systematics under control and a proper computation of covariance matrices for different cosmological observables (§1.3.2), both for the standard ΛCDM model and its extensions. To achieve this purpose, thousands of different realizations (for each model under investigation) are required. Such a task cannot be tackled with computationally expensive N-body simulations, but it can be faced with the aid of approximate methods (§2.2.2), fast and able to properly reproduce LSS features in the mildly non-linear regime.

The PINOCCHIO[1] (PINpointing Orbit Crossing Collapsed HIerarchical Objects) software implements an approximate method to quickly generate simulated halo catalogs. The package is discussed in Monaco et al. (2002a,b, 2013), and has been extended to second and third-order LPT (Munari et al., 2017b) and massive neutrino cosmologies (Rizzo et al., 2017). PINOCCHIO has been used to generate simulated halo catalogs for the VIPERS survey (de la Torre et al., 2013), and is currently being used within the Euclid collaboration for the computation of covariance matrices in the context of standard ΛCDM.

This PhD work is mainly focused on extending PINOCCHIO to beyond-ΛCDM models. In §4.3 I thoroughly test an approach to extend the code to WDM models. Such tests highlight the inability of the code to reproduce a

---

[1] `https://github.com/pigimonaco/Pinocchio`

WDM mass function, possibly related to a wrong calibration of the fragmentation part of the algorithm. However, the re-calibration process is rather lengthy, and the code is currently undergoing major development, therefore we leave it for a future work. In the next chapters (§5, §6) I give a thorough description of the steps taken to extend the code to MG models, focusing in particular on $f(R)$ models.

4.1 Description of the code

The PINOCCHIO code is based on three theories described in §2: Lagrangian perturbation theory, ellipsoidal collapse, and excursion set theory. PINOCCHIO performs two main task: the computation of collapse times and the fragmentation of collapsed elements into distinct objects, mimicking the hierarchical formation of structures. I give a detailed description of how the code works throughout this section, though the main steps can be summarized as follows:

- The code generates a linear density field on a regular grid in Lagrangian space;
- The field is smoothed on a set of scales (smoothing radii). For each smoothing radius the collapse time (CT) for each particle is computed, and the earliest CT is stored;
- Overdensities are treated as homogeneous ellipsoids: for each particle, the code computes the CT (defined as the time of orbit crossing, when the first axis of the ellipsoid goes to zero) as the earliest collapse time, considering all smoothing scales. Collapse times are computed with the LPT approach (§2.3.3);
- After CT are computed, particles are displaced using LPT (up to third order). Collapsed particles can be accreted onto a halo or become part of a filament;
- Halos are also displaced with LPT, and they can merge if they get close enough, i.e. their distance is below some threshold.

Initial conditions are set by generating a realization of a Gaussian field on N points of a cubic grid with side L; this can be done by inserting a tabulated linear power spectrum (e.g. generated with CAMB, Lewis & Challinor 2011), or by means of the fit of Eisenstein & Hu (1998). The Gaussian field, assumed to represent a linear density field, is smoothed on a set of smoothing radii R (typically $\sim$ 10-20), by means of a Gaussian filter. Smoothing radii are chosen so that the corresponding mass variances are logarithmically spaced in intervals of 0.15 dex.

The next step is the computation of CT: the evolution of mass elements is described as the evolution of ellipsoids, whose principal axes are given by the deformation tensor (Hessian of the peculiar gravitational potential). Using the linear growth rate as a time coordinate, the evolution of the ellipsoid is described with third order LPT (§2.3.3) until the time of orbit crossing, after which the perturbative approach breaks down. Since the LPT approach is slow to converge in the spherical case, leading to a significant overestimate of CT, the empirical correction of eq. 2.55 is adopted to properly reproduce spherical collapse. The deformation tensor is estimated for each smoothing radius using Fast Fourier Transforms (FFTs), and the code evaluates and stores the inverse collapse time $F(\vec{q}) = 1/D_1(t_{\rm coll}(\vec{q}))$ at which the mass element at $\vec{q}$ is predicted to collapse. Therefore, for each grid point the code evaluates a set of inverse collapse times F (one for each smoothing R), and assigns to the mass element the earliest CT, corresponding to the maximum of the inverse collapse time $F_{\rm max}$, with corresponding smoothing scale $R_{\rm max}$.

In order to construct halo catalogs, the software implements an algorithm to mimic the hierarchical formation of structures. After the computation of collapse times, particles (grid points) are sorted in order of descending $F_{\rm max}$. To determine whether a collapsing particle form a new halo, gets accreted on an existing halo or becomes a filamentary particle, its six grid neighbors are considered:

- A collapsing particle lacking collapsed neighbors is tagged as a new DM halo (with one particle);

- If the particle is *close enough* to a halo, it is considered for accretion. To determine whether accretion takes place, both the particle and the halo are displaced with LPT. By calling d their distance, the particle gets accreted if $d < d_{\rm thr}$, with the threshold set to:

$$d^2_{\rm thr} = \begin{cases} (fR^e)^2 + (f_{200}R)^2 & D\sigma \leq D\sigma_0 \\ \{fR^e[1 + s(D\sigma - D\sigma_0)]\} + (f_{200}R)^2 & D\sigma > D\sigma_0 \end{cases} \tag{4.1}$$

where R is the Lagrangian radius in grid units, $D\sigma$ is the standard deviation of the un-smoothed density and $f_{200} = (200)^{-1/3}$ (set by requiring the halo density to be 200 times that of the background). e, s and f are free parameters determined through a calibration process to reproduce a universal mass function. If the particle is not accreted, it is tagged as belonging to a filament;

- If the particle is close to more than one halo, the algorithm first verifies whether the particle gets accreted to the closer (in terms of d/R) halo. Then it computes the distance between the halos to check for halo merging;
- A particle close to one or more filament particles is tagged as filament as well.

Fig. 4.1 (Munari et al., 2017b) shows an example of halo mass function computed with PINOCCHIO, compared to the result of N-body simulations (blue dashed line) and the analytic fit of Crocce et al. (2010) (solid black line). PINOCCHIO mass functions are shown for different LPT orders (Zel'dovich approximation as purple dotted line, 2LPT as orange dashed line, 3LPT as red solid line). The bottom panes show residuals with respect to the analytic fit, confirming PINOCCHIO can reproduce the analytic prediction with $\sim$ 5% accuracy.

The advantage of using LPT is clear: the code can work without the need of time-steps, and is able to readily generate its outputs at any given redshift. PINOCCHIO outputs include DM halo catalogs and merger trees with continuous time sampling, as well as past light cones. Additionally, the code can generate GADGET-like snapshots with particles displaced with LPT, both in real and redshift space. The PINOCCHIO approach is particularly convenient, especially for the generation of merger trees and past light cones. In general, approximate methods based on particle-mesh integrations over few time-steps suffer from poor time sampling of halo merger histories. Sparse time-sampling also complicates the generation of halo catalogs along the

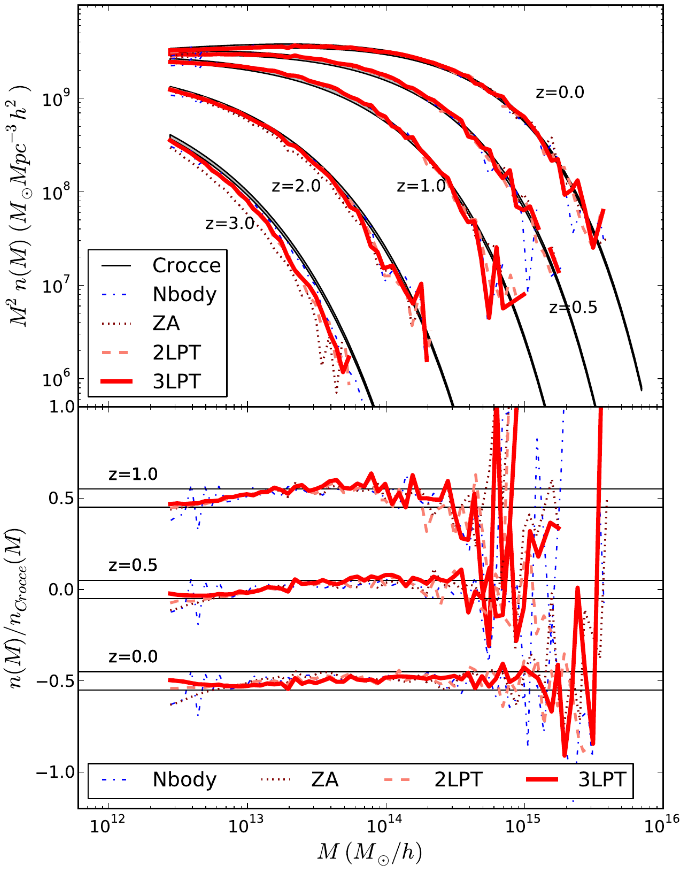

Fig. 4.1: Halo mass function obtained from PINOCCHIO for different redshifts using three different LPT orders to construct halos. The black line shows the analytic fit of Crocce et al. (2010), while dashed blue line is obtained from an N-body simulation. The lower panel shows residuals with respect to the analytic fit, with horizontal black lines marking the $\pm 5\%$ region. From Munari et al. (2017b).

past light cone. On the other hand, in PINOCCHIO all displacements are evaluated with a single time-step, thus making any level of time-sampling easy to achieve. In particular, halo masses are updated every time a particle is added to a group, and merger histories report masses for each pair of merging of haloes. Hence, mass accretion histories are available for each merger event, without the need to output the halo catalogs many times.

4.2 Extension to massive neutrinos

Although in the standard model of particle physics neutrinos are described as fundamental massless particles, the discovery of the neutrino oscillations phenomenon has shown that at least two of the three neutrino families are indeed massive (Forero et al., 2012), establishing a lower bound on the sum of the neutrino masses $\sum_i m_{\nu_i} \geq 0.06$ eV. Such discovery has been one of the most important of the last decades, pointing towards the existence of physics beyond the standard model. Massive neutrinos affect cosmological quantities in several ways (Lesgourgues et al., 2013), therefore precise cosmological analyses require to properly account for them. Massive neutrinos become non-relativistic quite late ($z_{\rm nr} \sim 2000$) in the thermal history of the Universe, but they decouple fairly early ($z_{\rm dec} \sim 10^9$). As a consequence they maintain relatively large velocities with respect to other massive particles. Thus, they can be considered as a secondary, diffuse matter component with a thermal free-streaming velocity. The latter acts as an effective pressure term, setting a scale below which the growth of neutrino perturbations is strongly suppressed. Such scale is called the free-streaming length and can be written as:

$$k_{\rm fs} = \sqrt{\frac{3}{2}\Omega_m(a)}\frac{aH(a)}{c_\nu(a)} \ , \tag{4.2}$$

where $c_\nu(a) = \delta P_\nu / \delta \rho_\nu$ is the sound speed corresponding to the effective neutrino pressure. The evolution of neutrino perturbations is coupled to that of CDM, resulting in a suppression of growth also for the cold component. Moreover, the presence of a free-streaming scale results in a scale-dependent growth rate $D(t, R)$.

Castorina et al. (2014) showed that neutrinos do not cluster significantly on small scales, despite contributing to the expansion rate of the Universe. For this reason, the halo mass function and halo bias in a cosmology with massive neutrinos can be described in terms of the CDM plus baryons density field. It is then possible to generate simulated halo catalogs by providing PINOCCHIO with the proper power spectrum P_{cb}, as done in Rizzo et al. (2017). In order to introduce the scale-dependent growth due to massive neutrinos, Fourier-space linear growth factors are obtained from the linear CDM+baryons power spectrum $P_{\rm cb}(k,t)$ generated with the CAMB Boltzmann solver for a given cosmological model, on a grid of $N_{\rm CAMB} = 150$

output times, logarithmically spaced in scale factor from $a = 0.01$ to $a = 1$. The (now scale-dependent) growth factor is no longer used as a time variable, since ellipsoidal collapse is evaluated at a fixed value of the smoothing radius R. Moreover, because of the scale-dependence of $D_1(k,t)$, the density and velocity growth factors in configuration space differ. Therefore, the latter are obtained by means of two different integrals:

$$\begin{aligned} D_\delta^2(t,R) &= \frac{\int_0^\infty P_{cb}(k,t)\tilde{W}^2(kR)k^2\mathrm{d}k}{\int_0^\infty P_{cb}(k,t_0)\tilde{W}^2(kR)k^2\mathrm{d}k} \\ D_v^2(t,R) &= \frac{\int_0^\infty P_{cb}(k,t)\tilde{W}^2(kR)\mathrm{d}k}{\int_0^\infty P_{cb}(k,t_0)\tilde{W}^2(kR)\mathrm{d}k} \end{aligned} \tag{4.3}$$

where $\tilde{W}$ is the Fourier transform of the window function, and denominator quantities are needed to normalize the growth factor at some reference time t_0. The second-order growth rate, needed to displace particles with 2LPT, is computed adopting the fit proposed by Bouchet et al. (1995), shown to be accurate at percent level for a wide range of values of the cosmological parameters:

$$D_2 = -\frac{3}{7}D_1^2\Omega_m(a)^{-1/143}\,. \tag{4.4}$$

The above expression was derived for massless-neutrino cosmologies; 2LPT displacements are therefore implemented in PINOCCHIO under the assumption that eq. 4.4 is accurate enough even in presence of massive neutrinos, provided that the linear growth rate is the scale dependent one derived from eq. 4.3. Fig. 4.2 and 4.3 show respectively the halo mass function and the power spectrum obtained from PINOCCHIO with massive neutrinos, confirming that the approximating D_2 with the fit of eq. 4.4 does not result in a significant worsening of the predictive power of the code. In particular, the halo mass function at $z = 0$ (left) and $z = 1$ (right), plotted in Fig. 4.2 for different neutrino masses, show $\leq$10% agreement with both N-body simulations and the analytic fit of Crocce et al. (2010) (middle and bottom panel respectively). Fig. 4.3 shows the real space halo power spectrum at $z = 0$ (left) and $z = 1$ (right), confirming that PINOCCHIO is able to recover the clustering properties of DM halos, with $\sim$ 10% deviation respect to the results of N-body simulations, for a wide range of neutrino masses.

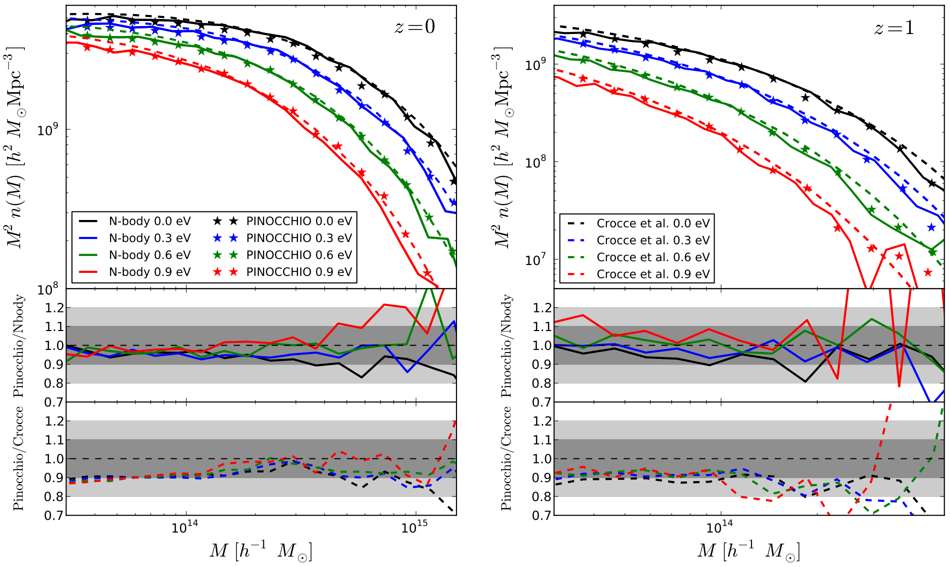

Fig. 4.2: *Top panel*: mass function for different values of the neutrino mass. Solid lines show the result of N-body simulations, while dashed lines show the PINOCCHIO predictions. *Middle panel*: ratio of the PINOCCHIO mass function to the one measured from N–body simulations. *Bottom panel*: ratio of the PINOCCHIO mass function to the fit of Crocce et al. (2010). From Rizzo et al. (2017).

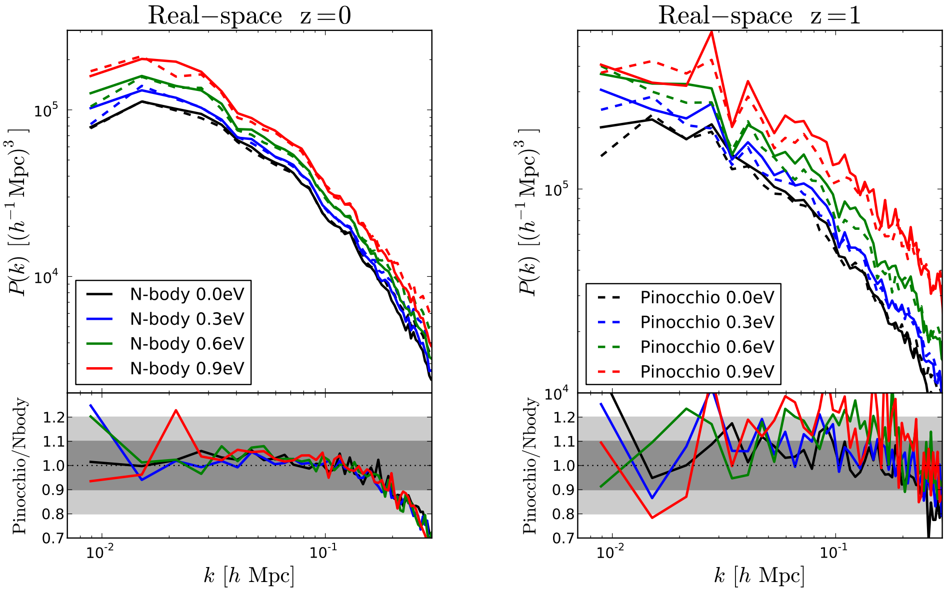

Fig. 4.3: *Top panel*: halo power spectrum in real space at redshift $z = 0$ (left) and $z = 1$ (right), with different values of the neutrino mass. *Bottom panel*: ratio of the PINOCCHIO real–space halo power spectrum to the one measured from N–body simulations (Rizzo et al., 2017).

4.2.1 Testing the massive neutrino approach in MG

The presence of a scale-dependent growth rate is also a feature of modified gravity models, though in this case it is introduced by the coupling of the additional MG degree of freedom to the matter field. As a first approach to extend the computation of Lagrangian displacements to MG we test a similar technique to the one adopted in the case of massive neutrinos, described in the previous section. In this case, the linear power spectrum is computed with EFTCAMB (Hu et al., 2015) for the case of $n = 1$ Hu-Sawicki with $f_{R0} = -10^{-4}$. From these linear power spectra we compute the linear growth rate adopting eq. 4.3, while the second order growth rate is computed with eq. 4.4. To test the validity of our approach, we compare to the DUSTGRAIN-pathfinder simulations (Giocoli et al. 2018, see §5.4.1), ran with the same MG model considered in this work. Technical details on how we construct the halo catalog from the Lagrangian displacement field are described in §5.4. We compare the halo power spectrum to the one measured from simulations: in Fig. 4.4 I show the ratio of the halo power spectrum constructed from LPT displacements to the one measured from the N-body simulations for three different redshifts.

The first order of LPT (Zel'dovich approximation, green line) exhibit a similar performance as both in the ΛCDM and in the massive neutrino cases, being able to recover the halo power spectrum of simulations within 5% up to scales $k \sim 0.1\,h$ Mpc^{-1}. On the other hand, the second order (2LPT, purple line) shows a significant deviation and does not represent an improvement over the linear order. Such result suggests that the approach of Rizzo et al. (2017) is not suitable in the case of MG. This is due to the fact that the scale-dependence of $D_2(k,t)$ is not properly captured by the $D_1^2(k,t)$ term of eq. 4.4. I describe a suitable method to compute the second-order growth rate in MG in §5, showing the improved agreement to N-body simulations when displacements are evaluated with the proper $D_2(k,t)$ (Moretti et al., 2019).

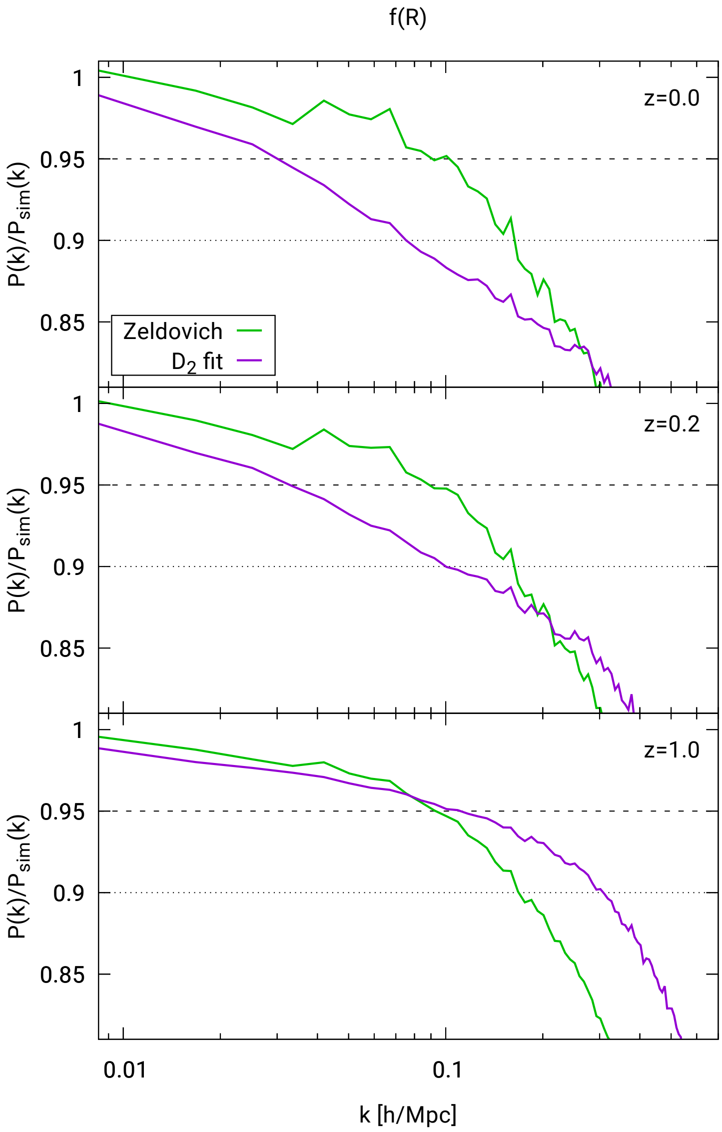

Fig. 4.4: Ratio of the halo power spectrum constructed from LPT displacements to the one measured from the DUSTGRAIN-pathfinder simulations for three different redshifts ($z = 0$,0.2,1, top to bottom). $D_1(k, a)$ is computed as ratio of linear power spectra generated with EFTCAMB and used to compute the first order of LPT (green line), while D_2 is computed from eq. 4.4, and used to compute the second order (2LPT, purple line).

4.3 Testing PINOCCHIO with WDM

One of the possible extensions of the standard cosmological scenario is to consider Warm Dark Matter (WDM) as an alternative to CDM. WDM could solve several issues appearing from the comparison between CDM N-body simulations and observations, such as the so-called "missing satellite problem" (Primack, 2009), the "too big to fail" problem (Boylan-Kolchin et al., 2011), or the "cusp-core problem" (Bullock, 2010); potential candidates include the sterile neutrino (Dodelson & Widrow, 1994; Shaposhnikov & Tkachev, 2006) and the gravitino (Moroi et al., 1993; Gorbunov et al., 2008). In general, DM particles can be classified according to their velocity dispersion. The latter defines a free-streaming length, below which overdensity fluctuations are erased, as in the massive neutrino case (which can in fact be classified as hot dark matter). This results in a suppression in the growth of structures below some cutoff scale, smaller than those typically affected by massive neutrinos, with an associated effect on the abundance of collapsed structures. In particular, the abundance of high mass halos is predicted to be suppressed with respect to a standard CDM scenario, as can be seen in Fig. 4.5 (Angulo et al., 2013).

Part of my PhD project was devoted to testing a possible way of including WDM in PINOCCHIO. The general approach to generate initial conditions for N-body simulations with WDM is to use a scale dependent transfer function applied to a linear power spectrum, in order to take into account the suppression of small scale fluctuations (Bode et al., 2001):

$$T_{\mathrm{WDM}}(k) = T_{\mathrm{CDM}}(k)\left[1+(\alpha k)^2\right]^{-5} , \tag{4.5}$$

where α depends on the WDM particle mass. Applying the transfer function of eq. 4.5 results in a truncated power spectrum, with a cut-off at the free streaming scale. Following the same approach, we input a truncated power spectrum in PINOCCHIO, and compute the mass function. The result is shown in Fig. 4.6 for $m_{\mathrm{WDM}} = 250$ eV (green line): while the suppression of the mass function on the low-mass end is similar to the one of Fig. 4.5, a significant loss of halos is present also at $M_h \geq 10^{12} - 10^{13}\ M_\odot\ h^{-1}$, where the WDM mass function should be suppressed by less than 10% respect to the CDM one.

To better investigate the problem, I perform several tests. A similar effect

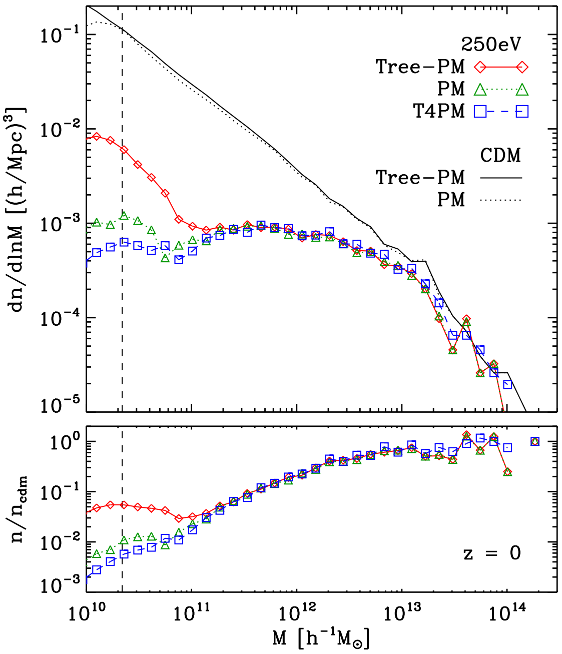

Fig. 4.5: Halo mass function in presence of WDM, computed from N–body simulations (red, green and blue lines). WDM free-streaming results in a suppression of the mass function on the low-mass end, while the abundance of high-mass halos is roughly the same as in CDM (black lines). From Angulo et al. (2013).

to using a truncated power spectrum can in principle be obtained by changing the minimum scale on which the smoothing is performed. As described in sec. 4.1, the code performs a number of smoothing for different scales R_{smooth}, with the last smoothing set to $R_{\mathrm{min}} = 0$, followed by the computation of collapse times for all grid points and for each smoothing. Changing the value of R_{min} amounts to washing out overdensities on scales smaller than R_{min}, in a way that is equivalent to having a truncated power spectrum.

The first test was targeted at assessing the stability of the code when changing the number of smoothing radii: I ran the code several times with all parameters fixed, but with different number of smoothing radii. The results are shown in fig. 4.7, where I plot the mass function obtained for the different smoothing schemes considered: $N_{\mathrm{smooth}} = 10$ (red line), $N_{\mathrm{smooth}} = 30$ (purple line) and $N_{\mathrm{smooth}} = 100$ (blue line). Dashed lines represent runs where the last smoothing was removed (hence $R_{\mathrm{min}} > 0$). In black I also

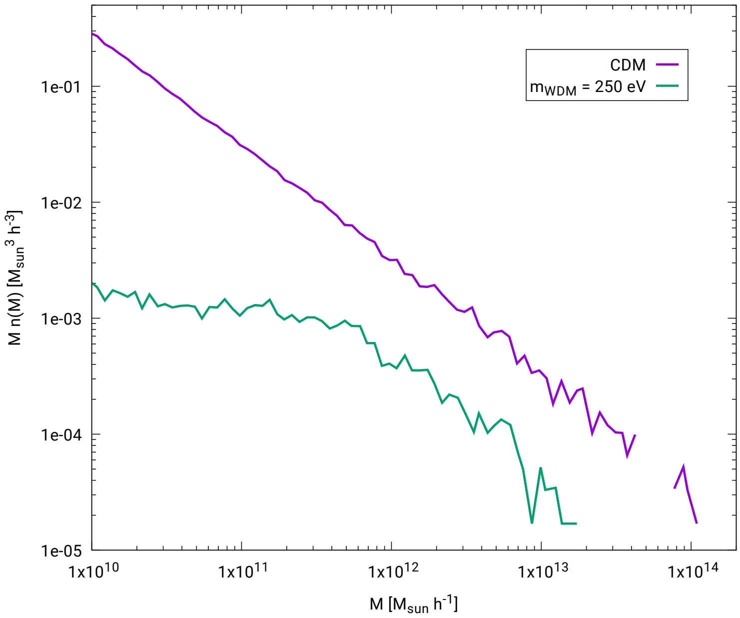

Fig. 4.6: Halo mass function computed with PINOCCHIO for $m_{\text{WDM}} = 250$ eV (green line) and CDM (purple) line, for a box with $L = 80$ Mpc h^{-1}, $N_{part} = 1024^3$. The effect of WDM is included using a truncated power spectrum, computed with the transfer function of eq. 4.5. The purple line is the CDM mass function. Courtesy of P. Monaco

show the Watson fit for the mass function (Watson et al., 2013), on which PINOCCHIO is calibrated. The result shows the code is stable in all cases considered, yielding similar results for the mass function.

I then change the minimum smoothing radius in the range $0 \leq R_{\text{min}} \leq d$, where d is the interparticle distance, and compare the obtained mass functions. The results are shown in Fig. 4.8 for different values of R_{min}, as stated in the legend: while runs with R_{min} set to a fraction of the interparticle distance show no significant difference in the mass function, the run with $R_{\text{min}} = d$ exhibits a similar behavior to the one displayed in Fig. 4.6, with a suppression of halos for all masses. In Fig. 4.9 I plot the results obtained for $0 \leq R_{\text{min}} \leq 2.5d$, showing how the suppression of the high-mass end of the halo mass function gets more significant as the value of R_{min} increases.

This result shows the presence of a numerical issue, resulting in the inability of the code to reproduce the high-mass end of the WDM mass function. To gain more insight, I performed an object-by-object analysis. Particles in PINOCCHIO are tagged with an ID and a halo-ID: particles

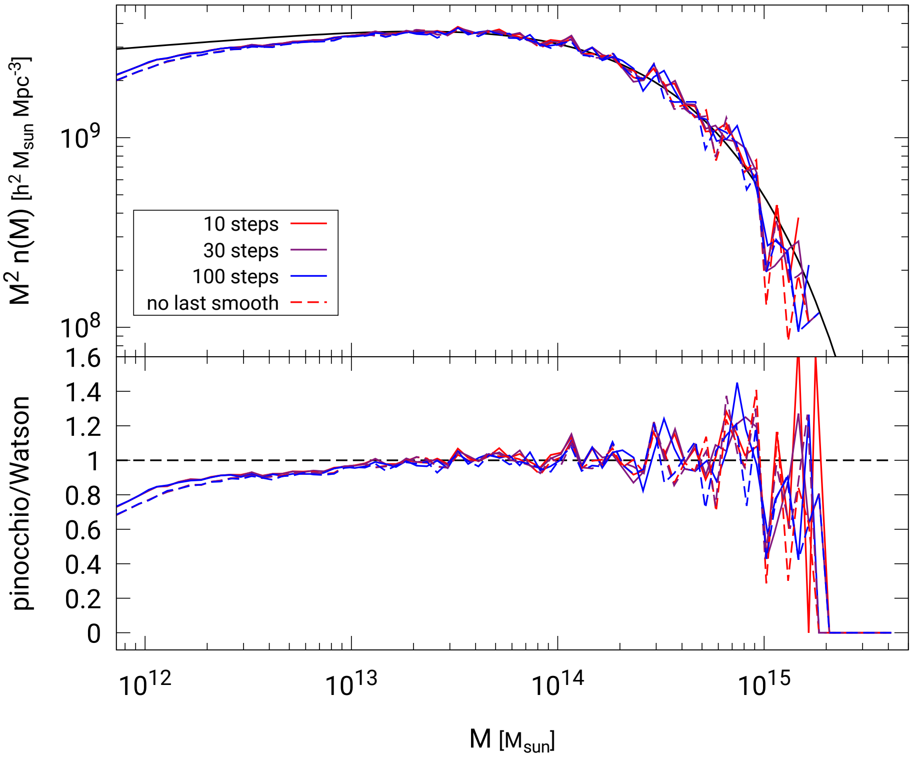

Fig. 4.7: *Top panel*: mass function computed for different number (100 in blue, 30 in purple, 10 in red) of smoothing radii, with the last smoothing set to $R_{\min} = 0$ (solid lines) or removed (dashed lines). In black is shown the fit of Watson et al. (2013). *Bottom panel*: ratio of the different mass functions to the fit.

belonging to the same halo all have the same halo-ID, corresponding to the ID of the first particle to collapse. For each halo, I compare the results of two realizations with different minimum smoothing radii $R_{\min} = 0$ and $R_{\min} = d$, d being the interparticle distance. After choosing one halo in the $R_{\min} = 0$ simulation, I identified the corresponding halo (halo with the same ID) in the $R_{\min} = d$ simulation. Particles that are in the halo in the first simulation can be: (i) in the same halo, (ii) in a different halo, (iii) in a filament or (iv) not collapsed. Fig. 4.10 show the result of such analysis: while most particle belong to the same halo in both simulations (light blue curve), a significant fraction (∼20%) of particles that are in halo in the $R_{\min} = 0$ simulation is tagged as filament particles (i.e. collapsed but not accreted) in the $R_{\min} = d$

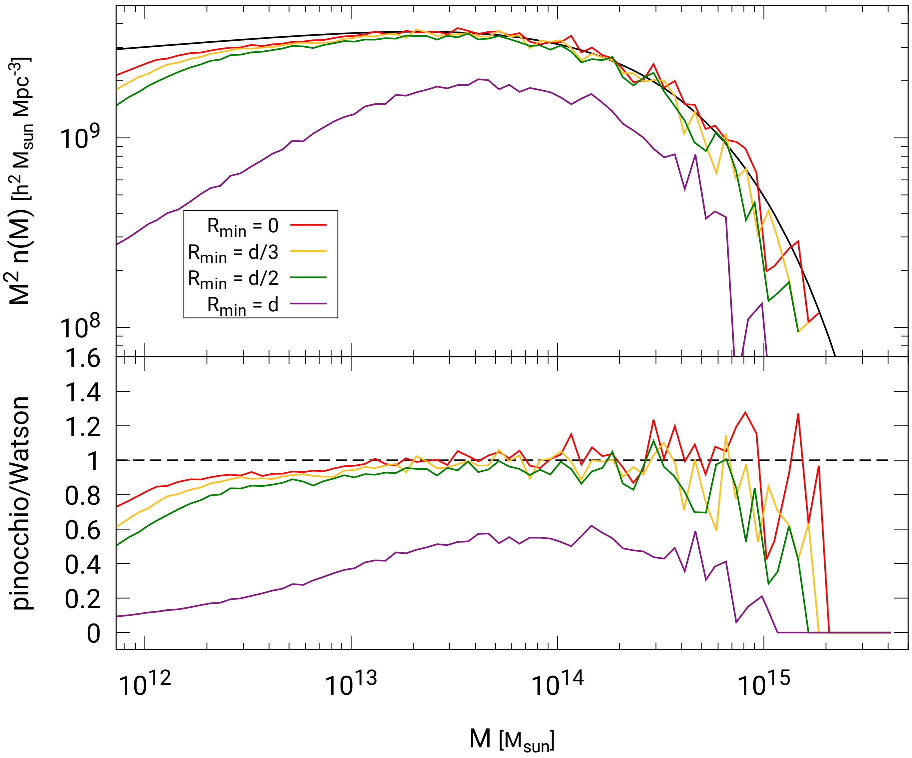

Fig. 4.8: Top panel: mass function computed with different values for the last smoothing radius $R_{\rm min}$ ($R_{\rm min} = 0$ in red, $R_{\rm min} = d/3$ in yellow, $R_{\rm min} = d/2$ in green and $R_{\rm min} = d$ in purple). Black line shows the fit from Watson et al. (2013). Bottom panel: ratio of the different mass functions to the analytic fit.

simulation.

4.3.1 Summary and discussion

Using a truncated power spectrum as input in PINOCCHIO to include the effects of WDM showed an inability to properly reproduce the halo mass function (Fig. 4.6), with a significant loss of high-mass halos with respect to the results of N-body simulations. In PINOCCHIO, changing the last smoothing radius $R_{\rm min}$ is equivalent to using a truncated power spectrum. I run the code with different smoothing schemes, with the following results:

- The first test (Fig. 4.7) was aimed at assessing the numerical stability of the code when changing the number of smoothing radii, and confirmed

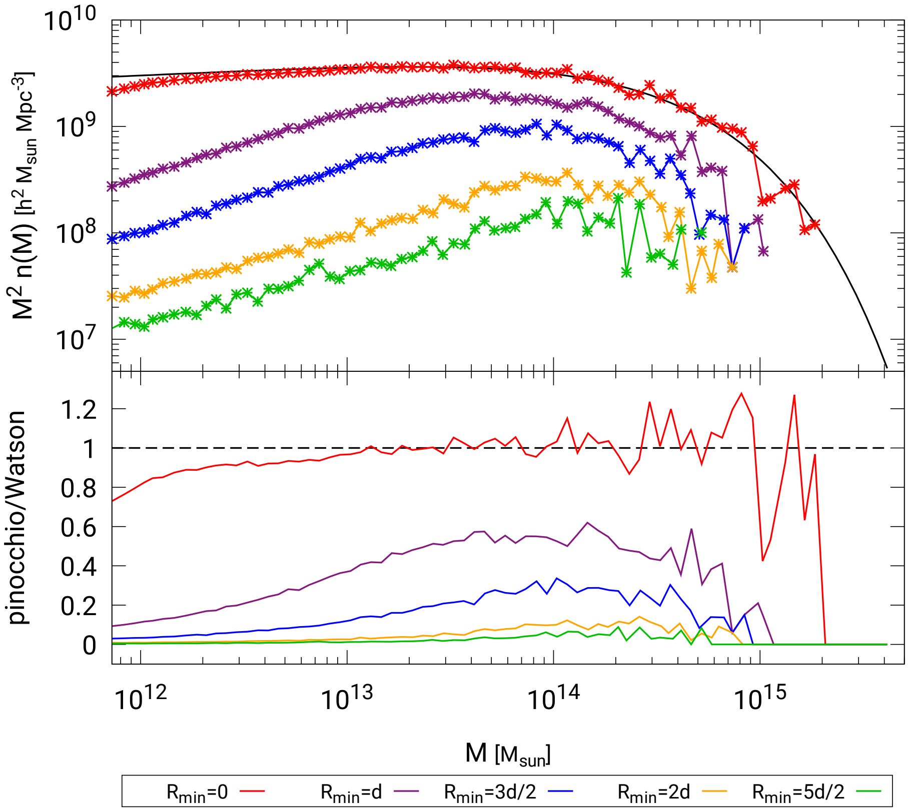

Fig. 4.9: Top panel: mass function computed with different values for the last smoothing radius $R_{\min}$ ($R_{\min} = 0$ in red, $R_{\min} = d$ in purple, $R_{\min} = 3d/2$ in blue, $R_{\min} = 2d$ in yellow and $R_{\min} = 5d/2$ in green). Black line shows the fit from Watson et al. (2013). Bottom panel: ratio of the different mass functions to the analytic fit.

that a different N_{smooth} does not have significant effects on the halo mass function;

- The second test (Fig. 4.8 and 4.9) showed that, when considering $R_{\min} = d$ (blue line of Fig. 4.8), the mass function is significantly suppressed on all mass-scales. The effect is more dramatic if the last smoothing is set to even larger values of $R_{\min}$, as shown in Fig. 4.9. This effect is not noticeable in the $R_{\min} > 0$ cases of Fig. 4.7 (dashed lines), because the last smoothing is always performed on scales that are a small fraction of the inter-particle distance;

- I perform an object-by-object analysis, comparing halo-by-halo the two realizations with $R_{\min} = 0$ and $R_{\min} = d$. The results (Fig. 4.10)

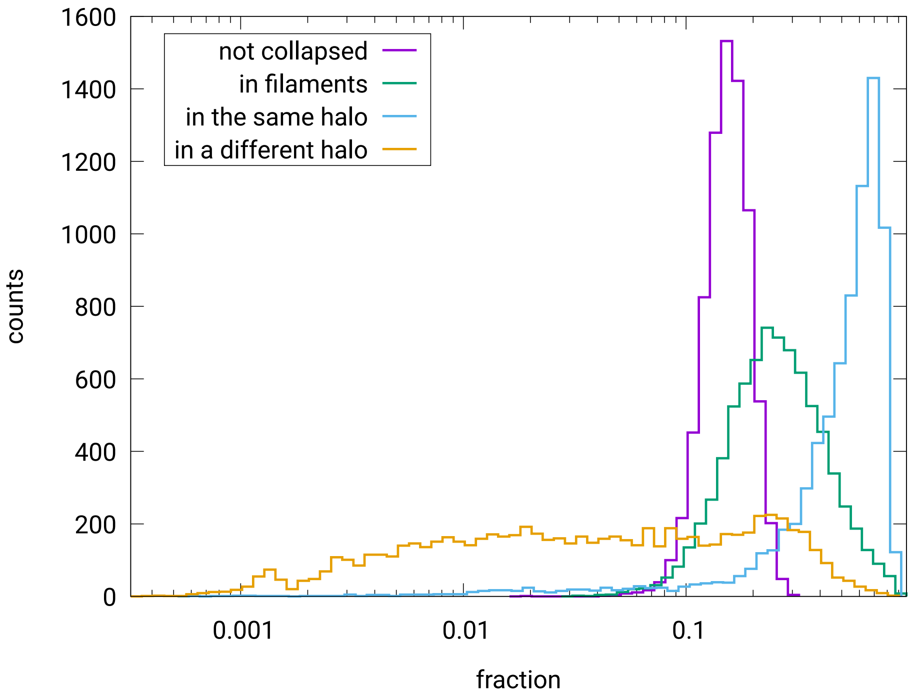

Fig. 4.10: Comparison between two realizations with different minimum smoothing, $R_{\rm min} = 0$ and $R_{\rm min} = d$, with d the interparticle distance. For each halo in the $R_{\rm min} = 0$ simulation, I check whether the particles in the $R_{\rm min} = d$ simulation are in the same halo (light blue curve), in a different halo (orange curve), not collapsed (purple curve), or filament particles (green curve). A significant fraction of particles are tagged as filament, highlighting an issue in the calibration of the accretion distance.

showed that while most ($\sim$ 70%) particles are in the same halo in both simulations, a significant fraction of particles ($\geq$ 10%) that are in halos in the $R_{\rm min} = 0$ simulation are tagged as filaments in the $R_{\rm min} = d$ simulation.

The last result highlights an issue in the grouping part of the algorithm, in particular at the level of the calibration of the parameters that determine the distance threshold for accretion. This results in a higher fraction of filament particles, and a reduction in the abundance of high-mass halos. Since the calibration adopted is cosmology independent (eq. 4.1), it should hold also in the case of WDM cosmologies. Likely, the parameterization adopted for the threshold distance is wrong, though the effects are not evident in the case of standard CDM. The process of calibration is however quite cumbersome, since it involves identifying a proper parameterization for the threshold distance $d_{\rm thr}$ as well as performing several runs of the code to fit the parameters (see Appendix A of Munari et al. 2017b). Moreover, the code is currently undergoing major developments with the purpose of extending it to MG models, hence we leave the re-calibration for a future work.

Chapter 5

Lagrangian Perturbation theory with Modified Gravity

The first step towards an extension of PINOCCHIO to MG models is a proper reformulation of LPT, that must include the scale-dependence in the growth of structures induced by MG. This is a potential problem for the LPT approach, since it makes the factorization of the time evolution to compute displacements unfeasible, and both the theoretical and computational treatment of LPT with modified gravity become more involved. Additionally, for our purposes we need to be at least second-order in the perturbative treatment to be sufficiently accurate in the description of mildly-NL scales. While the computation of the linear order can easily be extended, evaluating the second-order displacement field is more complicated. A full theoretical description of LPT (up to third order) in the framework of scalar-tensor modified gravity theories was recently proposed in Aviles & Cervantes-Cota (2017), while Valogiannis & Bean (2017); Winther et al. (2017) implement different numerical approaches to compute cosmological quantities in this framework.

In this chapter I describe a new numerical method, based on FFTs, developed to compute the source term of the differential equation for 2LPT displacements when modified gravity theories are considered. In what follows, I will mostly focus on Hu-Sawicki $f(R)$ models (§3.5.1); the method is however quite general and can easily be extended to different MG models. The results presented here are described in a paper, submitted for review to MNRAS (Moretti et al., 2019).

5.1 Theoretical framework

I focus on MG models that reproduce the ΛCDM expansion history on large scales, while on intermediate scales they include a fifth force that is due to a new scalar degree of freedom. Solar system constraints are met by means of a screening mechanism (§3.3). The fifth force caused by the gravity modification introduces mode coupling even at the linear level; additionally, in order to properly describe non-linear scales, the Klein-Gordon equation for the scalar field must be solved. Following the approach of Koyama et al. (2009), the modified Poisson equation and the Klein-Gordon equation can be written as:

$$\frac{1}{a^2}\nabla^2\Phi = 4\pi G\bar{\rho}\delta - \frac{1}{2a^2}\nabla^2\varphi \ , \tag{5.1}$$

$$(3+2\omega)\frac{1}{a^2}\nabla^2\varphi = -8\pi G\bar{\rho}\delta + \mathrm{NL} \ , \tag{5.2}$$

where Φ is the gravitational potential, $\bar{\rho}$ is the background matter density, φ is the scalar field that encodes the modification of gravity, ω is the Brans-Dicke (coupling) parameter, and *NL* are possible non-linearities that might arise in the Lagrangian, due to the coupling of the scalar field to matter or self-coupling. Going to Fourier space, eq. 5.2 can be written as:

$$(3+\omega)\frac{k^2}{a^2}\varphi_k = 8\pi G\bar{\rho}\delta_k - \mathcal{I}(\varphi_k) \ . \tag{5.3}$$

The term $\mathcal{I}(\varphi_k)$ is the scalar field self–interaction, that is related to the screening mechanism responsible of recovering GR on small scales. It can be expanded as $\mathcal{I}(\varphi_k) = M_1(k,a)\varphi_k + \delta\mathcal{I}(\varphi_k)$, with

$$\begin{aligned}\delta\mathcal{I}(\varphi_k) = \frac{1}{2}\int \frac{\mathrm{d}^3k_1\mathrm{d}^3k_2}{(2\pi)^3}\delta_D(\vec{k}-\vec{k}_{12})M_2(\vec{k}_1,\vec{k}_2,a)& \\ \times\ \varphi(\vec{k}_1,a)\varphi(\vec{k}_2,a) + \mathcal{O}(\varphi_k^3) \ ,&\end{aligned} \tag{5.4}$$

where the M_i functions are in general scale and time dependent and their functional form depends on the particular model considered. I now focus on $f(R)$ models (§3.5), although the method is quite general, and can be applied to other scalar-tensor theories, provided that the MG potential can be split in a background value plus perturbations, and the perturbations can be Taylor expanded (see eq. 5.7 below).

Taking the trace of the modified field equations 3.7 for $f(R)$, one obtains:

$$3\Box f_R = R(1-f_R) + 2f - 8\pi G\rho \ , \tag{5.5}$$

where $f_R = \mathrm{d}f(R)/\mathrm{d}R$. Equivalently, one can split f_R and R in background quantities plus perturbations δf_R and δR. In the quasi–static approximation one can write:

$$\frac{3}{a^2}\nabla^2\delta f_R = -8\pi G\bar{\rho}\delta + \delta R \ , \tag{5.6}$$

which is nothing but the Klein-Gordon equation for a scalar field with potential δR and Brans-Dicke parameter $\omega = 0$. The potential can be expanded as

$$\delta R = \sum_k \frac{1}{k!}M_k(\delta f_R)^k \qquad , \qquad M_k = \left.\frac{\mathrm{d}^k R(f_R)}{\mathrm{d}f_R^k}\right|_{f_R=\bar{f}_R} \tag{5.7}$$

For $f(R)$ gravity the coefficients M_k only depend on time; this is an important feature for the approach we propose in this work (described in §3.5). In the following treatment I consider Hu-Sawicki $f(R)$ (§3.5.1), where the function $f(R)$ is the one of eq. 3.13. By fixing $n = 1$, the M_k coefficients can be written as:

$$\begin{aligned} M_1(a) &= \frac{3}{2}\frac{H_0^2}{|f_{R0}|}\frac{(\Omega_{m,0}a^{-3}+4\Omega_\Lambda)^3}{(\Omega_{m,0}+4\Omega_\Lambda)^2} \ , \\ M_2(a) &= \frac{9}{4}\frac{H_0^2}{|f_{R0}|^2}\frac{(\Omega_{m,0}a^{-3}+4\Omega_\Lambda)^5}{(\Omega_{m,0}+4\Omega_\Lambda)^4} \ . \end{aligned} \tag{5.8}$$

Substituting eq. 5.3 in the Fourier space version of the modified Poisson equation 5.1, and then combining with the equation of motion for the particle, one can write the evolution equation for the first order displacement field in Fourier space as:

$$a^2H^2(\hat{T} - 4\pi G\bar{\rho}\mu(k,a))\ \mathrm{FT}[\phi^{(1)}_{,ii}](\vec{k},a) = 0 \ , \tag{5.9}$$

where FT is the Fourier transform operator, $\hat{T} = \mathrm{d}^2/\mathrm{d}a^2 + 3/a + H'(a)/H(a)\times \mathrm{d}/\mathrm{d}a$ ($'$ denoting derivation with respect to the scale factor), and

$$\mu(k,a) = 1 + \frac{1}{3}\frac{k^2/a^2}{k^2/a^2 + m^2(a)} \ . \tag{5.10}$$

The $m^2(a)$ function represents the mass of the scalar field, and is related to $M_1(a)$ by $M_1(a) = 3m^2(a)$. It is no longer possible to separate time and space, since the operator acting on the first order displacement potential is no longer time–dependent only, due to the presence of $\mu(k, a)$ in eq. 5.9. Nonetheless, we can separate time for each Fourier mode, so that:

$$\mathrm{FT}[\phi^{(1)}_{,ii}](\vec{k}, a) = D_1(k, a)\ \mathrm{FT}[\phi^{(1)}_{,ii}](\vec{k}, a_{in})\ , \tag{5.11}$$

where $D_1(k, a)$ is the solution of:

$$a^2H^2(\hat{T} - 4\pi G\bar{\rho}\mu(k, a))D_1(k, a) = 0\ . \tag{5.12}$$

It is worth noting that the first order growth factor is now scale dependent, due to the presence of the $\mu(k, a)$ function in the differential equation. However, the scale dependence is fully enclosed in μ, and is only related to the modulus of k. The linear growth factor can then be computed by fixing a value for k and solving the differential equation, repeating for a set of k-values and finally interpolating to obtain the function at any k. I numerically solve eq. 5.12 with a standard Runge-Kutta algorithm, with initial conditions for $D_1(k, a)$ set to the growing mode for a matter dominated (Einstein–de Sitter) Universe, namely $D_1(a_{in}) = a_{in}$ and $D'_1(a)|_{a=a_{in}} = 1$. The resulting linear growth factor is then normalized so that $D_1(k = 0, a = 1) = 1$. The result is shown in Fig. 5.1, where I plot the ratio between the MG linear growth factor D_{MG} and the ΛCDM one in the case of $n = 1$ Hu-Sawicki $f(R)$, for three different values of the f_{R0} parameter and two different redshifts.

Once again, the initial first–order displacement field can be determined from the initial density field, and its evolution computed my multiplying it by $D_1(k, a)$. However, when going to second order this kind of separation cannot be done, since the second order growth factor depends on three wave-numbers k, k_1 and k_2 and on the dot product $\vec{k}_1 \cdot \vec{k}_2$. The second order displacement field can be written (in Fourier space) as an integral over k_1 and k_2:

$$\mathrm{FT}[\phi^{(2)}_{,ii}](\vec{k}, a) = \int \frac{\mathrm{d}^3k_1\mathrm{d}^3k_2}{(2\pi)^3}\delta_D(\vec{k} - \vec{k}_{12})D_2(k, k_1, k_2, a)\delta_1\delta_2\ , \tag{5.13}$$

where δ_D is the Dirac delta, $\vec{k}_{12} = \vec{k}_1 + \vec{k}_2$, $\delta_i = \delta(\vec{k}_i)$ is the linear density contrast evaluated at present time and $D_2(k, k_1, k_2, a)$ is the scale-dependent

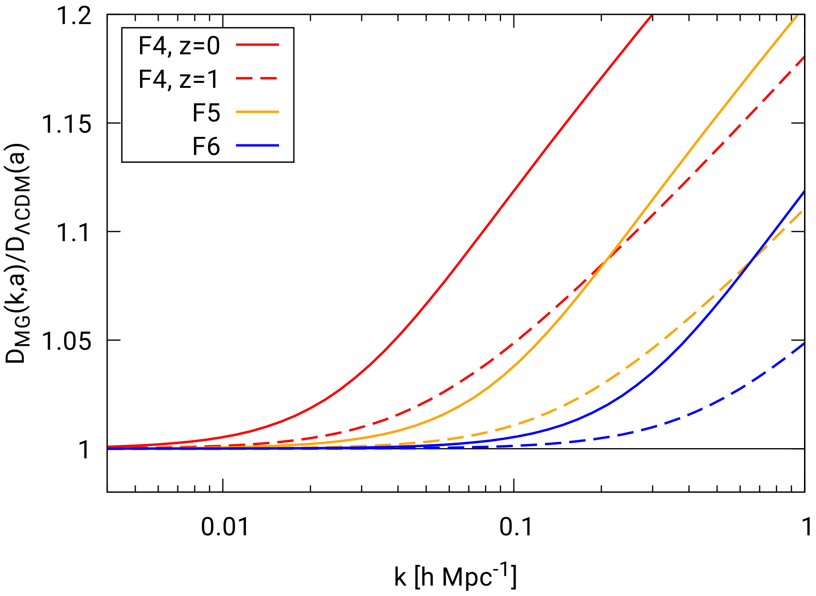

Fig. 5.1: Solution to eq. 5.12 for Hu–Sawicki $f(R)$ with n=1 normalized to the ΛCDM linear growing mode for three different values of the f_{R0} parameter ($f_{R0} = -10^{-4}$ in red, labeled as F4; $f_{R0} = -10^{-5}$ in orange, labeled as F5; $f_{R0} = -10^{-6}$ in blue, labeled as F6), shown for $z = 0$ (solid line) and $z = 1$ (dashed line).

second order growth rate obtained by solving:

$$\begin{aligned}
&a^2H^2(a)\left[\hat{T} - 4\pi G\bar{\rho}\mu(k)\right] D_2(k, k_1, k_2, a)\\
&\qquad = 4\pi G\bar{\rho} D_1(k_1, a) D_1(k_2, a)\Bigg\{\mu(k)+\\
&\qquad - \frac{(\vec{k_1}\cdot\vec{k_2})^2}{k_1^2k_2^2}\left[\mu(k_1)+\mu(k_2)-\mu(k)\right]+\\
&\qquad + \frac{m^2(a)}{\Pi(k)}\Bigg[2\frac{(\vec{k_1}\cdot\vec{k_2})^2}{k_1^2k_2^2}\left(\mu(k_1)+\mu(k_2)-2\right)+\\
&\qquad \frac{\vec{k_1}\cdot\vec{k_2}}{k_1^2}\left(\mu(k_1)-1\right)+\frac{\vec{k_1}\cdot\vec{k_2}}{k_2^2}\left(\mu(k_2)-1\right)\Bigg]+\\
&\qquad - \frac{2}{27}4\pi G\bar{\rho}\frac{k^2}{a^2}\frac{M_2(a)}{\Pi(k)\Pi(k_1)\Pi(k_2)}\Bigg\}.
\end{aligned} \tag{5.14}$$

A full derivation of this last equation can be found in Aviles & Cervantes-Cota

(2017). For the sake of simplicity, I dropped write the time dependence of $\mu(k, a)$ and $\Pi(k, a)$ in eq. 5.14.

The presence of the Dirac delta in eq. 5.13 requires that $\vec{k} = \vec{k}_1 + \vec{k}_2$, so that the integral runs over all possible triangle configurations formed by $\vec{k}_1$, $\vec{k}_2$ and $\vec{k}$ in Fourier space. Because of this, implementing the full solution for the second order displacements would require to solve a different equation for each wavenumber $\vec{k}$, whose source term includes a 9-dimensional integral. While not unfeasible in principle, this computation would be very time consuming, making an approximate method based on 2LPT a poor alternative to full N-body simulations.

One possible alternative, already explored by Winther et al. 2017, is to find an approximation for $D_2(k, a)$, in order to achieve an effective factorization of the second order-potential into the same space part as in GR (to be computed with Fast Fourier Transforms) and an effective k-dependent growth rate:

$$\phi^{(2)}(\vec{k}, a) = D_2(k, a)\phi^{(2)}(\vec{k}, a_{in}) \tag{5.15}$$

In particular, one can choose a triangle configuration for $\vec{k}$, $\vec{k}_1$ and $\vec{k}_2$, solve eq. 5.14 to find $D_2(k, k_1, k_2, a)$ and then compute the displacement field in the standard way, with $\phi^{(2)}(\vec{k}, a_{in})$ being the Fourier-space version of the initial second order displacement field (term in square brackets on the right-hand-side of eq. 2.26).

5.2 Source term

As discussed in the previous section, the goal is to find an approximation for the second-order growth rate which allows to readily compute the second order displacement field. Moreover, we want to quantify the deviation of the approximation from the full solution. The approach is to compute the full source term of the differential equation for the 2LPT displacement field by taking advantage of FFTs, and then compare it to analytical expressions for different triangle configurations, in order to find the one that best matches the full source term. Next, I numerically solve the differential equation for D_2 for the chosen triangle configuration, and use it to approximate the evolution of the displacement field.

The second order displacement field in general, scalar-tensor theories of gravity (where the scalar field potential can be expanded as in eq. 5.7) is the solution of eq. 5.13. The growth factor can be computed by solving eq. 5.14. This equation reduces to the standard, ΛCDM one for $\mu(k,a) = 1$. The dependence on closed triangles in Fourier space is related to the presence of derivatives of the first-order displacement field as well as the M_k functions, which can in principle bear a scale dependence. In the special case of $f(R)$ gravity theories, the M_k functions only depend on time, so they can be taken out of the integral we need to solve to compute $\phi^{(2)}(\vec{k},a)$. Eq. 5.13 can then be written by expressing the Fourier-space integrals as Fourier transforms of local, non-linear functions in real space. It is then possible to take advantage of FFTs to compute the full source term of the differential equation. The validity of this approach is not limited to $f(R)$ models but extends to all theories where the MG scalar potential can be expanded into scale independent coefficients. The full equation for 2LPT displacements can be written as:

$$a^2H^2(\hat{T} - 4\pi G\bar{\rho}\mu(k,a))\ \mathrm{FT}[\phi^{(2)}_{,ii}](\vec{k},a) = S_1 + S_2 + S_3 + S_4\ , \tag{5.16}$$

where

$$S_1 = 4\pi G\bar{\rho}\ \mathrm{FT}\left[\phi^{(1)}_{,ij}\ \mathrm{FT}^{-1}\left[\mu(k,a)\ \mathrm{FT}[\phi^{(1)}_{,ji}]\right]\right]\ , \tag{5.17}$$

$$S_2 = -2\pi G\bar{\rho}\mu(k,a)\ \mathrm{FT}\left[\phi^{(1)}_{,ii}\phi^{(1)}_{,jj} - \phi^{(1)}_{,ij}\phi^{(1)}_{,ji}\right]\ , \tag{5.18}$$

$$S_3 = \left(\frac{8\pi G\bar{\rho}}{3}\right)^2 \frac{M_2(a)}{12}\frac{k^2/a^2}{\Pi(k,a)}\ \mathrm{FT}\left[\left(\mathrm{FT}^{-1}\left[\frac{\delta^{(1)}_k}{\Pi(k,a)}\right]\right)^2\right]\ , \tag{5.19}$$

$$\begin{aligned} S_4 = -\frac{8\pi G\bar{\rho}}{3}\frac{m^2(a)}{2a^2}\frac{1}{\Pi(k,a)}\ \mathrm{FT}\Bigg[2\phi^{(1)}_{,ij}\left(\mathrm{FT}^{-1}\left[\frac{\delta^{(1)}_k}{\Pi(k,a)}\right]\right)_{,ij} \\ +\phi^{(1)}_{,iij}\left(\mathrm{FT}^{-1}\left[\frac{\delta^{(1)}_k}{\Pi(k,a)}\right]\right)_{,j}\Bigg]\ . \end{aligned} \tag{5.20}$$

Here $\Pi(k,a) = k^2/a^2 + m^2(a)$ and the $\phi^{(1)}$, $\delta^{(1)}$ fields are evolved with the linear scale–dependent growth factor $D_1(k,a)$. The S_1 and S_2 terms come from keeping second order terms in the Poisson equation and the equation of motion. The S_3 term is related to the second–order scalar field self–interaction (NL in eq. 5.2). Finally, the S_4 term (first introduced by Aviles & Cervantes-Cota 2017), is a geometric term, due to the fact that we are performing Fourier transforms in Lagrangian Fourier space, not Eulerian.

5.3 Approximations for D2

The method adopted is the following: I generate a linear density field on a regular grid, compute the first order growth factor $D_1(k, a)$ by numerically solving eq. 5.12 and use it to evolve the field. Next I compute the S_i terms of eq. 5.16, going back and forth from Fourier space to configuration space to solve the integrals. I divide the source term by the equivalent quantity evaluated for ΛCDM. The result is a quantity that depends on $\vec{k}$, which I bin in a grid of k-values, computing its average and scatter within each bin. The aforementioned average is compared to the analytical expressions obtained using various triangle configurations in Fourier space. The result is shown in fig. 5.2, where I plot the computation of the full source term of the differential equation divided by its equivalent evaluated for a ΛCDM cosmology, at z=0. Solid lines represent the source term for boxes with different sizes ($200\ h^{-1}$ Mpc, $400\ h^{-1}$ Mpc, $600\ h^{-1}$ Mpc, $700\ h^{-1}$ Mpc) with a fixed resolution of 1 particle / h^{-1} Mpc. For each box I produce two realizations, one with MG and one with standard GR, both with the same initial conditions in order to have the same modes and sample variance. Afterwards I compute the ratio of the two, and compute average and standard deviation in bins of k. Dashed lines show the obtained 1σ standard deviation of the distribution of the points in each bin: this represents the scatter, due to the fact that the source term depends on the vector $\vec{k}$. This scatter provides a measure of how accurate a factorization in terms of a mildly k-dependent growth rate $D_2(k, t)$ is: even though the source term is not completely separable, the standard deviation is always below ~ 0.2, and goes to zero at large scales, as expected. Moreover, the average varies smoothly with k, and the standard deviation of the mean within each bin is not large, $\sigma/\sqrt{N} \sim 10^{-6}$ (with N the number of wave-modes in each bin). We can conclude that the average is measured with a good precision, and can be used to the purpose of finding an approximation to D_2.

To find an approximation for D_2 I compare the average ratio of source term to the same quantity, obtained analytically by adopting different triangle configurations: the result is shown in Fig. 5.3. The top panel shows the full source term (divided by the GR one) of Fig. 5.2 with black dots, and different

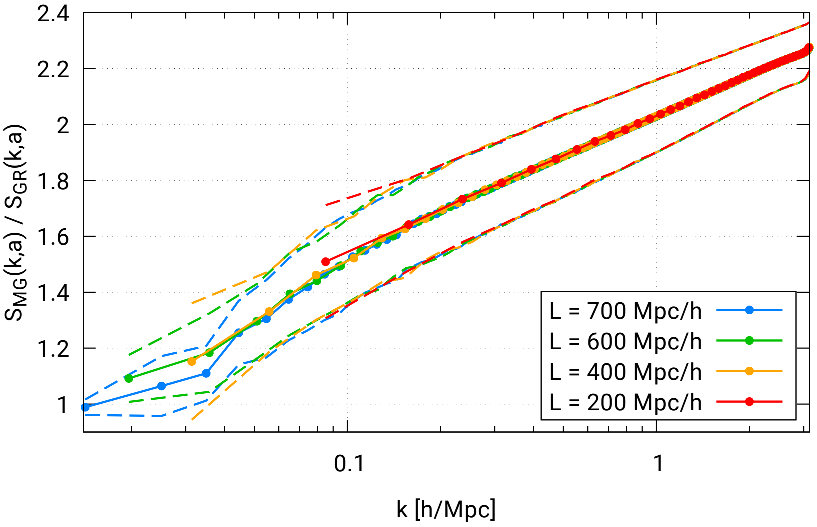

Fig. 5.2: Source term of the second–order displacement field differential equation with $f(R)$ modified gravity, normalized to the one in GR at $z = 0$. The modified gravity model is $n = 1$ Hu–Sawicki with $f_{R0} = -10^{-4}$. Different colors correspond to different box sizes, all with the same resolution of 1 particle per $\mathrm{Mpc}\ h^{-1}$. Each solid line is the result binned in k; dashed lines represent 1σ deviation from the mean value within each k–bin.

triangle configurations (solid lines), while in the bottom panel we show the percent difference between the full source term and different triangle configurations. First I compare to orthogonal ($k_1 = k_2$, $\theta = 90°$), equilateral ($k_1 = k_2, \theta = 60°$) and squeezed ($k_1 \simeq 0, k_2 = k$) configurations: the solution is very close to the orthogonal configuration, and above the equilateral one. These are both isosceles triangles with $k_1 = k_2$ and angle between $\vec{k}_1$ and $\vec{k}_2$ respectively $\theta = 90°$ and $\theta = 60°$. I therefore focus on isosceles triangles, keeping $k_1 = k_2$ and varying the angle. The best configuration is found to be the orthogonal one (red line in fig. 5.3, hereafter T1) and the one with $\theta = 80°$ (orange line in fig. 5.3, hereafter T2). Both T1 and T2 give results that are well within 1% with respect to the full source term, in particular for the mildly intermediate scales we are interested in describing with 2LPT. I also compare the source term to triangle configurations with different ratio k_1/k_2 and fixed angle $80°$, finding that increasing the ratio k_1/k_2 gives a worse match to the source term (green and magenta lines of fig. 5.3). The approximation proposed by Winther et al. 2017, is shown in blue in fig. 5.3, and corresponds to fixing $k_1 = k_2$, $\theta = 90°$ in eq. 5.14, but the first order growth rates in that equation are computed as $D_1(k)$ instead of $D_1(k_1)$, $D_1(k_2)$. This choice gives a slight overestimation of the source term, but the deviation is still within 5% up to $k \sim 0.2h$ Mpc^{-1}.

To understand the generality of this result, I perform the same computation for three different redshifts ($z = 0$, $z = 0.5$ and $z = 1$) and three different values of the f_{R0} parameter ($f_{R0} = -10^{-4}$, F4; $f_{R0} = -10^{-5}$, F5; $f_{R0} = -10^{-6}$, F6). The result is shown in fig. 5.4. The black dots represent the result of the ratio of source terms S_{MG}/S_{GR}, while the solid lines represent the two best triangles found for the F4, $z = 0$ case: T1 in red and T2 in green. It is worth noting that, when considering different redshifts and values of f_{R0}, the T1 configuration approximates better the full source term, and is therefore the one adopted to compute the approximate $D_2(k, a)$ when comparing to full N-body simulations.

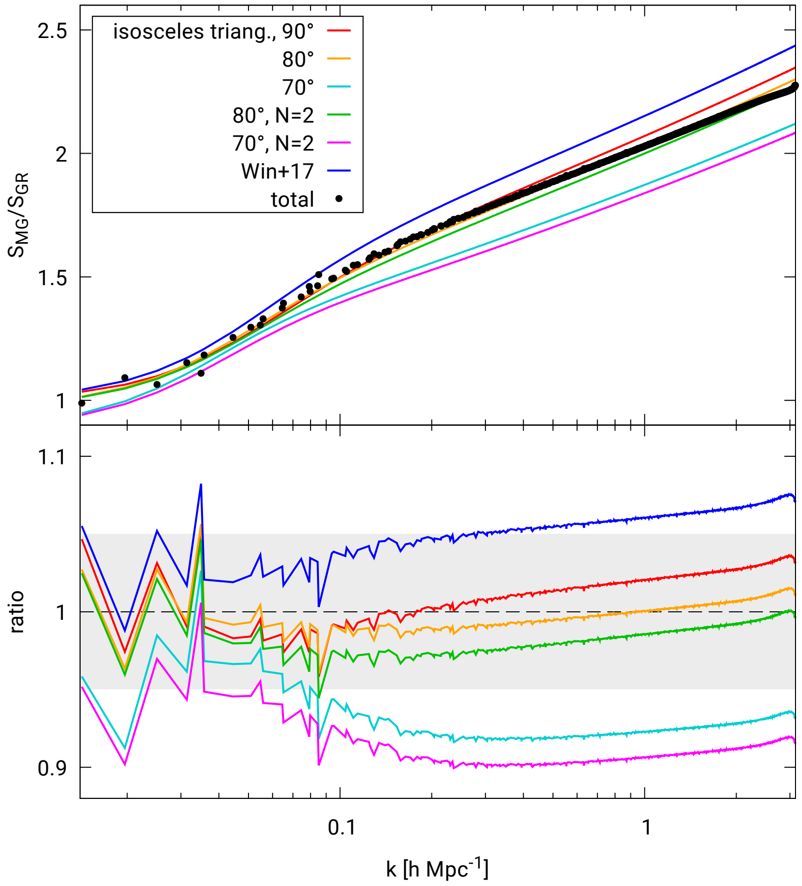

Fig. 5.3: Top panel: comparison of the full source term (black dots) to different triangle configurations at redshift $z = 0$. The red, orange and cyan lines represent isosceles triangles respectively with angle $90°$ (orthogonal configuration), $80°$ and $70°$ between k_1 and k_2. The green and magenta lines represent triangles with $k_1 = 2k_2$ and angle $80°$ and $70°$ respectively between k_1 and k_2. In blue is shown the approximation adopted in Winther et al. (2017). Bottom panel: ratio of the full solution to different configurations. The grey shaded area represents a 5% deviation from the full source term.

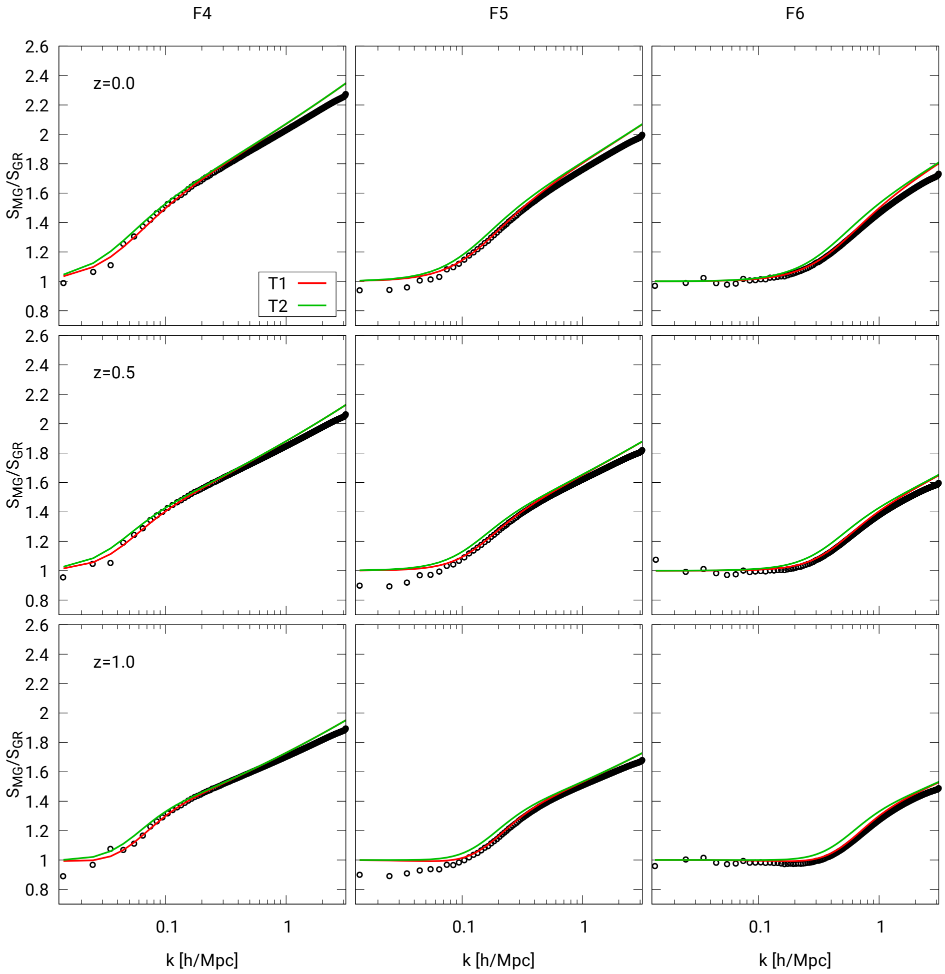

Fig. 5.4: Computation of the full source term (black dots), compared to the triangle configurations T1 (orthogonal: $k_1 = k_2$, $\theta = 90°$, red line) and T2 ($k_1 = k_2$, $\theta = 80°$, green line), for different redshifts and different values of the $\mathrm{f_{R0}}$ parameter. Top row is z=0, middle row z=0.5 and bottom row is for z=1. The left column is $\mathrm{f_{R0}} = -10^{-4}$, middle column $\mathrm{f_{R0}} = -10^{-5}$ and right column $\mathrm{f_{R0}} = -10^{-6}$. For each redshift and each value of $\mathrm{f_{R0}}$ we compute the source term for a box with 700^3 particles and $\mathrm{L} = 700\ \mathrm{Mpc}\ h^{-1}$.

5.4 Displacement test

5.4.1 DUSTGRAIN–pathfinder simulations

To test how well our approximation for second order displacements does at reconstructing the positions of dark matter halos, I use a suite of N-body simulations run with $f(R)$ gravity (Giocoli et al., 2018), the DUSTGRAIN-pathfinder simulations. These simulations are performed with the MG-GADGET code (Puchwein et al., 2013) and consist of 768^3 particles of mass $8.1 \times 10^{10} M_{\odot}$ in a 750 h^{-1} Mpc side box. The adopted cosmology is the one of (Planck Collaboration et al., 2016): $\Omega_m = 0.31345$, $\Omega_b = 0.0481$, $\Omega_\Lambda = 0.68655$, $H_0 = 67.31 \mathrm{km\ s}^{-1}\ \mathrm{Mpc}^{-1}$, $A_s = 2.199 \times 10^{-9}$, $n_s = 0.9658$. The MG model is Hu–Sawicki $f(R)$ with n=1, and three different values for $f_{R0} = -10^{-4}$ (F4), -10^{-5} (F5), -10^{-6} (F6). For our tests, I use the simulation with $f_{R0} = -10^{-4}$ to maximize deviations from GR, and compare the halo power spectrum derived with our approximation to the one measured in the simulations. A reference ΛCDM simulation is also available. Halos are found by running a standard friends-of-friends halo finder on the simulation snapshots, using a linking length of 0.2 times the inter–particle distance.

5.4.2 Comparison results

The goal is to assess the performance of approximation for D_2 described in §5.3 for 2LPT in the context of MG models. For this purpose, I conduct an analysis similar to the one carried out in Munari et al. (2017a): the code is set up using the same initial conditions of the N-body simulation, distributing particles on a regular grid. Particles in the same Lagrangian positions are labelled with the same IDs as in the N-body simulation; they are displaced particles according to the approximated $D_2(k, a)$ and grouped in halos using the same membership of the simulation. Finally, the halo catalog is constructed, computing the position of each halo by averaging over the particles that belong to it. From the reconstructed catalog I evaluate the halo power spectrum, using the method described in Sefusatti et al. (2016), both for the “approximated” catalog and the simulation one. The result is shown in fig. 5.5 for three different redshifts: $z = 0, 0.2, 1.0$: here I plot the ratio of the halo power spectrum obtained when displacing particles with our approximation to the one measured from simulations. I show results for the Zel'dovich approximation (green lines) and for 2LPT approximated with the T1 triangle configuration (red lines), as well as the approximation proposed by Winther et al. (2017) (blue lines). The same quantities are computed for a ΛCDM simulation and plotted in fig. 5.6 at redshift $z = 0$ (top panel) and $z = 1$ (bottom panel); here the green line is again the Zel'dovich approximation, while the red line is 2LPT.

Since the fifth force introduced by the gravity modification enhances the clustering of matter, the value of σ_8 at $z = 0$ is larger for the $f(R)$ simulation than the ΛCDM one. In a sense, at a given redshift a Universe with MG is *more non-linear* with respect to one where gravity is described by GR. Given that the perturbative approach breaks down as the field becomes non-linear, a fair comparison between MG and ΛCDM should be performed between snapshots with the same level of non-linearity. To assess the performance of our method with $f(R)$ gravity with respect to ΛCDM I choose two snapshots with the same value of σ_8, and compare the halo power spectrum obtained for ΛCDM at redshift $z = 0$ (top panel of fig. 5.6) to the $f(R)$ one at $z = 0.2$ (middle panel of fig. 5.5).

In both cases, the second order approximation allows to reproduce the halo power spectrum within 10% up to $k \simeq 0.4\ h\ \mathrm{Mpc}^{-1}$ at $z = 1$ and $k \simeq 0.2\ h\ \mathrm{Mpc}^{-1}$ at $z = 0.2$ for $f(R)$. This result is similar to the one obtained for 2LPT with ΛCDM; to better quantify the performance of 2LPT with MG, I plot in fig. 5.7 the ratio $(P_{MG}(k)/P_{sim,MG}(k))/(P_{\Lambda CDM}(k)/P_{sim,\Lambda CDM})$: the deviation between the two is within 1% up to scales $k \simeq 0.4\ h$ Mpc^{-1}. Moreover, it can be seen from fig. 5.5 that the two approximations considered (T1 and the one proposed in Winther et al. 2017) yield very similar results in terms of the halo power spectrum, even though they showed a few percent difference with respect to the full source term.

I also perform a test to check the accuracy with which halo centers are reproduced from particles displaced with our approximation, with respect to the simulation catalogs. The result is shown in fig. 5.8 and fig. 5.9, both for the first-order Zel'dovich approximation (green lines) and 2LPT (red and blue lines, same color-coding as in fig. 5.5, with the case of ΛCDM 2LPT plotted in orange). Here I plot the distance between the halo-centers of the simulation and the ones in the approximated catalog, normalized to the inter-particle distance (corresponding to ~ 0.78 Mpc h^{-1}), as a function of the halo mass. To assess the performance of our 2LPT+MG approach, I compute

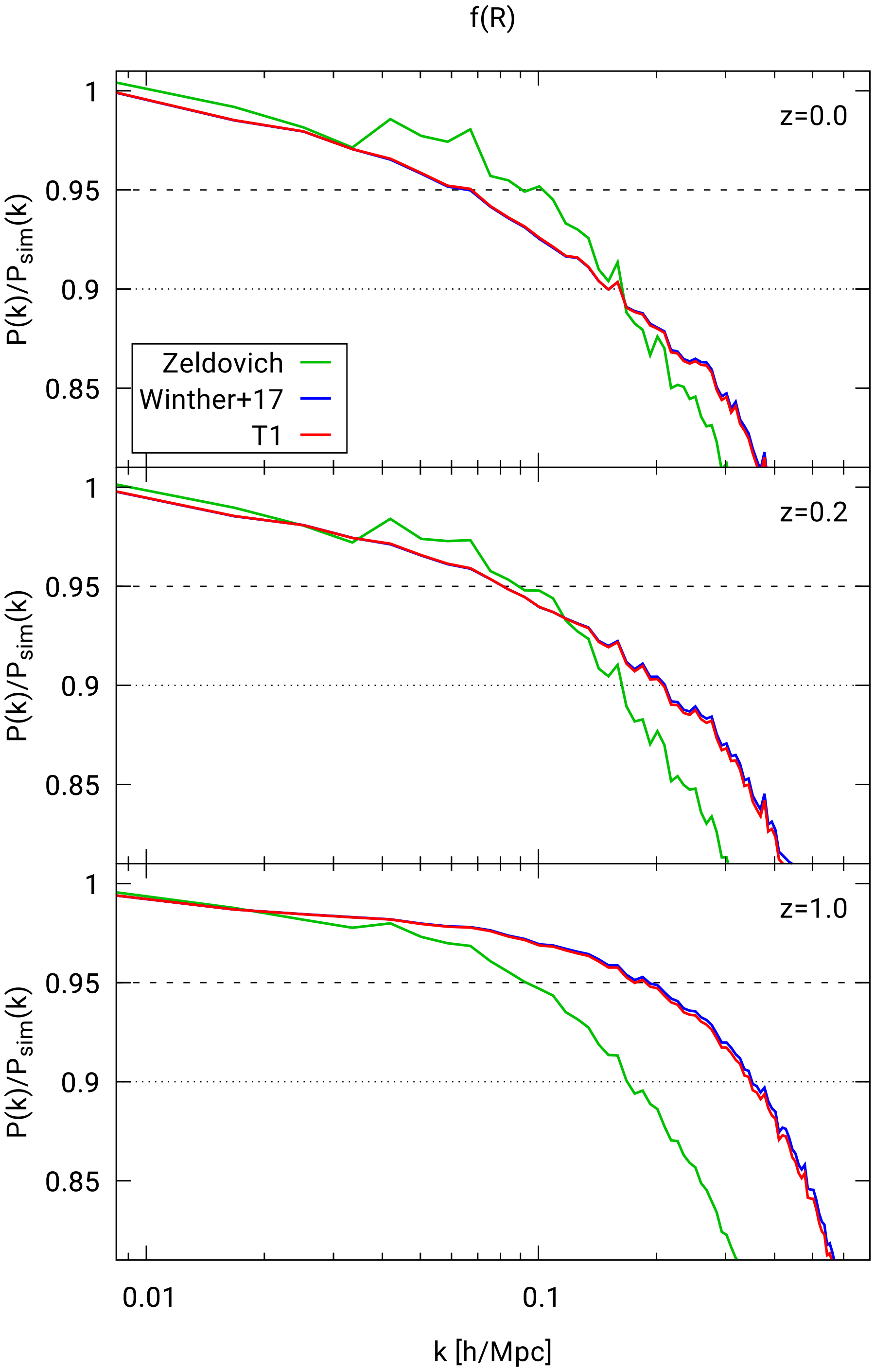

Fig. 5.5: Ratio of the halo power spectrum evaluated with different approximations to the one measured from simulations: in green is the Zel'dovich approximation, the red line is the T1 triangle with $k_1 = k_2$, $\theta = 90^o$. In blue we also plot the result obtained when adopting the approximation proposed in Winther et al. (2017). The dashed and dotted black lines mark respectively 5% and 10% deviation.

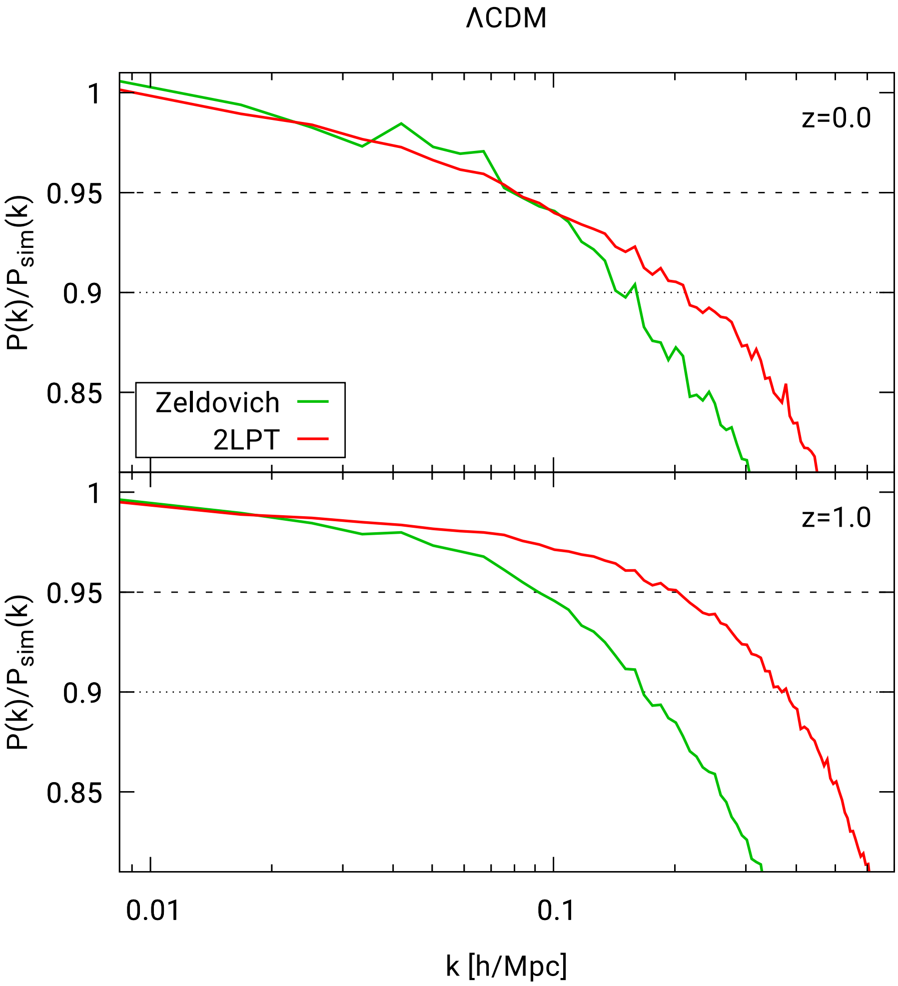

Fig. 5.6: Ratio of the halo power spectrum for ΛCDM at $z = 0$ (top panel) and $z = 1$ (bottom panel) with respect to the simulation. The particles are displaced with the Zel'dovich approximation (first order LPT, green line) or second order LPT (red line). The dashed and dotted black lines mark respectively 5% and 10% deviation.

halo distances also for the ΛCDM scenario (dashed lines in fig. 5.8 and 5.9). As before, in order to do a fair comparison between the perturbative approaches in the two gravity models with the same level of non-linearity, I compare the ΛCDM result at $z = 0$ to the MG one at $z = 0.2$ (fig. 5.8). It can be seen that, even though there is on average an error of ~ 0.8 times the inter-particle distance (green lines) for the first order, and ~ 0.4 times the

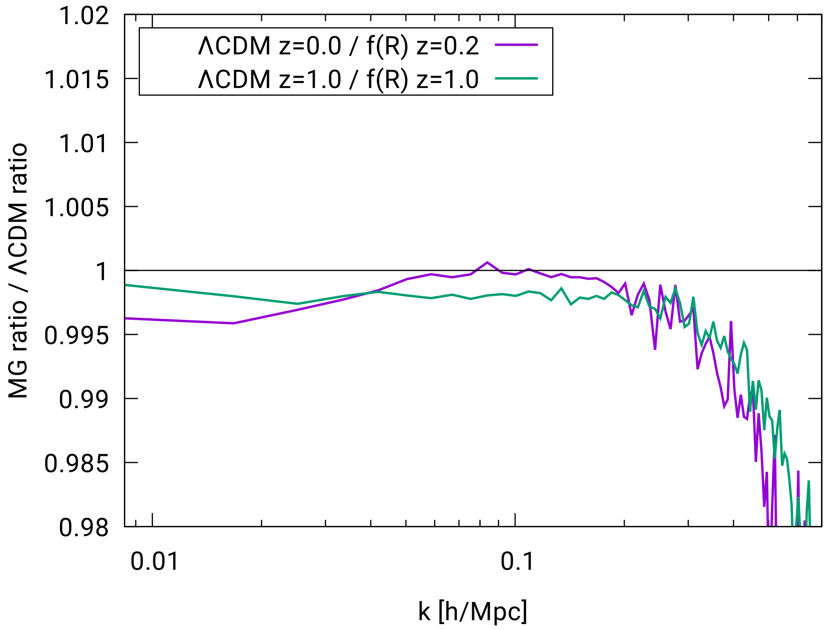

Fig. 5.7: Ratio of the orange lines of Fig. 5.5 to the blue lines of Fig. 5.6 for $z = 1$ (green line) and $z = 0.2$ for MG vs $z = 0$ for ΛCDM (purple line).

inter-particle distance for the second order, the performance is the same as the one shown by 2LPT+ΛCDM. Moreover, the error on the halo position is roughly independent from the halo mass. In fig. 5.9 I perform the same test but at redshift $z = 1$; as expected, the LPT halo centers are a better match to the simulation ones', and the performance for the MG model is again similar to the one obtained for the standard scenario.

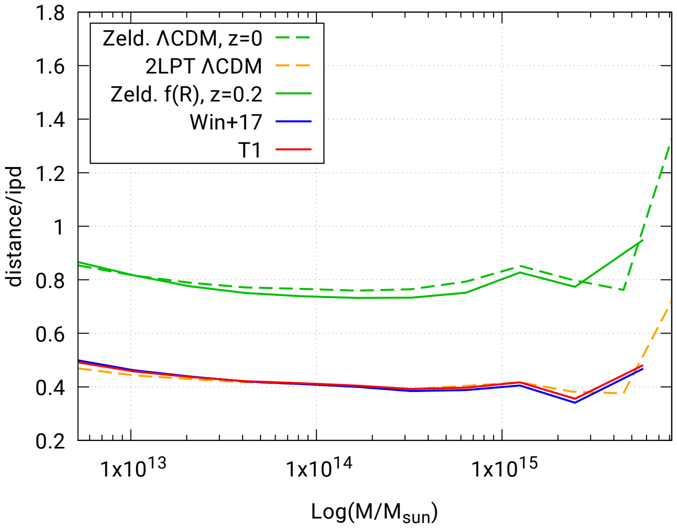

Fig. 5.8: Distance between the halo center as measured in the simulations to the one measured after halo reconstruction as a function of the halo mass, in units of inter–particle distance (*ipd*, $0.977\ \mathrm{Mpc}\ h^{-1}$). Dashed lines represent the median of the halo distance for the ΛCDM simulation at $z = 0$, while solid lines represent the same quantity for the $f(R)$ simulation at redshift $z = 0.2$. Green lines refer to particles displaced with first order LPT (Zel'dovich approximation), while the orange, blue and red lines represent respectively the ΛCDM 2LPT, the approximation used in Winther et al. (2017) for $f(R)$ 2LPT and the triangle configuration labeled as T1 in the previous plots.

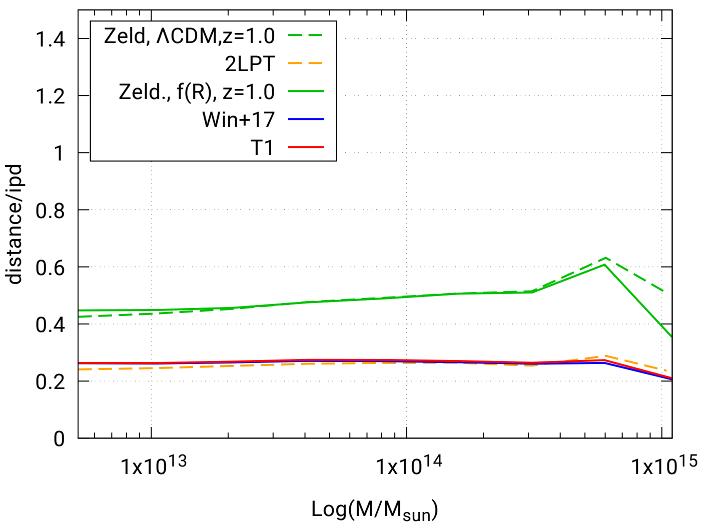

Fig. 5.9: Same as Fig. 5.8 but at redshift $z = 1$.

5.5 Extension to MG: first approach

As anticipated in §4.2, a first approach to extend PINOCCHIO to MG was to test if the technique used in Rizzo et al. (2017) for massive neutrinos gives acceptable results also in the case of $f(R)$ gravity. The linear growth rate is computed as the square root of ratios of linear power spectra generated with EFTCAMB, while the second order growth rate is obtained from eq. 4.4. The result of a comparison between halo power spectra (4.4): when adopting eq. 4.4 to compute 2LPT displacements, the resulting halo power spectrum does not show any improvements with respect to the linear approximation for intermediate scales $0.04\ h\ \mathrm{Mpc}^{-1} \leq k \leq 0.1\ h\ \mathrm{Mpc}^{-1}$.

The reason behind this can be explained if one compares the second order growth rate obtained from eq. 4.4 to the one obtained by solving the second order differential equation for the triangle T1 ($k_1 = k_2$, $\theta = 90°$), shown in fig 5.10. In the top panel I plot the ratio between $D_2(k,a)$ and $-3D_1^2(k,a)/7$ as a function of $\Omega_m(a)$. The black line represents the best fit obtained by Bouchet et al. (1995) for a ΛCDM Universe ($\Omega_m(a)^{-1/143}$), while the red, blue, orange and green lines show the ratio $D_2/(-3D_1^2/7)$ in the case of Hu–Sawicki $f(R)$ with $f_{R0} = -10^{-4}$, for increasing value of the wavenumber k as specified in the legend. The bottom panel shows the ratio of the lines of the top panel to $\Omega_m(a)^{-1/143}$. It can be seen that, in the case of scale-dependent growth induced by MG, eq. 4.4 does not provide a good description for D_2. In particular, even though the approximation is still accurate for the largest scales ($10^{-3}\ h$ Mpc^{-1}, red line), where relevant effects of MG are not expected on the growth rates, for smaller scales (and already at $k = 10^{-2}\ h$ Mpc^{-1}, blue line), the growth rate deviates for more than $\sim$ 3-4% from the fit, and the deviation gets more significant for smaller scales. This is due to the fact that the scale dependence of $D_2(k,a)$ is not accurately modeled by $D_1^2(k,a)$, therefore to properly treat mildly non-linear scales the fit of eq. 4.4 is not adequate, and one must resort to the method described in the previous sections.

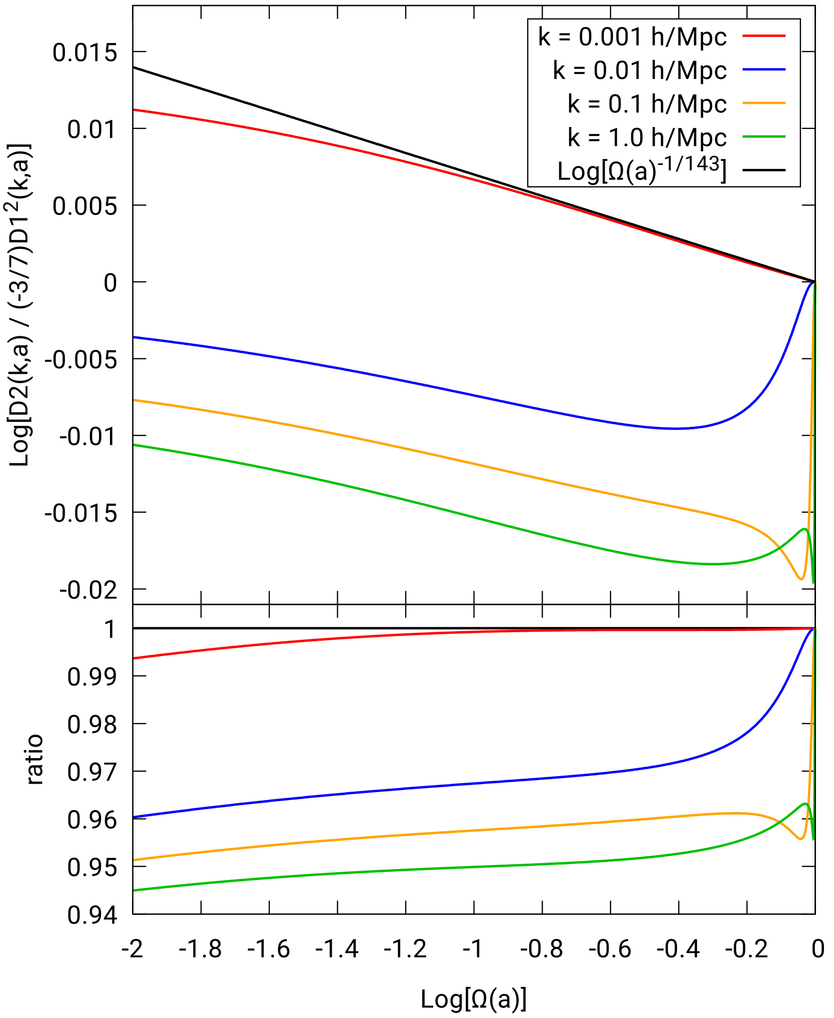

Fig. 5.10: *Top panel*: Ratio of the second order scale–dependent growth factor $D_2(k,a)$ to $(-3/7)D_1^2(k,a)$, as a function of $\Omega_m(a)$. The black line is the fit of Bouchet et al. (1995), $\Omega_m(a)^{-1/143}$, while the red, blue, orange and green lines show $D_2(k,a)$ for different values of k, respectively $0.001, 0.01$, 0.1 and 1 h/Mpc. The modified gravity model chosen is $n=1$ Hu–Sawicki with $f_{R0}=-10^{-4}$. *Bottom panel*: Ratio of $D_2(k,a)/(-3/7)D_1^2(k,a)$ to $\Omega_m(a)^{-1/143}$. For small values of k (red line) the fit of Bouchet et al. (1995) is still valid, as expected, however, already for $k=0.01h/\mathrm{Mpc}$, there is a deviation of $\sim 3-4\%$.

5.6 Summary and discussion

In this chapter I presented a new computation of second-order LPT that is valid for a class of modified gravity theories, and specialized it to the case of Hu-Sawicki $f(R)$ theory, testing its performances against N–body simulations. In MG theories the various expansion terms of LPT are typically not separable as products of time-dependent and space-dependent functions, and the equation for the second-order Fourier-space Lagrangian potential $\phi^{(2)}(\vec{k},a)$ can be written as an integral over two more vectors $\vec{k}_1$ and $\vec{k}_2$, that are constrained to form a triangle with $\vec{k}$. For the case in which the coefficients M_k (eq. 5.7) of the Taylor expansion of the fluctuations in the Ricci scalar δR are not scale-dependent, the differential equation for the 2LPT displacement potential can be written in terms of direct and inverse Fourier transforms. This allows to treat it with a numerical approach.

Using an initial density field sampled in cubic boxes of varying size and number of grid points, I numerically characterized the source term of the 2LPT potential (normalized by its GR counterpart) by computing its average and standard deviation as a function of k. I considered different triangle configurations to find the second order growth factor $D_2(k,k_1,k_2,a)$ that best reproduces the average of the source term, and used it to achieve an effective separation of the 2LPT displacement field into a space part, that does not depend on time and is equal to that used in GR, and a k-dependent second-order growth rate $D_2(k,a)$. The latter can be computed by numerically integrating a set of ordinary differential equations, one for each k value. The scatter in the numerical solution around the average source term gives a measure of the accuracy of this approximation, and is found to be moderate at the scales where 2LPT is relevant. I also tested the approximations chosen for $D_2(k,a)$ at different redshifts and for different values of the f_{R0} parameter, and found that the chosen triangle configurations can be safely adopted.

I implemented the solution for both differential equations for $D_2(k,a)$ in our code to compute Lagrangian displacements, and followed the approach discussed in Munari et al. (2017a) to test the accuracy level to which the approximation can reproduce halo positions with respect to an N-body simulation. I produced a second-order displacement field, and compared with the results of a simulation run with MG-Gadget (Giocoli et al., 2018) and Hu-Sawicki $f(R)$ gravity (with a large value of $f_{R0}=-10^{-4}$, to maximize the effect of modified gravity). The halos in the simulation were identified using a standard friends-of-friends halo finder algorithm. To construct the “approximated” halo catalog, I used the same particle assignment of the simulation to group particles displaced with 2LPT, then I re-computed each halo center of mass as the average over all particles that belong to it. Using these halo displacements I computed the halo power spectrum and compared it with that measured from the N-body halo catalog. As demonstrated by Munari et al. (2017a) in the context of ΛCDM, this procedure allows to test how an approximate method like 2LPT can recover the clustering of halos without being required to solve the much harder problem of identifying halos themselves. Both chosen triangle configurations, together with the one previously proposed by Winther et al. (2017), perform well in terms of the halo power spectrum, allowing to reconstruct it within $\sim$ 10% at mildly non linear scales ($k \simeq 0.2 - 0.4\ h\ \mathrm{Mpc}^{-1}$). This performance is the same (within 1%) as the one shown by 2LPT in a standard, ΛCDM Universe with GR, as highlighted in Fig. 5.7, meaning that the loss of power in the reconstructed halo $P(k)$ with respect to the N-body one is mostly due to the failure of the perturbative approach as the displacement field becomes non-linear. I conclude that LPT can be safely used to displace particles even in presence of MG. The method used to construct the halos, by matching the particle memberships to the simulation ones, allows to perform an object–by–object analysis. I verify how good our approximation for the halo displacements is at recovering the halo positions with respect to the simulation. The result is again consistent with the one obtained in a ΛCDM scenario.

Throughout this analysis, I focused in particular on Hu-Sawicki $f(R)$. The method I propose is however quite general, and can be extended to other MG theories: once the functional form for the $\mu(k, a)$ function (that parameterizes the Fourier-space Poisson equation) and the M_k coefficients are known, such procedure propose can be employed to find a proper approximation for D_2. If the M_k coefficients are scale-dependent the method can in principle still be applied, provided that the S_3 (scalar field self-interaction) term of eq. 5.19 can be written in terms of Fourier transforms. This requires identifying the proper operators in configuration space that correspond to the M_k coefficients in Fourier space. The procedure must be done only once for each gravity theory, and does not require the use of N–body simulations. This allows to produce large sets of approximated simulations for different gravity models, a task that plays a crucial role in the computation of the covariance matrices needed to constrain cosmological parameters. Scale-dependent growth is implemented in the PINOCCHIO code as an optional functionality, making it able to generate 2LPT displacements fields with modified gravity. However, a key part of the algorithm is the one that groups particles in halos, needed to make the code fully predictive. In the standard PINOCCHIO code this is done by treating overdensities as homogeneous ellipsoids and computing collapse times as the moment of first orbit crossing, as described in §4. In the next chapter I describe an extension of ellipsoidal collapse to MG suitable to be implemented in PINOCCHIO.

Chapter 6

Ellipsoidal collapse with Modified Gravity

In the previous chapter I described the extension of 2LPT to $f(R)$ models, together with a new numerical method developed to test different approximations for the second-order growth rate. Such approximation is required to achieve a quick computation of LPT displacements, crucial for implementation in PINOCCHIO. The second ingredient, essential to have a full extension of the code, is a proper formulation of Ellipsoidal Collapse (EC) in the context of MG theories. In the standard case, PINOCCHIO implements the LPT approach to EC (Monaco 1997a,b, see §2.3.3). The computation of collapse times (CT) with the LPT description is fast, since it only requires solving a cubic equation for $D(a_{\mathrm{coll}})$. Such technique results in an overestimation of collapse times for spherical overdensities, due to the slow convergence properties of the LPT series for spherical and quasi-spherical configurations. However, the problem can easily be circumvented by applying a correction (eq. 2.55) to reproduce spherical collapse.

Nonetheless, the LPT description of EC cannot be trivially extended to the MG case, since it employs as a time variable the growth factor. The latter acquires a scale-dependence in MG theories, as extensively discussed in §5. As a consequence, the suitable approaches are those that numerically integrate the equations for the evolution of the ellipsoid axes in their full generality, as a function of time, developed by Bond & Myers (1996) (BM) and Nadkarni-Ghosh & Singhal (2016) (NGS). In this chapter I describe how to extend the computation of CT for ellipsoidal overdensities in presence of MG. I perform thorough tests on the three EC approaches described in §2.3.3 in the standard ΛCDM scenario. Starting from the results of Ruan et al. (2020), that extend the BM approach to $f(R)$ models, I derive an extension of the NGS prescription (§6.2.2). The latter is suitable for implementation in PINOCCHIO, being $\sim$30 times faster than the BM approach. The implementation is currently ongoing. In §6.3 I summarize the software development status. As for the extension of LPT displacements described in §5, I focus on Hu-Sawicki $f(R)$. The results discussed here will be the subject of a future paper (Moretti 2020, in preparation).

6.1 Comparison of EC in ΛCDM

The three different prescriptions for EC described in §2.3.3 can be adopted for the purpose of computing CT for ellipsoidal overdensities:

- The BM approach (Bond & Myers, 1996), which describes the evolution of the ellipsoid dimensionless principal axes a_i by means of three coupled second-order integro-differential equations (2.43;

- The NGS approach (Nadkarni-Ghosh & Singhal, 2016), describing the dynamics of triaxial collapse in terms of eigenvalues of the deformation tensor $\lambda_{a,i}$, the velocity derivative tensor $\lambda_{v,i}$ and the gravity Hessian $\lambda_{d,i}$. Computing CT involves solving a set of nine coupled first-order differential equations (2.49);

- The LPT approach (Monaco, 1997a,b) is the one currently implemented in PINOCCHIO. It is based on the Taylor expansion of the ellipsoid potential. This method involves solving an algebraic equation for the linear growth rate $D_1(a)$, of the same order of the perturbative order chosen in the expansion (2.54); in what follows I adopt the LPT expansion up to third-order.

In order to extend the computation of EC in PINOCCHIO to MG theories, and in view of the need to adopt a different description with respect to the one currently implemented, I perform a comparison between the three methods. I assess the performances of the three approaches, integrating the equations of EC for the first two methods and solving the algebraic equation of the LPT method. I compare the CT obtained, extending the analysis of Monaco (1995, 1997b). In this context, collapse is defined as the time when the shortest axis goes to zero, corresponding to the moment of orbit crossing. Hence, for each method the time of collapse is computed as:

- *BM approach*: if a_i are the dimension-less principal axes of the ellipsoid, and the eigenvalues of the tidal tensor are ordered as $\lambda_1 \geq \lambda_2 \geq \lambda_3$, collapse times are evaluated as the time when $a_1 = 0$;

- *NGS approach*: given the above definition of collapse for the BM approach, and the definitions of the nine dimensionless parameters of 2.48, collapse occurs when $\lambda_{a,1} = 1$;

- *LPT approach*: collapse corresponds to the time the Jacobian of the transformation from Eulerian to Lagrangian coordinates vanishes, identified as the value of the linear growth rate $D(a_{\rm coll})$ that solves eq. 2.54.

In all cases, CT is completely determined by the eigenvalues of the tidal tensor λ_i. Moreover, $\delta = \sum_i \lambda_i$.

As previously discussed, the LPT approach provides with a faster numerical solution than the BM one, though it has slow convergence properties in the case of spherical overdensities, resulting in an over-estimation of spherical collapse times evaluated with LPT. This can be seen in Fig. 6.1, where I plot collapse times obtained with the LPT and the BM descriptions, shown respectively in blue and orange. Fixing $\delta_{\rm L}(a = 1) = 1.686$, I vary the eigenvalues λ_i, thus considering different ellipsoidal shapes. The latter are described as combinations of the eigenvalues of the tidal tensor, $x = \lambda_1 - \lambda_2$, $y = \lambda_2 - \lambda_3$, so $x = y = 0$ corresponds to the spherical case. On the z axis I plot the collapse times evaluated for the different combinations of λ_i. Except for the cases close to spherical, the LPT approach is in good agreement with the BM approach. The cosmology is set to an Einstein-de Sitter Universe ($\Omega_{m,0} = 1$); as expected, the BM approach correctly reproduces the spherical case (i.e. an overdensity $\delta_{\rm L} = 1.686$ collapses at $a_{\rm coll} = 1$).

A better visualization of the comparison between different approaches can be obtained plotting the residuals between CT evaluated with two methods, as in Fig. 6.2. There I plot $100 \times ({\rm CT_{LPT}}/{\rm CT_{BM}} - 1)$ (color-coded) as a function of $x = \lambda_1 - \lambda_2$ and $y = \lambda_2 - \lambda_3$. I stress that the color-bars in the two panels span different ranges, to properly display the % deviations as a

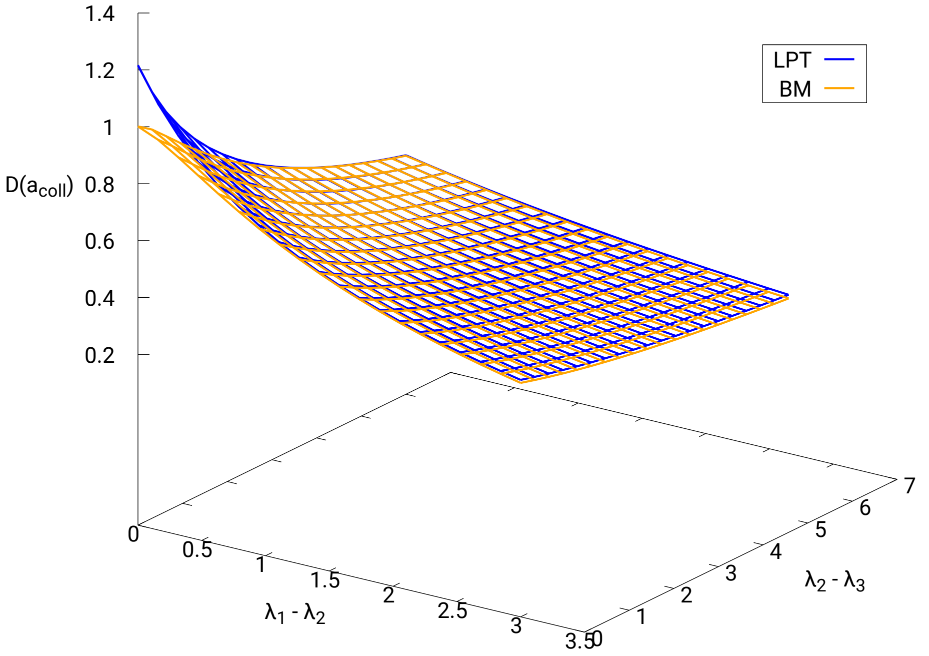

Fig. 6.1: Collapse times as a function of the shape of the ellipsoid $\lambda_1 - \lambda_2$ and $\lambda_2 - \lambda_3$. The λ_i are chosen so that the linearly evolved overdensity $\delta = 1.686$. Collapse times obtained with LPT are in blue, those obtained with BM are in orange. The poor performance of LPT respect to the BM method in quasi-spherical cases is evident.

function of the ellipsoid shape. In this case I consider a flat ΛCDM cosmology with $\Omega_{m,0} = 0.3$, and a linearly evolved overdensity $\delta_L = 3$. The values of λ_i are chosen varying $0 \leq x \leq 3$, $0 \leq y \leq 6$. The top panel of Fig. 6.2 shows the % difference between collapse times computed with LPT and BM when no spherical correction is applied: in this case the two methods show a discrepancy as high as 20% for quasi-spherical cases. The bottom panel shows the same quantity after applying the spherical correction of eq. 2.55: in this case the deviation is reduced to $\leq 2.5\%$. Collapse times are evaluated in terms of the linear growth rate $D(a_{\rm coll})$.

In Fig. 6.3 I show the comparison between the NGS and the BM prescriptions (top panel), and the LPT and BM prescriptions, with the spherical correction applied to LPT computed CT (bottom panel, same as the bottom panel of Fig. 6.2). Note that again the color-bars span different ranges: the difference in CT computed with BM and NGS is $\leq$0.22%, confirming that the two methods are numerically equivalent.

The same comparison is performed for different values of δ, yielding similar results. Moreover, the NGS approach is $\sim$ 30 times faster than BM, owing to the fact that the differential equations to solve do not involve the computation of elliptic integrals. The NGS description of EC is therefore our choice for the implementation in PINOCCHIO, since it allows for a fast solution with negligible compromises on the accuracy in the computation of CT with respect to the BM approach. As of now, the code has been modified to evaluate CT with the NGS description in the context of standard ΛCDM. This change results in more precise computation of CT respect to the previous implementation, based on LPT. Moreover, it is propaedeutic for the purpose of extending the code to MG, given that the scale-dependent growth rate (used in LPT) cannot be used as time variable. As anticipated, the BM and NGS methods are both suitable to be extended to MG, since they numerically integrate the equations for the evolution of the ellipsoid axes as a function of time. An extension of the BM approach to Hu-Sawicki $f(R)$ is developed in Ruan et al. (2020) and described in §6.2.1. Starting from those results, I derive an extension of the NGS method which is suitable to be implemented in PINOCCHIO, described in §6.2.2.

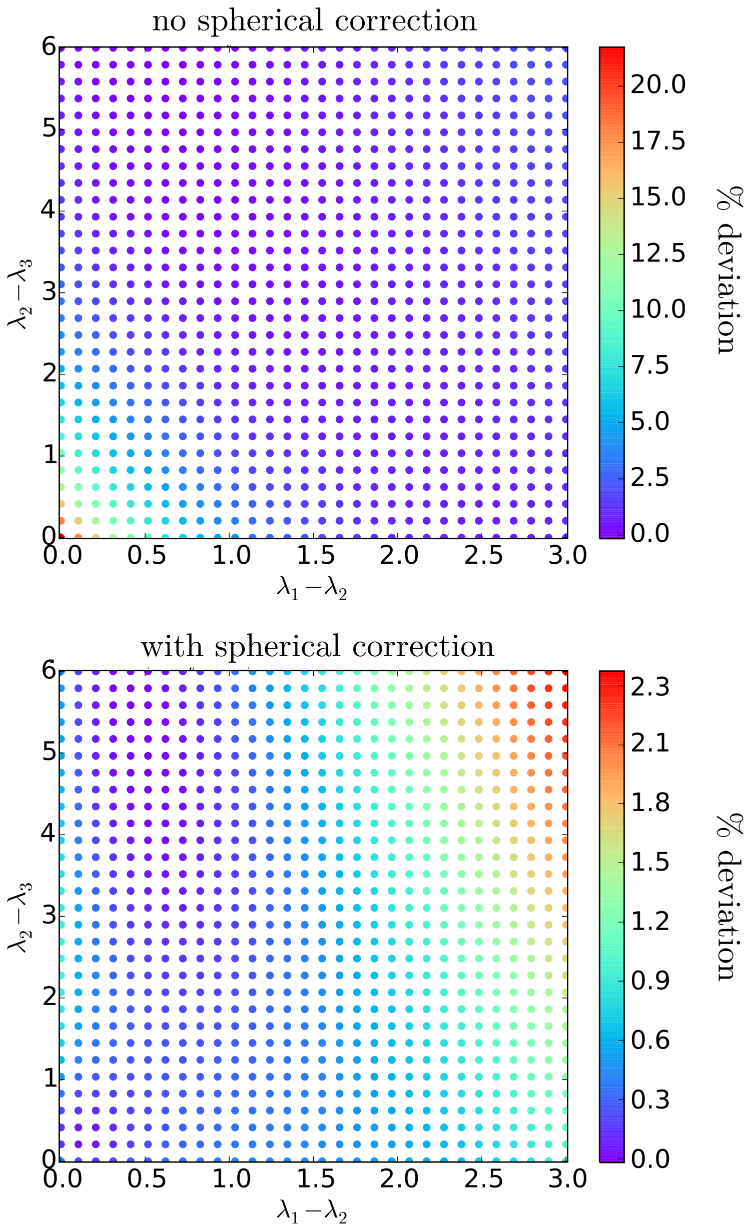

Fig. 6.2: % deviation of collapse times computed with the LPT and BM approach, color-coded. The top panel shows the result when no spherical correction is applied, while the bottom panel shows the corrected results. The discrepancy is reduced from being as high as 20% to $\leq 2.5\%$. Note that the color-bars span different ranges.

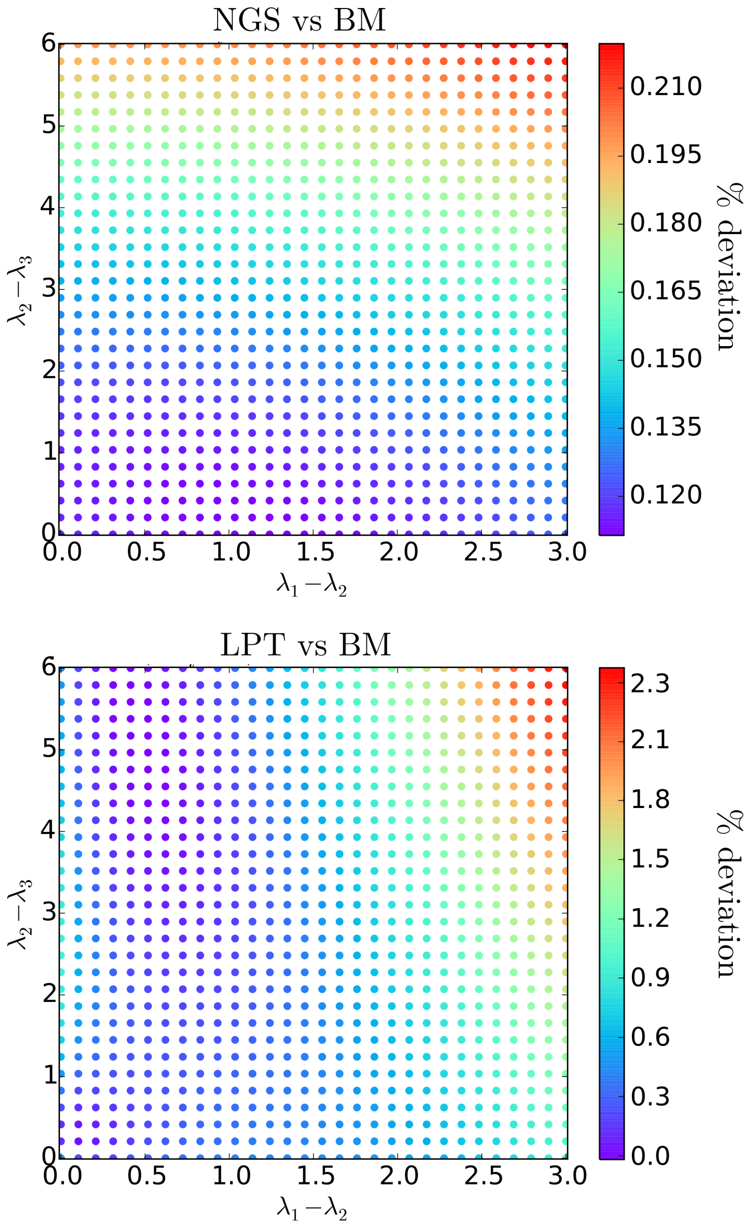

Fig. 6.3: % deviation of collapse times computed with the NGS and BM approaches (top panel), and LPT and BM approaches corrected to reproduce spherical collapse (bottom panel), color-coded. Note that the color-bars span different ranges.

6.2 Gravitational collapse in MG

A proper description of gravitational collapse in the context of MG should take into account both the gravity enhancement due to the fifth force and a screening mechanism, required to comply with Solar System constraints. As anticipated in §3.3, for $f(R)$ models the mechanism at play is the chameleon (Khoury & Weltman, 2004a): a scalar field can acquire an effective mass that is environmentally dependent. In high density regions, such mass becomes large, effectively hiding the additional degree of freedom and suppressing the fifth force. On the other hand, in low density environments such as in cosmological volumes, the mass associated with the field is small and the effects of MG can be manifest. In the non-relativistic limit the scalar field equation of motion can be written as:

$$\nabla^2\varphi = \frac{\mathrm{d}V_{\rm eff}}{\mathrm{d}\varphi} \ , \tag{6.1}$$

where $V_{\rm eff}(\varphi)$ is the scalar field potential plus a contribution from the coupling of φ to the matter field, $V_{\rm eff}(\varphi) = V(\varphi) + \rho\exp(\sqrt{8\pi}\beta\varphi)$. The second derivative of $V_{\rm eff}$ is the effective mass of the scalar field, m^2_φ.

The behavior of scalar field outside of massive objects can be shown to be dependent on the ratio of $\Delta\varphi$ (i.e. the difference in the value of the scalar field inside and outside the object), to the value of the Newtonian potential at the surface of the object Φ_N. In particular, satisfying the condition

$$\frac{\sqrt{8\pi}(\varphi_{\rm out} - \varphi_{\rm in})}{6\beta\Phi_N} \ll 1 \ , \tag{6.2}$$

results in a configuration of the gravitational field where φ occupies the minima of the effective potential inside and outside the object, except for a thin shell where the value of φ increases from $\varphi_{\rm in}$ to $\varphi_{\rm out}$. Here β is the strength of the coupling between the additional degree of freedom and matter ($\beta = -1/\sqrt{6}$ for $f(R)$).

Khoury & Weltman (2004a) derive an estimation for the radial profile of the scalar field in the case of a spherical top-hat overdensity of physical radius $R_{\rm TH}$, with constant inner and outer densities $\rho_{\rm in}$ and $\rho_{\rm out}$ respectively. The distance needed for the MG scalar field φ to settle from the outside value

$\varphi_{\rm out}$ to the inside value $\varphi_{\rm in}$ in the case of a spherical top-hat is:

$$\frac{R_{\rm TH}-R_0}{R_{\rm TH}}=\frac{\Delta R}{R_{\rm TH}}\simeq\frac{1}{\sqrt{8\pi G}\beta}\frac{\varphi_{\rm out}-\varphi_{\rm in}}{\rho_{\rm in}R_{\rm TH}^2}\ . \tag{6.3}$$

The condition of eq. 6.2 results then in the requirement that $\Delta R/R_{\rm TH}\ll 1$, i.e. a thin shell is present. The values of the scalar field that minimize the effective potential inside and outside the shell are, for Hu-Sawicki $f(R)$:

$$\varphi_{\rm in/out}=f_{R,{\rm in/out}}\simeq\left[\frac{1+4\Omega_\Lambda/\Omega_m}{\tilde\rho_{\rm in/out}a^{-3}+4\Omega_\Lambda/\Omega_m}\right]^{n+1}f_{R0}\ , \tag{6.4}$$

where $\tilde\rho_{\rm in/out}=\rho_{m,{\rm in/out}}/\bar\rho_m$. The thickness of the thin shell 6.3 can then be written as:

$$\begin{aligned}\frac{\Delta R}{R_{\rm TH}}\simeq\frac{|f_{R0}|a^3}{\Omega_m\tilde\rho_{\rm in}(H_0R_{\rm TH})^2}&\Bigg[\left(\frac{1+4\Omega_\Lambda/\Omega_m}{\tilde\rho_{\rm out}a^{-3}+4\Omega_\Lambda/\Omega_m}\right)^{n+1}\\&-\left(\frac{1+4\Omega_\Lambda/\Omega_m}{\tilde\rho_{\rm in}a^{-3}+4\Omega_\Lambda/\Omega_m}\right)^{n+1}\Bigg]\ .\end{aligned} \tag{6.5}$$

Considering the radial profile for the scalar field $\varphi(r)$ for $r\in[R_0,R_{\rm TH}]$ derived in Khoury & Weltman (2004a):

$$\varphi(r)\simeq\varphi_{\rm in}+\frac{\sqrt{8\pi}\beta}{3}\rho_{\rm in}\left[\frac{r^2}{2}+\frac{R_0^3}{r}-\frac{3}{2}R_0^2\right]\ , \tag{6.6}$$

it is possible to write the additional force felt by a test mass at $R_{\rm TH}$ as:

$$\mathcal{F}\frac{GM}{R_{\rm TH}^2}=\sqrt{8\pi}\beta\ \nabla\varphi|_{R_{\rm TH}}\simeq\frac{GM}{3R_{\rm TH}^2}\left[3\frac{\Delta R}{R_{\rm TH}}-3\left(\frac{\Delta R}{R_{\rm TH}}\right)^2+\left(\frac{\Delta R}{R_{\rm TH}}\right)^3\right]\ . \tag{6.7}$$

Since $R_{\rm TH}\geq R_0$ and $R_0\geq 0$, $\Delta R/R_{\rm TH}\in[0,1]$ and the enhancement of gravity is $\mathcal{F}\in[0,1/3]$. Following Lombriser et al. (2013), the force enhancement is taken to be the quantity in square brackets in eq. 6.7:

$$\mathcal{F}=\frac{1}{3}\min\left(1,3\frac{\Delta R}{R_{\rm TH}}-3\left(\frac{\Delta R}{R_{\rm TH}}\right)^2+\left(\frac{\Delta R}{R_{\rm TH}}\right)^3\right)\ . \tag{6.8}$$

With this description, the gravity modification can be expressed in terms of an effective gravitational constant $G_{\rm eff}=G\,(1+\mathcal{F})$.

The evolution for the spherical overdensity in terms of the dimensionless comoving radius $y = r(a)/aR_{\rm TH}$, with r the physical radius of the overdensity, is:

$$y_h'' + \left[2 - \frac{3}{2}\Omega_m(a)\right] y_h' + \frac{1}{2}\Omega_m(a)(1+\mathcal{F})(y_h^{-3} - 1)y_h = 0 \; , \tag{6.9}$$

where $'$ denotes derivation with respect to $\ln a$ and $\mathcal{F}$ depends on the density of the environment via eq. 6.3. The environment is assumed to follow a ΛCDM evolution, so that:

$$y_{\rm env}'' + \left[2 - \frac{3}{2}\Omega_m(a)\right] y_{\rm env}' + \frac{1}{2}\Omega_m(a)(y_{\rm env}^{-3} - 1)y_{\rm env} = 0 \; . \tag{6.10}$$

6.2.1 Extension of the BM approach

Starting from the modeling of spherical collapse in MG described in the previous section, Ruan et al. (2020) present an extension of the BM approach to ellipsoidal collapse to Hu-Sawicki $f(R)$, applying it in the context of excursion set theory. The basic idea is to consider the gravity modification as an effective gravitational constant $G_{\rm eff} = G(1+\mathcal{F})$, where $\mathcal{F}$ is the force enhancement derived from the radial profile of φ for the spherical case 6.8. To take into account triaxial symmetry, the spherical radius y_h is replaced by an “effective” radius $(Y_1Y_2Y_3)^{1/3}$. The Y_i are the dimension-less comoving principal axes of the ellipsoid. The thickness of the thin shell can then be written as:

$$\begin{aligned}\frac{\Delta R}{R} = \frac{|f_{R0}|c^2a^7}{\Omega_{m,0}(H_0R_{\rm init})^2}(Y_1Y_2Y_3)^{-1/3} &\left[\left(\frac{1+4\Omega_\Lambda/\Omega_{m,0}}{y_{\rm env}^{-3} + 4a^3\Omega_\Lambda/\Omega_{m,0}}\right)^2\right. \\ &\left. - \left(\frac{1+4\Omega_\Lambda/\Omega_{m,0}}{(Y_1Y_2Y_3)^{-1} + 4a^3\Omega_\Lambda/\Omega_{m,0}}\right)^2\right] \; .\end{aligned} \tag{6.11}$$

In terms of the dimension-less axes $a_i = aY_i$ of eq. 2.46, the evolution equation in MG reads:

$$\begin{aligned}\frac{{\rm d}^2a_i}{{\rm d}a^2} + \left(\frac{1}{a} + \frac{E'(a)}{E(a)}\right)\frac{{\rm d}a_i}{{\rm d}a} + &\left(\frac{3\Omega_{m,0}}{2a^5E^2(a)}C_i(a)(1+\mathcal{F})\right. \\ &\left. - \frac{2\Omega_\Lambda a^3 - \Omega_{m,0}}{2a^5E^2(a)}\right) a_i = 0 \; .\end{aligned} \tag{6.12}$$

Eq. 6.12 constitutes a set of three coupled second-order integro-differential equations that describe the time-evolution of the ellipsoid principal axes. The formulation is equivalent to the standard BM prescription of eq. 2.46, but with an enhanced gravitational force described by the $\mathcal{F}$ term. The latter depends on the evolution of the environment (computed solving eq. 6.10) through eq. 6.8 and6.11. With respect to the standard case, solving eq. 6.12 involves two additional parameters: the density of the environment $\delta_{\rm env}$ and the mass of the halo $M_h = 4\pi/3(R_{\rm init}a_{\rm init})^3\bar{\rho}_{m,\rm init}$ (or equivalently $R_{\rm init}$). The evolution of the ellipsoid is then completely specified by M_h, $\delta_{\rm env}$, λ_i, together with the cosmological parameters and the value of f_{R0}.

6.2.2 Extension of the NGS approach

Following the dynamics of the ellipsoid described by eq. 6.12, as in the standard case, involves the computation of elliptic integrals. As anticipated before, this makes the BM integro-differential equations ill-suited to be implemented in an fast approximate method such as PINOCCHIO, in which the computation of collapse times is repeated many times. However, as I showed in §6.1, the NGS approach yield very similar results to the BM description, but in a fraction (~1/30) of the time. We choose to adopt the NGS description of EC, using the prescription of Ruan et al. (2020) to extend it to $f(R)$. I start from the definition of the eigenvalues of the deformation tensor, the velocity derivative tensor and the gravity Hessian:

$$\begin{aligned}
\lambda_{a,i} &= 1 - \frac{a_i}{a} \ , \\
\lambda_{v,i} &= \frac{1}{H}\frac{\dot{a}_i}{a_i} - 1 \ , \\
\lambda_{d,i} &= \frac{\delta\alpha_i}{2} + \lambda_{ext,i} = C_i - \frac{1}{3} \ ,
\end{aligned} \tag{6.13}$$

and proceed to derive the equations for the evolution of the eigenvalues as in Nadkarni-Ghosh & Singhal (2016): I derive the eigenvalues 6.13 respect to the scale factor a, adopting the modified equation 6.12 for the a_i. The resulting evolution equations for the eigenvalues $\lambda_{a,i}$, $\lambda_{v,i}$, $\lambda_{d,i}$ are:

$$\begin{aligned}
\frac{\mathrm{d}\lambda_{a,i}}{\mathrm{d}\ln a} &= -\lambda_{v,i}(1-\lambda_{a,i}) \\
\frac{\mathrm{d}\lambda_{v,i}}{\mathrm{d}\ln a} &= -\frac{1}{2}\left[3\Omega_m(a)\lambda_{d,i}(1+\mathcal{F}) - \left(\Omega_m(a) - 2\Omega_\Lambda(a) - 2\right)\lambda_{v,i} + 2\lambda_{v,i}^2\right] \\
\frac{\mathrm{d}\lambda_{d,i}}{\mathrm{d}\ln a} &= -(1+\delta)\left(\delta + \frac{5}{2}\right)^{-1}\left(\lambda_{d,i} + \frac{5}{6}\right)\sum_{j=1}^{3}\lambda_{v,j} + \\
&\quad + \left(\lambda_{d,i} + \frac{5}{6}\right)\sum_{i=1}^{3}(1+\lambda_{v,i}) - \left(\delta + \frac{5}{2}\right)(1+\lambda_{v,i}) + \\
&\quad + \sum_{j\neq i}\frac{(\lambda_{d,j} - \lambda_{d,i}[(1-\lambda_{a,i})^2(1+\lambda_{v,i}) - (1-\lambda_{a,j})^2(1+\lambda_{v,j})]}{(1-\lambda_{a,i})^2 - (1-\lambda_{a,j})^2}
\end{aligned} \tag{6.14}$$

where $\mathcal{F}$ is evaluated from eq. 6.8. The thickness of the thin-shell is:

$$\begin{aligned}
\frac{\Delta R}{R} = \frac{|f_{R0}|c^2 a^7}{\Omega_{m,0}(H_0 R_{\mathrm{init}})^2}\left[\sum_i (1-\lambda_{a,i})\right]^{-1/3} \times \Bigg[\left(\frac{1 + 4\Omega_\Lambda/\Omega_{m,0}}{y_{\mathrm{env}}^{-3} + 4a^3\Omega_\Lambda/\Omega_{m,0}}\right)^2 - \\
\left(\frac{1 + 4\Omega_\Lambda/\Omega_{m,0}}{\left[\sum_i (1-\lambda_{a,i})\right]^{-1} + 4a^3\Omega_\Lambda/\Omega_{m,0}}\right)^2\Bigg] .
\end{aligned} \tag{6.15}$$

Note that only the equation for the eigenvalues of the velocity derivative tensor $\lambda_{v,i}$ is modified, with the inclusion of the $(1+\mathcal{F})$ term. For the purpose of implementing EC of mass elements in PINOCCHIO we set the density of the local environment to the background value $\rho_{\mathrm{env}} = \bar{\rho}_m$, so that $\delta_{\mathrm{env}} = 0$ and $y_{\mathrm{env}} = 1$. Moreover, we identify the initial radius of the halo R_{init} with the smoothing radius.

Following the definition of collapse as orbit crossing, the ellipsoid collapses as $\lambda_{a,1} \to 1$, provided that the initial eigenvalues are sorted as $\lambda_{a,1} \geq \lambda_{a,2} \geq \lambda_{a,3}$. In Fig. 6.4 I show the evolution of the axes a_i as a function of time for an ellipsoidal configuration in Hu-Sawicki $f(R)$ with $f_{R0} = -10^{-4}$ (solid lines), as well as the same quantity for the standard GR case (dashed lines). The evolution is computed solving eq. 6.14, the a_i can be evaluated from the definition of the $\lambda_{a,i}$ 6.13. The initial conditions for the eigenvalues are set to $\lambda_{a,1} = 1.5$, $\lambda_{a,2} = 1.3$, $\lambda_{a,3} = 1$. In the case shown, collapse occurs earlier with respect to the GR case because of the gravity enhancement.

In Fig. 6.5 I plot the evolution of the shortest axis of the ellipsoid (the first

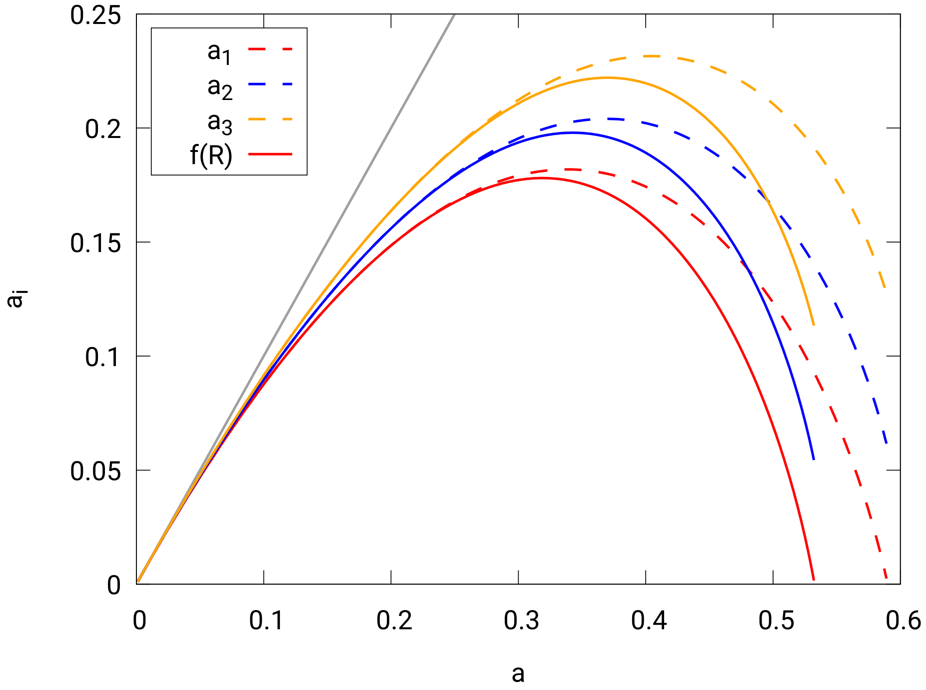

Fig. 6.4: Evolution of the principal axes of an ellipsoid with $\lambda_{a,1} = 1.5$, $\lambda_{a,2} = 1.3$, $\lambda_{a,3} = 1$ computed solving eq. 6.14 (solid lines) for $f_{R0} = -10^{-4}$, compared to the standard case (dashed lines).

to collapse, top panel) and of the $\lambda_{a,1}$ eigenvalue (bottom panel) for different values of the f_{R0} parameter, as stated in the legend. Fig. 6.5 confirms that increasingly smaller values of f_{R0} reduce to the GR case (shown in black). The results summarized in this section are preliminary, tests performed so far include:

- In cases where the modification of gravity is not screened, collapse occurs earlier due to enhancement in the gravitational force, as shown in Fig. 6.4. Future tests will involve a proper characterization of the screening mechanism;

- I numerically solve eq. 6.12 (BM) and 6.14 (NGS) for some configurations, confirming that the evolution for the ellipsoid axes and the collapse times are the same in the two approaches. This test will be extended as the comparison shown in Fig. 6.3, considering a grid of values for the λ_i and different values of δ;

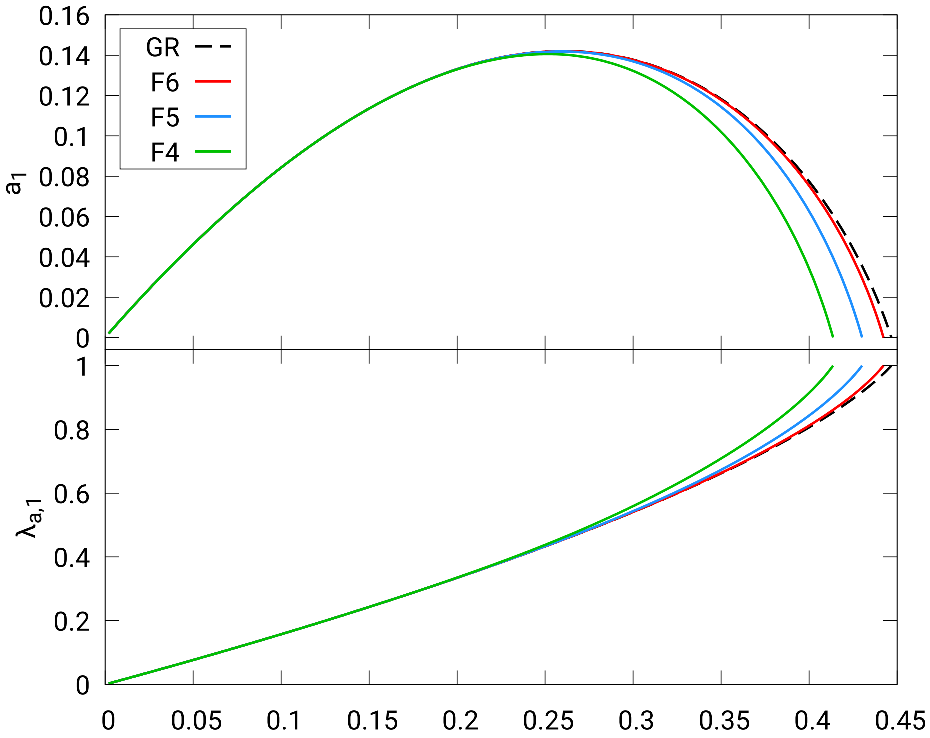

Fig. 6.5: Evolution of the first axis a_1 of an ellipsoid with $\lambda_{a,1} = 1.5$, $\lambda_{a,2} = 1.3$, $\lambda_{a,3} = 1$ (top panel) and of the eigenvalue λ_1 (bottom panel) for different values of f_{R0}: $f_{R0} = -10^{-4}$ shown in green, $f_{R0} = -10^{-5}$ shown in blue, and $f_{R0} = -10^{-6}$ shown in red. The dashed black line represents the standard case.

- The results obtained for different values of the f_{R0} parameter, plotted in Fig. 6.5, confirm that the evolution of the ellipsoid approaches the GR one as $f_{R0} \to 0$.

6.3 Implementation status

The combination of 2LPT and EC described respectively in §5 and §6, formulated in the case of $f(R)$ gravity, provide the theoretical framework for the extension of PINOCCHIO to MG models. In both cases, implementation in a fast approximate method requires to find the optimal balance between accuracy and speed: solving the full equation for 2LPT displacements and computing collapse times with the extension of the BM approach would be too computationally demanding. In this sense, the ideal methods are provided by the approximation for the second-order growth rate proposed in the previous chapter and the extension of the NGS approach to $f(R)$ gravity described here.

Software development is currently ongoing. With respect to version 4.1.2 of PINOCCHIO, we performed the following modifications:

- In the context of standard ΛCDM, we implemented the computation of CT with the NGS prescription. This results in a more accurate evaluation of collapse times with respect to the previous LPT based implementation, as discussed in §6.1 and shown in Fig. 6.3. For each smoothing radius the code evaluates CT solving eq. 2.49 on a grid of values of $\lambda_1, \lambda_2, \lambda_3$, instead of solving for each particle. The results are stored in a matrix, and each time the `collapse_times` routine is called CT are computed interpolating over the matrix;

- The approximate second-order growth rate described in §5 allows to factorize the Fourier-space displacement field in terms of $D_2(k, a)$ times the initial displacement field. However, to construct halos the code requires the computation of displacements in configuration space. In the standard ΛCDM case, the factorization of displacements holds true also in configuration space; in Rizzo et al. (2017), an effective factorization was assumed (4.3), but this could be a poor approximation in the MG case, because of the mode coupling induced by the scalar field. We are currently devising an optimal way to compute configuration-space displacements with the best compromise between accuracy and computational time.

At the moment, we are working on the implementation of the EC extension to MG following the approach presented in 6.2.2. Once the code is ready and well tested, we will go through a comparison of our results with N-body simulations. Then we will release the code, providing the community with a tool to compute covariance matrices for different cosmological observables, useful in the construction of covariance matrices to constrain extensions of the standard ΛCDM scenario in view of future galaxy surveys.

Chapter 7

Conclusions

This PhD thesis addresses the extension of approximate methods to generate simulated dark matter halo catalogs in the framework of modified gravity theories. These are an extension of the standard ΛCDM model of cosmology, alternative to the introduction of a cosmological constant; MG models foresee specific signatures on cosmological observables, that are however not detected in currently available data. Future galaxy surveys, such as Euclid, SKA, DESI or LSST, will provide a large amount of high-precision data, with the potential to provide tight constraint on the cosmological parameters and disentangle between different gravity theories. Shedding light on these topics requires a precise measurement of the cosmological parameters (with percent level accuracy) and to discriminate among different MG models. To achieve these goals it is crucial to accurately model the non-linear regime of structure formation, where characterizing signatures of different MG models can be found. The ability to constrain the cosmological model is strongly dependent on the capability to properly compute covariance matrices and likelihoods for different cosmological observables. Performing such task requires the generation of large sets of simulated dark matter halo (and galaxy) catalogs, which would be unfeasible with computationally expensive N-body simulations. A viable alternative is provided by approximate methods, able to quickly produce predictions of cosmological observables, and to describe the mildly NL scales with minor compromises in accuracy.

One such method is implemented in the PINOCCHIO software (Monaco et al., 2002a,b), whose algorithm is based on Lagrangian PT, ellipsoidal collapse and the extended Press-Schechter formalism. PINOCCHIO is already used within the Euclid collaboration to compute covariance matrixes in the context of the standard model of cosmology: the main goal of this PhD was to extend it to MG theories of gravity.

The first analysis I performed was related to a possible way of including warm dark matter cosmologies in the code (§4). The impact of WDM is a suppression of density fluctuations below some threshold, resulting in a decrease in the number of high mass halos. The washing out of small scale fluctuations due to WDM can be described by means of a truncated power spectrum. However, the use of such truncated power spectrum in PINOCCHIO highlights an inability of the code to properly reproduce the WDM mass function: the loss of halos is present on all mass scales, and not only at the high mass end of the spectrum. In the context of PINOCCHIO, a similar result can be obtained by changing the minimum radius on which the code performs the smoothing (by default set to $R_{\rm min} = 0$). To further investigate the problem, I performed several tests with different smoothing schemes, described in §4.3. An object-by-object analysis, performed by checking the particle membership to halos in two realizations with different $R_{\rm min}$, shows that a significant fraction of halo particles end up in filaments in the $R_{\rm min} > 0$ case. Such outcome reveals an issue in the fragmentation process, likely related to the calibration of the threshold distance for accretion. Such calibration is however cosmology independent, and should hold also in the WDM case. Possibly, the parameterization chosen for the threshold is wrong, though the issue is not evident in the standard CDM case. Since the process of re-calibration is quite cumbersome, it is left for a future work.

Extending PINOCCHIO to MG requires a proper reformulation of both LPT and EC in modified gravity, as well as implementation in the code. Concerning LPT, the main difficulty arise in the treatment of the growth rate, since in MG it is scale dependent. Hence, the factorization of displacements in time- and scale-dependent functions is no longer a viable option. Moreover, to compute the second-order displacement field one must in principle solve a 9-dimensional integral that runs over all possible triangle configurations formed by $\vec{k}_1$, $\vec{k}_2$ and $\vec{k}$ in Fourier space. Such a computation would be quite demanding in terms of computational time, and is therefore not suitable for implementation in PINOCCHIO. In §5 I described a new numerical method aimed at determining the second order Lagrangian displacement field for particles. Such method relies on fast Fourier transforms to compute the full source term of the differential equation for second-order Lagrangian displacements, and allows to test different approximation for the second order growth rate. The MG model I consider is Hu–Sawicki $f(R)$, though the approach is quite general and can easily be applied to other MG theories. Using the approximated growth rate, I computed the 2LPT displacement field for particles, and used it to construct the halo catalogs. The method's predictions were tested against the set of full N-body DUSTGRAIN-pathfinder simulations (Giocoli et al., 2018). I grouped the particles in halos according to the halo-membership provided by the N-body catalog, and compute the halo power spectrum in order to compare it to the one measured from the simulations. The method is able to recover the simulation power spectrum with 10% level accuracy up to scales of $k \sim 0.2 - 0.4$ h Mpc^{-1}. Using this technique, I also tested the Lagrangian approach in the context of MG and compared it to the standard GR case, showing that the performance of LPT with modified gravity is the same as the one obtained in the standard case. The results of this work are presented in a paper (Moretti et al., 2019), already accepted for publication in MNRAS.

In PINOCCHIO, the computation of collapse times is performed by treating overdensities as homogeneous ellipsoids. Therefore, a proper description of EC in the framework of MG is required. Such description should include both the enhancement of gravity due to the fifth force and a screening mechanism. In its standard version, the code implements the computation of collapse times based on the LPT description (§2.3.3), which uses the linear growth rate as a time variable. However, the scale dependence of the growth rate in MG makes this prescription not easily extendable. Two possible alternatives are provided by the Bond & Myers (1996) (BM) and Nadkarni-Ghosh & Singhal (2016) (NGS) approaches, formulated in the context of standard ΛCDM. In 6 I performed a thorough comparison between the three methods, showing that collapse times computed with LPT deviate by less than 2% from those evaluated with BM. The NGS results, on the other hand, differ by less than 0.2% from BM, hence BM and NGS provide very similar outcomes. However, the solution of the BM equations is ∼30 times slower respect to the NGS ones, since the former involves integro-differential equations. The suitable approach to be implemented in PINOCCHIO is then the NGS description. In §6.2.2 I presented an extension of the NGS prescription to Hu-Sawicki $f(R)$ models, starting from the results of Ruan et al. (2020). The force modifications due to MG are introduced by means of an effective gravitational constant, derived from the radial profile of the MG scalar field for a spherical top-hat. I performed some preliminary tests on the NGS extension to MG, confirming that: (i) the NGS extension and the BM extension of Ruan et al. (2020) yield the same results; (ii) in MG collapse proceeds faster respect to the standard GR case; (iii) the evolution of the ellipsoid reduces to standard GR as the value of the f_{R0} parameter decreases . Implementation of the extension of the NGS approach to MG in PINOCCHIO is currently ongoing. These results will be the topic of a forthcoming paper (Moretti 2020, in preparation).

In the future I will extend the code to include more MG theories, to broaden its capacity in the framework of beyond-ΛCDM cosmological models. Moreover, recent works (e.g. Baldi et al. 2014) have highlighted a possible degeneracy between MG and massive neutrinos, which could in principle hinder our capability to distinguish between a Universe described by ΛCDM and one with MG+massive neutrinos. In Rizzo et al. (2017), PINOCCHIO was extended to massive neutrino cosmologies. I will implement the code to account for both effects simultaneously, which would be beneficial both in the computation of covariance matrices and the determination of the proper observables to break the abovementioned degeneracies.

To summarize, in this thesis I described the extension of 2LPT and EC to $f(R)$ gravity, providing the optimal numerical approaches to implement them using a fast, approximate method. These findings constitute the theoretical framework for the extension of PINOCCHIO to MG models. Once the code is ready and well tested, we will go through a comparison of our results with N-body simulations, followed by the release of the code. The extended version of PINOCCHIO will be a valuable tool to compute covariance matrices for cosmological observables in the context of beyond-ΛCDM models, a crucial task for constraining cosmological parameters with future surveys, such as Euclid.

List of Figures

References

Abbott B. P., et al., 2016, Phys. Rev. Lett., 116, 061102

Abbott B. P., et al., 2017a, Phys. Rev. Lett., 119, 161101

Abbott B. P., Abbott R., Abbott T. D., Acernese F., Ackley K., Adams C. e. a., 2017b, ApJ, 848, L12

Abbott T. M. C., et al., 2018, MNRAS, 480, 3879

Abbott T. M. C., et al., 2019, Phys. Rev. D, 99, 123505

Alam S., et al., 2017, MNRAS, 470, 2617

Alcock C., Paczynski B., 1979, Nature, 281, 358

Amendola L., Tsujikawa S., 2010, Dark Energy: Theory and Observations

Amendola L., et al., 2018a, Living Reviews in Relativity, 21, 2

Amendola L., Kunz M., Saltas I. D., Sawicki I., 2018b, Phys. Rev. Lett., 120, 131101

Anderson L., et al., 2012, MNRAS, 427, 3435

Angrick C., Bartelmann M., 2010, A&A, 518, A38

Angulo R. E., Hahn O., Abel T., 2013, MNRAS, 434, 3337

Appleby S., Battye R., 2007, Physics Letters B, 654, 7

Arbey A., 2012, Computer Physics Communications, 183, 1822

Armendariz-Picon C., Mukhanov V., Steinhardt P. J., 2000, Phys. Rev. Lett., 85, 4438

Avila S., Murray S. G., Knebe A., Power C., Robotham A. S. G., Garcia-Bellido J., 2015, MNRAS, 450, 1856

Aviles A., Cervantes-Cota J. L., 2017, Phys. Rev. D, 96, 123526

Axelsson M., Hansen F., Koivisto T., Mota D. F., 2014, A&A, 564, A113

Babichev E., Deffayet C., Ziour R., 2009, International Journal of Modern Physics D, 18, 2147

Baldi M., Villaescusa-Navarro F., Viel M., Puchwein E., Springel V., Moscardini L., 2014, MNRAS, 440, 75

Barnes J., Hut P., 1986, Nature, 324, 446

Bassett B. A., Corasaniti P. S., Kunz M., 2004, ApJ, 617, L1

Baumann D., Nicolis A., Senatore L., Zaldarriaga M., 2012, J. Cosmology Astropart. Phys., 2012, 051

Bernardeau F., Colombi S., Gaztañaga E., Scoccimarro R., 2002, Phys. Rep., 367, 1

Bernardeau F., Crocce M., Scoccimarro R., 2008, Phys. Rev. D, 78, 103521

Bernardeau F., Crocce M., Scoccimarro R., 2012, Phys. Rev. D, 85, 123519

Berti E., et al., 2015, Classical and Quantum Gravity, 32, 243001

Bertschinger E., 1998, ARA&A, 36, 599

Bicknell G. V., 1974, Journal of Physics A Mathematical General, 7, 341

Blake C., et al., 2011, MNRAS, 415, 2892

Blas D., Garny M., Konstandin T., 2014, J. Cosmology Astropart. Phys., 2014, 010

Blot L., et al., 2019, MNRAS, 485, 2806

Bode P., Ostriker J. P., Turok N., 2001, ApJ, 556, 93

Bond J. R., Myers S. T., 1996, ApJ, 103, 1

Bond J. R., Cole S., Efstathiou G., Kaiser N., 1991, ApJ, 379, 440

Bouchet F. R., Colombi S., Hivon E., Juszkiewicz R., 1995, A&A, 296, 575

Bower R. G., 1991, MNRAS, 248, 332

Boylan-Kolchin M., Bullock J. S., Kaplinghat M., 2011, MNRAS, 415, L40

Brax P., Valageas P., 2014a, Phys. Rev. D, 90, 023507

Brax P., Valageas P., 2014b, Phys. Rev. D, 90, 023508

Brax P., van de Bruck C., Davis A.-C., Li B., Shaw D. J., 2011, Phys. Rev. D, 83, 104026

Buchert T., 1992, MNRAS, 254, 729

Buchert T., 1994, MNRAS, 267, 811

Buchert T., Ehlers J., 1993, MNRAS, 264, 375

Bullock J. S., 2010, arXiv e-prints, p. arXiv:1009.4505

Burgess C. P., 2013, arXiv e-prints,

Burrage C., Sakstein J., 2018, Living Reviews in Relativity, 21, 1

Capozziello S., de Laurentis M., Odintsov S. D., Stabile A., 2011, Phys. Rev. D, 83, 064004

Cardone V. F., Capozziello S., 2011, MNRAS, 414, 1301

Carrasco J. J. M., Hertzberg M. P., Senatore L., 2012, Journal of High Energy Physics, 2012, 82

Carrasco J. J. M., Foreman S., Green D., Senatore L., 2014, J. Cosmology Astropart. Phys., 2014, 057

Castorina E., Sefusatti E., Sheth R. K., Villaescusa-Navarro F., Viel M., 2014, Journal of Cosmology and Astro-Particle Physics, 2014, 049

Chevallier M., Polarski D., 2001, International Journal of Modern Physics D, 10, 213

Chuang C.-H., Kitaura F.-S., Prada F., Zhao C., Yepes G., 2015a, MNRAS, 446, 2621

Chuang C.-H., et al., 2015b, MNRAS, 452, 686

Cognola G., Elizalde E., Nojiri S., Odintsov S. D., Sebastiani L., Zerbini S., 2008, Phys. Rev. D, 77, 046009

Colavincenzo M., et al., 2019, MNRAS, 482, 4883

Colless M., et al., 2003, arXiv e-prints, pp astro–ph/0306581

Copeland E. J., Sami M., Tsujikawa S., 2006, International Journal of Modern Physics D, 15, 1753

Creminelli P., Vernizzi F., 2017, Phys. Rev. Lett., 119, 251302

Crocce M., Scoccimarro R., 2006, Phys. Rev. D, 73, 063519

Crocce M., Fosalba P., Castand er F. J., Gaztañaga E., 2010, MNRAS, 403, 1353

Cyburt R. H., Fields B. D., Olive K. A., Yeh T.-H., 2016, Reviews of Modern Physics, 88, 015004

Damour T., Polyakov A. M., 1994, Nuclear Physics B, 423, 532

Daniel S. F., Linder E. V., 2010, Phys. Rev. D, 82, 103523

Daniel S. F., Linder E. V., Smith T. L., Caldwell R. R., Cooray A., Leauthaud A., Lombriser L., 2010, Phys. Rev. D, 81, 123508

Davis M., Peebles P. J. E., 1983, ApJ, 267, 465

De Felice A., Tsujikawa S., 2010, Living Reviews in Relativity, 13, 3

De Laurentis M., De Martino I., 2013, MNRAS, 431, 741

Dodelson S., Widrow L. M., 1994, Phys. Rev. Lett., 72, 17

Dvali G., Gabadadze G., Porrati M., 2000, Physics Letters B, 485, 208

Einstein A., 1916, Annalen der Physik, 354, 769

Eisenstein D. J., Hu W., 1998, ApJ, 496, 605

Eisenstein D. J., et al., 2005, ApJ, 633, 560

Euclid Collaboration et al., 2019, arXiv e-prints, p. arXiv:1910.09273

Event Horizon Telescope Collaboration et al., 2019, ApJ, 875, L1

Feng Y., Chu M.-Y., Seljak U., McDonald P., 2016, MNRAS, 463, 2273

Forero D. V., Tórtola M., Valle J. W. F., 2012, Phys. Rev. D, 86, 073012

Freedman W. L., et al., 2019, ApJ, 882, 34

Friedmann A., 1922, Zeitschrift fur Physik, 10, 377

Gamow G., 1946, Physical Review, 70, 572

Garrison L. H., Eisenstein D. J., Ferrer D., Tinker J. L., Pinto P. A., Weinberg D. H., 2018, ApJS, 236, 43

Garrison L. H., Eisenstein D. J., Pinto P. A., 2019, MNRAS, 485, 3370

Geller M. J., Huchra J. P., 1989, Science, 246, 897

Giocoli C., Baldi M., Moscardini L., 2018, MNRAS, 481, 2813

Gorbunov D., Khmelnitsky A., Rubakov V., 2008, Journal of High Energy Physics, 2008, 055

Goroff M. H., Grinstein B., Rey S. J., Wise M. B., 1986, ApJ, 311, 6

Gunn J. E., 1977, ApJ, 218, 592

Guth A. H., 1981, Phys. Rev. D, 23, 347

Hagstotz S., Gronke M., Mota D. F., Baldi M., 2019, A&A, 629, A46

Hinterbichler K., Khoury J., 2010, Phys. Rev. Lett., 104, 231301

Hockney R. W., Eastwood J. W., 1988, Computer simulation using particles

Hu W., Sawicki I., 2007, Phys. Rev. D, 76, 064004

Hu B., Raveri M., Silvestri A., Frusciante N., 2015, Phys. Rev. D, 91, 063524

Hubble E. P., 1926, ApJ, 64, 321

Hubble E., 1929, Proceedings of the National Academy of Science, 15, 168

Hulse R. A., Taylor J. H., 1975, ApJ, 195, L51

Huterer D., Turner M. S., 2001, Phys. Rev. D, 64, 123527

Ishak M., 2019, Living Reviews in Relativity, 22, 1

Jain B., Bertschinger E., 1994, ApJ, 431, 495

Joudaki S., et al., 2018, MNRAS, 474, 4894

Joyce A., Jain B., Khoury J., Trodden M., 2015, Phys. Rep., 568, 1

Kaiser N., 1987, MNRAS, 227, 1

Khoury J., 2010, arXiv e-prints, p. arXiv:1011.5909

Khoury J., Weltman A., 2004a, Phys. Rev. D, 69, 044026

Khoury J., Weltman A., 2004b, Phys. Rev. Lett., 93, 171104

Khoury J., Wyman M., 2009, Phys. Rev. D, 80, 064023

Kitaura F. S., Yepes G., Prada F., 2014, MNRAS, 439, L21

Koyama K., 2018, International Journal of Modern Physics D, 27, 1848001

Koyama K., Taruya A., Hiramatsu T., 2009, Phys. Rev. D, 79, 123512

LSST Science Collaboration et al., 2009, arXiv e-prints,

Lacey C., Cole S., 1993, MNRAS, 262, 627

Laureijs R., et al., 2011, preprint

Lemaître G., 1927, Annales de la Société Scientifique de Bruxelles, 47, 49

Lemaître G., 1931, MNRAS, 91, 490

Lesgourgues J., Mangano G., Miele G., Pastor S., 2013, Neutrino Cosmology

Levi M., et al., 2013, arXiv e-prints,

Lewis A., Challinor A., 2011, CAMB: Code for Anisotropies in the Microwave Background (ascl:1102.026)

Li B., Zhao H., 2009, Phys. Rev. D, 80, 044027

Li B., Zhao G.-B., Koyama K., 2013, J. Cosmology Astropart. Phys., 2013, 023

Linde A. D., 1982, Physics Letters B, 108, 389

Linder E. V., 2003, Phys. Rev. Lett., 90, 091301

Linder E. V., 2005, Phys. Rev. D, 72, 043529

Linder E. V., Cahn R. N., 2007, Astroparticle Physics, 28, 481

Lippich M., et al., 2019, MNRAS, 482, 1786

Llinares C., Mota D. F., 2013, Phys. Rev. Lett., 110, 161101

Lombriser L., Li B., Koyama K., Zhao G.-B., 2013, Phys. Rev. D, 87, 123511

Lovelock D., 1969, Archive for Rational Mechanics and Analysis, 33, 54

Lovelock D., 1971, Journal of Mathematical Physics, 12, 498

Maeda K.-I., 1989, Phys. Rev. D, 39, 3159

Maor I., Brustein R., Steinhardt P. J., 2001, Phys. Rev. Lett., 86, 6

Martin J., 2012, Comptes Rendus Physique, 13, 566

Martin J., Ringeval C., Vennin V., 2014, Physics of the Dark Universe, 5, 75

Mather J. C., et al., 1994, ApJ, 420, 439

Mazumdar A., Rocher J., 2011, Phys. Rep., 497, 85

Monaco P., 1995, ApJ, 447, 23

Monaco P., 1997a, MNRAS, 287, 753

Monaco P., 1997b, MNRAS, 290, 439

Monaco P., 2016, Galaxies, 4, 53

Monaco P., Theuns T., Taffoni G., 2002a, MNRAS, 331, 587

Monaco P., Theuns T., Taffoni G., Governato F., Quinn T., Stadel J., 2002b, ApJ, 564, 8

Monaco P., Sefusatti E., Borgani S., Crocce M., Fosalba P., Sheth R. K., Theuns T., 2013, MNRAS, 433, 2389

Moretti C. e. a., 2020, in prep.

Moretti C., Mozzon S., Monaco P., Munari E., Baldi M., 2019, arXiv e-prints, p. arXiv:1909.06282

Moroi T., Murayama H., Yamaguchi M., 1993, Physics Letters B, 303, 289

Munari E., Monaco P., Koda J., Kitaura F.-S., Sefusatti E., Borgani S., 2017a, J. Cosmology Astropart. Phys., 7, 050

Munari E., Monaco P., Sefusatti E., Castorina E., Mohammad F. G., Anselmi S., Borgani S., 2017b, MNRAS, 465, 4658

Nadkarni-Ghosh S., Singhal A., 2016, MNRAS, 457, 2773

Napolitano N. R., Capozziello S., Romanowsky A. J., Capaccioli M., Tortora C., 2012, ApJ, 748, 87

Nunes N. J., Mota D. F., 2006, MNRAS, 368, 751

Okumura T., et al., 2016, PASJ, 68, 38

Olive K. A., Pospelov M., 2008, Phys. Rev. D, 77, 043524

Oort J. H., 1932, Bull. Astron. Inst. Netherlands, 6, 249

Osato K., Nishimichi T., Bernardeau F., Taruya A., 2019, Phys. Rev. D, 99, 063530

Oyaizu H., 2008, Phys. Rev. D, 78, 123523

Padmanabhan T., 2003, Phys. Rep., 380, 235

Peacock J. A., Dodds S. J., 1994, MNRAS, 267, 1020

Peacock J. A., Heavens A. F., 1990, MNRAS, 243, 133

Peebles P. J. E., 1968, ApJ, 153, 1

Peebles P. J., Ratra B., 2003, Reviews of Modern Physics, 75, 559

Peirone S., Raveri M., Viel M., Borgani S., Ansoldi S., 2017, Phys. Rev. D, 95, 023521

Penzias A. A., Wilson R. W., 1965, ApJ, 142, 419

Percival W. J., White M., 2009, MNRAS, 393, 297

Perlmutter S., et al., 1999, ApJ, 517, 565

Pizzuti L., et al., 2017, J. Cosmology Astropart. Phys., 2017, 023

Planck Collaboration et al., 2014, A&A, 571, A12

Planck Collaboration et al., 2016, A&A, 594, A13

Planck Collaboration et al., 2018, arXiv e-prints, p. arXiv:1807.06209

Pogosian L., Silvestri A., Koyama K., Zhao G.-B., 2010, Phys. Rev. D, 81, 104023

Press W. H., Schechter P., 1974, ApJ, 187, 425

Primack J. R., 2009, New Journal of Physics, 11, 105029

Puchwein E., Baldi M., Springel V., 2013, MNRAS, 436, 348

Ratra B., Peebles P. J. E., 1988, Phys. Rev. D, 37, 3406

Reid M. J., Braatz J. A., Condon J. J., Greenhill L. J., Henkel C., Lo K. Y., 2009, ApJ, 695, 287

Riess A. G., et al., 1998, AJ, 116, 1009

Riess A. G., Casertano S., Yuan W., Macri L. M., Scolnic D., 2019, ApJ, 876, 85

Rizzo L. A., Villaescusa-Navarro F., Monaco P., Munari E., Borgani S., Castorina E., Sefusatti E., 2017, J. Cosmology Astropart. Phys., 1, 008

Robertson H. P., 1935, ApJ, 82, 284

Ruan C.-Z., Zhang T.-J., Hu B., 2020, MNRAS, p. 41

Sahni V., Coles P., 1995, Phys. Rep., 262, 1

Schmidt F., 2009, Phys. Rev. D, 80, 123003

Schneider A., et al., 2016, J. Cosmology Astropart. Phys., 2016, 047

Scoccimarro R., 2004, Phys. Rev. D, 70, 083007

Scoccimarro R., Sheth R. K., 2002, MNRAS, 329, 629

Sefusatti E., Crocce M., Scoccimarro R., Couchman H. M. P., 2016, MNRAS, 460, 3624

Shandarin S. F., Zeldovich Y. B., 1989, Reviews of Modern Physics, 61, 185

Shaposhnikov M., Tkachev I., 2006, Physics Letters B, 639, 414

Sheth R. K., Tormen G., 1999, MNRAS, 308, 119

Sheth R. K., Tormen G., 2002, MNRAS, 329, 61

Sivanandam N., 2013, Phys. Rev. D, 87, 083514

Song Y.-S., Hollenstein L., Caldera-Cabral G., Koyama K., 2010, J. Cosmology Astropart. Phys., 2010, 018

Sotiriou T. P., Faraoni V., 2010, Reviews of Modern Physics, 82, 451

Spergel D., et al., 2013, arXiv e-prints,

Springel V., 2005, MNRAS, 364, 1105

Stadel J. G., 2001, PhD thesis, UNIVERSITY OF WASHINGTON

Starobinskiǐ A. A., 1979, Soviet Journal of Experimental and Theoretical Physics Letters, 30, 682

Starobinsky A. A., 1980, Physics Letters B, 91, 99

Taruya A., Nishimichi T., Saito S., 2010, Phys. Rev. D, 82, 063522

Tassev S., Zaldarriaga M., Eisenstein D. J., 2013, J. Cosmology Astropart. Phys., 6, 036

Teyssier R., 2002, A&A, 385, 337

Vainshtein A. I., 1972, Physics Letters B, 39, 393

Valogiannis G., Bean R., 2017, Phys. Rev. D, 95, 103515

Velten H. E. S., vom Marttens R. F., Zimdahl W., 2014, European Physical Journal C, 74, 3160

Verde L., Treu T., Riess A. G., 2019, Nature Astronomy, 3, 891

Walker A. G., 1937, Proceedings of the London Mathematical Society, 42, 90

Watson W. A., Iliev I. T., D'Aloisio A., Knebe A., Shapiro P. R., Yepes G., 2013, MNRAS, 433, 1230

Weinberg S., 1989, Reviews of Modern Physics, 61, 1

Weisberg J. M., Nice D. J., Taylor J. H., 2010, ApJ, 722, 1030

Weller J., Albrecht A., 2001, Phys. Rev. Lett., 86, 1939

Wetterich C., 1988, Nuclear Physics B, 302, 668

White S. D. M., 1984, ApJ, 286, 38

White S. D. M., Silk J., 1979, ApJ, 231, 1

Will C. M., 2014, Living Reviews in Relativity, 17, 4

Winther H. A., Koyama K., Manera M., Wright B. S., Zhao G.-B., 2017, J. Cosmology Astropart. Phys., 8, 006

Wong K. C., et al., 2019, arXiv e-prints, p. arXiv:1907.04869

Wright B. S., Koyama K., Winther H. A., Zhao G.-B., 2019, arXiv e-prints,

York D. G., et al., 2000, AJ, 120, 1579

Zel'dovich Y. B., 1970, A&A, 5, 84

Zhao G.-B., Giannantonio T., Pogosian L., Silvestri A., Bacon D. J., Koyama K., Nichol R. C., Song Y.-S., 2010, Phys. Rev. D, 81, 103510

Zwicky F., 1933, Helvetica Physica Acta, 6, 110

de la Torre S., et al., 2013, A&A, 557, A54